Spring 2014

Covalently Functionalized Noble Metal Nanoparticles for Molecular Imprinted Polymer Biosensors: Synthesis, Characterization, and SERS Detection

Anna Allyse Volkert
University of Iowa

COVALENTLY FUNCTIONALIZED NOBLE METAL NANOPARTICLES FOR MOLECULAR IMPRINTED POLYMER BIOSENSORS: SYNTHESIS, CHARACTERIZATION, AND SERS DETECTION

by

Anna Allyse Volkert

A thesis submitted in partial fulfillment
of the requirements for the Doctor of
Philosophy degree in Chemistry
in the Graduate College of
The University of Iowa

May 2014

Thesis Supervisor: Associate Professor Amanda J. Haes

Graduate College
The University of Iowa
Iowa City, Iowa

CERTIFICATE OF APPROVAL

_____

PH.D. THESIS

_____

This is to certify that the Ph.D. thesis of

Anna Allyse Volkert

has been approved by the Examining Committee
for the thesis requirement for the Doctor of Philosophy
degree in Chemistry at the May 2014 graduation.

Thesis Committee: _____
Amanda J. Haes, Thesis Supervisor

_____
Ned Bowden

_____
C. Allan Guymon

_____
Sarah Larsen

_____
Edward Gillan

To my friends and family who have supported and helped me achieve my goals.

ACKNOWLEDGMENTS

First and foremost I would like to thank my advisor, Professor Amanda Haes, for repeatedly going above and beyond throughout my graduate career. You continually motivate me to strive to become a better chemist, mentor, and educator. I have learned so much and would not be where I am today without your support.

Next, I would like to thank my family for believing in me and supporting me in many different ways to help me achieve my goals. Even when I didn't believe in myself, you have always believed in me and what I could achieve.

I would also like to thank the amazing friends that I have made here at Iowa. You have been my family away from home and I will always treasure the memories we made here. Many of these friendships were formed through Alpha Chi Sigma. The brotherhood of Alpha Chi Sigma was always there for support and guidance in my early years as well as an outlet for me in stressful times. I truly believe I have made true and lasting friendships and will continue to strive for the advancements of chemistry in the future.

Finally, I would like to thank the members of the Haes group, both past and present. I would like to specifically thank Dr. Michael Ivanov and Dr. Varuni Subramaniam for your help, support, and guidance during your tenure in the group. I would also like to thank all of the exceptional undergraduates that I have had the opportunity to mentor. You all have helped me realize my true passion of teaching and without you some of the work presented in this dissertation wouldn't be possible.

ABSTRACT

This dissertation evaluates how gold nanoparticle structure and local environment influence resulting sensor function when using these nanomaterials for complex sample analysis. Molecular imprinted polymers (MIPs), a class of plastic antibodies, are engineered and incorporated into these nanosensors thereby facilitating the quantitative detection of a variety of small molecules when Raman spectroscopy and surface enhanced Raman scattering (SERS) are used for detection. First, homogeneous seeded growth gold nanosphere synthesis is evaluated as a function of ionic double layer composition and thickness. Systematically increasing the citrate concentration during synthesis improves nanomaterial shape homogeneity; however, further elevations of citrate concentration increase the number of internal and/or external atomic defects in the nanomaterials which leads to decreasing solution-phase stability. Next, spherical gold nanoparticles are modified with self-assembled monolayer (SAM), modeled using interfacial energy calculations, and experimental characterized using transmission electron microscopy, NMR, extinction spectroscopy, zeta potential, X-ray photoelectron spectroscopy, and flocculation studies to assess the morphology, surface chemistry, optical properties, surface charge, SAM packing density, and nanoparticle stability, respectively. The number of molecules on the nanostructures increases with increasing ionic strength (by decreasing the electrostatic interfacial energy between assembled molecules) which subsequently promotes nanoparticle stability. Third, plastic antibodies that recognize three drugs commonly used to treat migraines are engineered. These methacrylate-based MIPs are synthesized, extracted, characterized, and used to quantitatively and directly detect over-the-counter drugs in complex samples using Raman microscopy. These results along with numerical approximation methods to estimate drug binding site densities and dissociation constants with the MIPs serve as a foundation for understanding how modest recognition selectivity of MIPs coupled with

shifts in the vibrational energy modes from the drugs upon hydrogen binding to the polymer backbone promote sensitive and selective drug detection in complex samples. Finally, nanomaterial incorporation into MIPs for applications in SERS-based biosensors is evaluated. Importantly, gold nanorod concentration increases the detectability of the same drugs using MIPs as pre-concentration and recognition elements. This combination of materials, theory, and applications forms a solid foundation which should aid in the design and development of MIP nanobiosensors for specific and sensitive detection of small molecules in complex matrices.

TABLE OF CONTENTS

LIST OF TABLES

LIST OF FIGURES

CHAPTER 1 ADVANCEMENTS IN NANOSENSORS USING PLASTIC ANTIBODIES

1.1 Introduction

Biosensors contain immobilized receptors to detect biomolecules and are typically classified as affinity or affinity/catalytic devices.[1-3] In the former, a ligand binds to a receptor which causes either a change in receptor charge, conformation, optical parameter, and/or in the temperature of the medium.[1-3] In affinity/catalytic devices, initial ligand binding is followed by the production of a new reactive species that is then detected.[1-3] This chapter will focus on recent developments in affinity biosensors. Affinity biosensors typically rely on specific interactions between natural recognition elements such as antibodies, aptamers, and/or DNA with a ligand[2,4] Signal transduction methods applied to biosensors include amperometry, potentiometry, and optical spectroscopy.[3] Regardless of the method of signal transduction, biosensors are assessed based on figures of merit such as assay time, dissociation constant (K_d), limits of detection, and throughput.[2,3]

Immunoassays are a class of affinity biosensors which use immobilized recognition elements for either competitive or non-competitive detection of target analytes.[5] Competitive immunoassays typically employ an analyte and labeled analyte which competitively bind to an immobilized antibody.[1,2,5] In competitive immunoassays, analyte detectability is limited by the affinity constant to the employed antibody.[5] To improve detection limits, a non-competitive or two-site immunoassay (sandwich type) is employed where the analyte and a secondary labeled antibody are added sequentially to an immobilized capture antibody.[2,5] Sandwich-type immunoassays allow for the quantification of proteins and chemical/biowarfare agents with sub-μM range detection

[1] Adapted from *Advancements in Nanosensors using Plastic Antibodies*, Anna. A. Volkert and Amanda J. Haes, Analyst, **2014**, 139, 21-31.[1]

limits.[2] Typical assays times range anywhere from 2 to 60 minutes and additional pretreatment and washing steps which can take hours to days.[2]

To further improve the signal to noise of optical affinity biosensor responses, noble metal nanomaterials are often incorporated allowing for numerous "enhanced" detection methods such as colorimetry,[6-10] surface enhanced Raman spectroscopy (SERS),[11-16] and surface plasmon-based methods.[17-25] Biosensors which incorporate noble metal nanomaterials were extensively reviewed elsewhere and specifically focused on localized and surface plasmon biosensors as well as SERS biosensors.[17,18,26]

Biosensors that employ naturally occurring recognition elements require "biocompatible" solution conditions to prevent antibody degradation. In contrast, plastic antibodies provide a more environmentally stable and cheaper alternative than these naturally occurring recognition elements[27] Molecular imprinted polymers (MIP), a class of plastic antibodies, promote biomolecule recognition and detection with affinities and selectivities that rival that of traditional antibody-antigen couples thereby allowing for specific detection of target analytes.[28-32] Previously, molecular imprinting generated stable, specific recognition elements to detect drug molecules,[33-37] proteins,[38-46] and toxins[47-52] for use in biological and chemical sensors,[28,34-37,41,51-55] drug delivery,[46,48,56,57] and separations.[27,33,47,58,59] Other review articles summarized molecular imprinted polymer applications,[27,54,60] biosensors,[28,44] drug delivery,[56] and synthesis.[55,61]

Herein, the first section of this review examines biosensors that include noble metal nanoparticles along with naturally occurring recognition elements for optical sensors. Specifically, nanomaterials and enhanced signal transduction in aggregation-based immunoassays, plasmonic biosensors, SERS, and surface plasmon resonance (SPR) biosensors will be discussed. In the second section of the review, discussion of artificial recognition elements will focus on plastic antibody synthesis, limitations, and recent advances in plastic antibody technology. In the third and final section of this review, the advantages and methods of incorporating plastic antibodies into nanosensors

for real world applications will be explored. Specifically, noble metal nanomaterial incorporation into electrochemical, fluorescence, and SERS MIP sensors will be described. To our knowledge, this is the first review which focuses on noble metal nanomaterial incorporation into molecular imprinted polymers for real-world sensor applications for biological and environmental sample analysis. Future improvements in design of artificial recognition agents are envisioned to facilitate new methods for complex biological and chemical analyses.

1.2 Naturally Occurring Recognition Elements for Optical Sensors

Biosensors contain biological elements that recognize target analytes and signal transduction elements for detection.[4,22] The biological recognition element typically consists of naturally occurring recognition species such as antibodies, aptamers, and/or DNA.[4] These molecules possess high selectivity and affinity for target biomolecules which lead to specific detection of biomarkers,[16,19] proteins,[6-13,15,20-23,25,62] and viruses.[14,24] Improvement to optical biosensors can be made by incorporating noble metal nanomaterials for improved signal transduction allowing for numerous "enhanced" detection methods.[2]

Biosensors which utilize noble metal (Ag, Au, Cu) nanoparticles exhibit novel size dependent properties and enhanced biological and chemical detectability. For instance, the extinction (absorption + scattering) spectrum of gold nanoparticles can be tuned throughout visible to near-infrared wavelengths by varying the local dielectric environment (*i.e.* the surrounding medium and/or surface modification), metal, shape, or size.[63-65] Extinction spectra arise when the frequency of the electromagnetic field is in resonance with the oscillation of conduction band electrons. This phenomenon is known as the localized surface plasmon resonance (LSPR) and can be exploited for biosensor signal transduction.[66] A typical extinction maximum wavelength for 13 nm diameter

solution-phase spherical gold nanoparticles in water is 520 nm. When these particles agglomerate and/or aggregate, a new lower energy resonance forms at ~650 nm.[67] Relevant to biosensor developments, the exploitation of the controlled aggregation of antibody or aptamer functionalized nanomaterials allows for quantitative protein detection in complex matrices.[6-10,62]

Herein, noble metal nanomaterials and their method of signal transduction in aggregation-based immunoassays, plasmonic biosensors, and SERS biosensors will be described. Specifically, the signal transduction method, assay times, detection limits, and advantages of each biosensor will be thoroughly discussed and are briefly summarized in Table 1.1

Table 1.1. Comparison of Nanoparticle Based Biosensors.

	Nanoparticle Signal Transduction Method	Assay Time	Detection Limits	Advantages
Aggregation-Based Immuno-assays[6-10,62]	Extinction magnitude between 600 – 650 nm	1 - 6 hours	0.2 - 20 nM	Simple instrumenta-tion
Plasmonic Biosensors [19,20,22-25]	Refractive index changes	30 min – 3 hours	1 aM - 10 pM	High sensitivity
SERS Biosensors [11-14,16]	Enhanced Raman scattering	20 min – 24 hours	0.2 – 200 pM	Multiplexed and rapid detection in complex matrices

1.2.1 Aggregation-based Immunoassays

The simplest aggregation-based immunoassays with noble metal nanomaterials involve adding a target antigen to an aptamer or antibody functionalized nanoparticle solution and monitoring nanoparticle aggregation using extinction spectroscopy.[6,9,10]

Thanh and Rosenzweig used an aggregation-based immunoassay to quantify anti-protein A in solution by aggregating protein A functionalized gold nanoparticles with 0 – 50 μg/mL of anti-protein A. As expected, the optical density at 620 nm increased systematically with increasing anti-protein A concentration yielding a detection limit of 1 μg/mL. The detection limits are comparable to that observed using ELISA but required a total assay time of only 2 hours.[9]

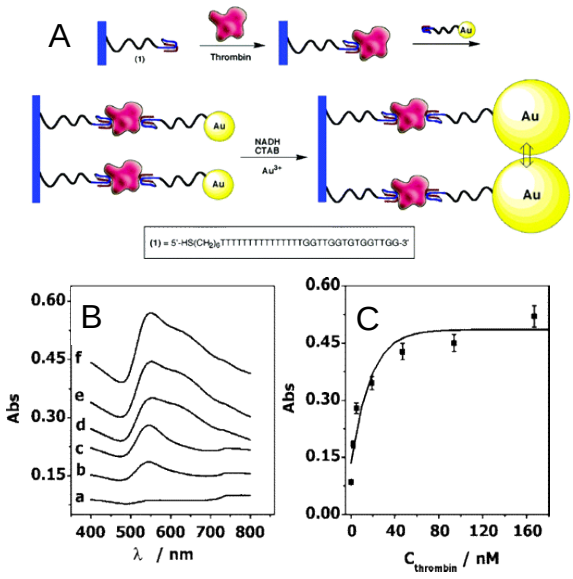

Figure 1.1. Aggregation-based immunoassay for thrombin detection. (A) Amplified detection of thrombin on surfaces by the catalytic enlargement of thrombin aptamer-functionalized gold nanoparticles. (B) Absorbance spectra of thiolated aptamer modified glass slides incubated in (a) 0, (b) 2, (c) 5, (d) 19, (e) 94, and (f) 167 nM thrombin using thiolated aptamer functionalized gold nanoparticles and the catalytic enlargment process. Slides were removed from the enhancement solution and rinsed prior to the recording of the spectra. (C) Calibration curve corresponding to the amplified optical detection of thrombin (reprinted with permission from reference 8, Copyright 2004 American Chemical Society).

In another example, Aslan and coworkers determined that the aggregation of functionalized nanoparticles in the presence of a receptor depended on the affinity of the ligand/receptor binding as well as the number of collisions between ligand functionalized

nanoparticles and receptors.[7] Aggregation of biotinylated gold nanoparticles using 4 – 200 nM streptavidin was quantified by plotting extinction magnitude changes at 600 nm. The well-studied biotin streptavidin system exhibits a strong binding constant (~10^{13} M^{-1})[18,22] which allowed for the assumption that aggregation is dominated by the collision frequency of streptavidin and biotin functionalized gold nanoparticles (no longer depended on ligand/receptor binding constraints). The collision frequency was then correlated to the extent of aggregation and used to model nanoparticle aggregation kinetics for biotin functionalized gold nanoparticles. These findings led to a better understanding of nanoparticle aggregation and as a result, more reproducible responses in this class of immunoassays.

In the previous examples, the magnitude of aggregation depended on analyte concentration. To overcome this inherent limitation, catalytic amplification promoted nanoparticle aggregation assays are used to amplify signals.[8,62] For instance, thrombin aptamer functionalized gold nanoparticles were aggregated in the presence of thrombin, separated from the nanoparticle solution, and used as seeds for catalytic growth in the presence of CTAB, $HAuCl_4$, and a reducing agent (NADH). The thrombin detection limit was ~20 nM, a 5-fold improvement when compared to traditional colorimetric thrombin detection methods. The detection of thrombin was further amplified using catalytic enlargement on glass surfaces where a thrombin aptamer was immobilized on a glass substrate and incubated in various concentrations of thrombin. The second binding site of thrombin was then available for binding with aptamer functionalized gold nanoparticles which were then enlarged using a growth solution (Figure 1.1A).[8] Absorbance spectra were collected after incubating the biosensor in thrombin concentrations varying from 0 to 160 nM (Figure 1.1B).[8] Specifically, the number of surface bound gold nanoparticles caused a systematic increase in absorbance at 650 nm as the thrombin concentration increased. A calibration curve was generated using the plasmon magnitude at 650 nm as a function of thrombin concentration (Figure 1.1C).[8] The detection limit improved by an

order of magnitude for catalytically enhanced assays *vs.* solution-phase measurements. All in all, controlled amplification of nanoparticle aggregation after a specific recognition event yielded reproducibly amplified signals and therefore, more sensitive aggregation-based immunoassay responses.

1.2.2 Plasmonic Biosensors.

While aggregation-based immunoassays use simple instrumentation and nanomaterial design strategies, biosensor sensitivity is limited by the number of aggregation events and require long incubation times to ensure maximized signals (*i.e.* equilibrium responses). As a result, sensing platforms using surface plasmon resonance (SPR) and LSPR spectroscopy are used as these signal transduction methods rely on measuring small changes in refractive index that result from analyte binding to the recognition element at or near the surface of a noble metal thin film or nanoparticle.[17,18,22] Molecular binding kinetics near the metal surface can be measured in real-time on the 10^{-1}-10^{3} s time scale with refractive index sensitivities on the order of 1 part in $10^{5} – 10^{6}$.[17,22] For instance, a SPR sensor successfully quantified avian influenza virus by first immobilizing an avian influenza aptamer to a gold surface and measuring the refractive index through changes in the angle of incidence in 0 – 12.8 hemagglutinating unit (HAU) avian influenza.[24] The avian influenza virus SPR sensor was portable and shown to detect avian influenza in 1.5 hours which is ~100x faster than current state of the art virus isolation and identification methods (*i.e*. ELISA).

Similar to SPR sensors, LSPR sensors take advantage of small refractive index changes induced by recognition events near a nanoparticle surface by measuring extinction magnitude or wavelength shifts.[18,22] Previously, a typical LSPR biosensor was constructed by (1) functionalizing surface immobilized triangular Ag nanoparticles with a self-assembled monolayer (SAM), (2) covalently attaching antibodies or aptamers to the SAM carboxylate groups, and (3) incubating the biosensor in a target biomolecule

solution while monitoring shifts in the extinction maximum wavelength ($\Delta\lambda_{max}$).[19,20,22] The biotin/streptavidin binding couple was used to determine the mechanism of LSPR biosensor responses.[20,22] Incubating a biotin functionalized nanosensor in 100 nM streptavidin resulted in a 27 nm red shift in the extinction maximum wavelength.[22] Varying the streptavidin concentration from 10^{-15} – 10^{-6} M resulted in a systematic λ_{max} shift yielding a surface-confined binding constant ($K_{a,surf}$) of 10^{11} M^{-1} and a streptavidin detection limit less than 1 pM.[22] This work demonstrates the selectivity and specificity capabilities of LSPR biosensors.

Since this work, development of LSPR biosensor applications continued.[19,20,22] The LSPR nanobiosensor response can be magnified by incorporating traditional "sandwich" bioassays using functionalized gold nanoparticles.[19,20,22] For example, nanoparticle substrates were fabricated by functionalizing surface immobilized Ag nanoparticles with an octanethiol/11-mercaptundecanoic acid SAM layer and amine-conjugated biotin. After incubation in a biotin solution, anti-biotin functionalized gold (Au@Ab) nanoparticles were introduced to the biosensor. Extinction spectra were measured after the LSPR sensor was incubated with 100 nM unlabeled antibiotin ($\Delta\lambda_{max}$ = 11 nm). Alternatively, after incubation with the Au@Ab nanoparticles, a 42.7 nm redshift occurred, a ~400% increase compared to the unlabeled antibiotin.[20]

Increased LSPR nanobiosensor sensitivity without the use of a sandwich assay can be achieved by altering the nanostructure employed in the biosensor.[25] As an example, Balamurugan and coworkers observed that increased thrombin sensitivity was achieved with gold nanorod substrates *vs.* gold bipyramid substrates as a result of higher surface coverage of thrombin aptamer on the gold nanorod substrates.[25] After the substrate-bound nanoparticles were functionalized with thrombin aptamer, thrombin solutions (concentration = 0 – 10^{-6} M) were incubated with the samples. Systematic λ_{max} shifts for the gold nanorod substrates and gold bipyramid substrates are shown in Figure 1.2A and 1.2B, respectively.[25] Interestingly, the gold bipyramid substrate which exhibited

a refractive index sensitivity twice that of gold nanorods revealed a ~25% smaller response *vs.* the gold nanorod substrate.2 X-ray photoelectron spectroscopy indicated that the reduced detection signals for the gold bipyramid could be attributed to ~1/2 the number of aptamer capture strands (*i.e.* surface density) on the bipyramids *vs*. the gold nanorods.[25] This study demonstrates that careful control of aptamer surface coverage on as well as refractive index sensitivity of the plasmonic substrate is vital to biosensors design.

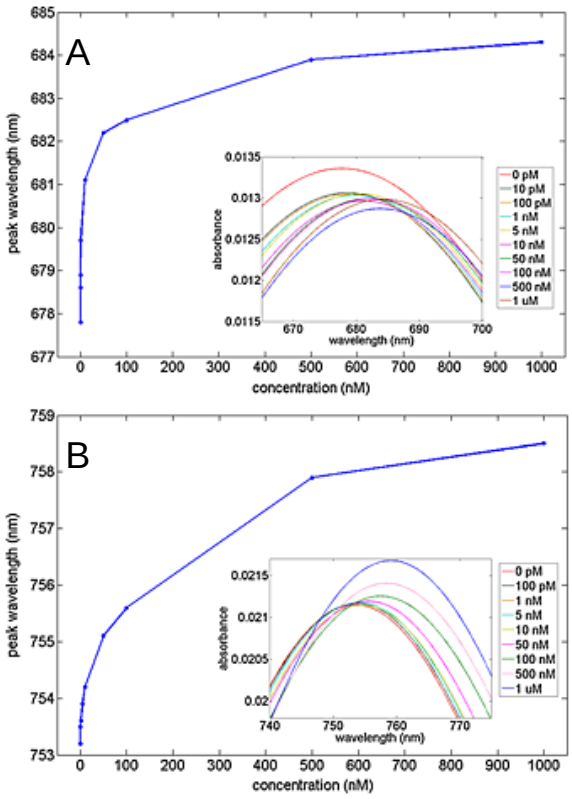

Figure 1.2. Wavelength shift responses for 0 pM – 1 μM thrombin for (a) gold nanorod substrates and (b) gold bipyramid substrates. The inset shows the UV–vis spectra obtained for increasing thrombin concentrations (reprinted with permission from reference 25, Copyright 2013, Wiley).

1.2.3 Surface-Enhanced Raman Scattering Biosensors

While LSPR sensors exhibit high sensitivities (~350 nm/RIU) and selectivities when receptors are used, multi-analyte detection is limited by non-specific refractive index changes resulting in universal signal transduction. One opportunity to overcome this limitation of refractive index sensors is to use SERS biosensors. SERS sensors combine natural recognition elements such as antibodies and antigens with large signal enhancements from gold and/or silver nanomaterials as well as with narrow and unique Raman vibrational bands for multiplexed detection.[11-14,16] SERS biosensors are characterized as either label (indirect) or label-free (direct). Incorporating extrinsic Raman labels into sandwich-style immunoadsorbant assays for indirect measurements decreased assay time without sacrificing sensitive responses to biomarkers,[16] proteins,[13] and viruses.[14]

For instance, extrinsic Raman labels (ERLs) can be synthesized by functionalizing gold nanoparticles with a Raman reporter molecule and antibody. When the target antigen is present, the ERLs bind to the target antigen, and the SERS signal of the reporter molecule is measured.[13,14,16] For example, simultaneous multi-analyte identification capabilities are demonstrated in Figure1.3 and was achieved using three ERLs that were functionalized with 3-methoxybenzenethiol, 2-methoxybenzenethiol, or 4-nitrobenzenethiol and rabbit IgG, human IgG, and mouse IgG, respectively.[13] The SERS spectra for a mixture of all three antibodies, combinations of two analytes, individual analytes, and a blank positively identified target antibodies and illustrated successful multi-analyte detection.[13] Furthermore, quantitative detection of multiple antibodies was simultaneously achieved using ERLs.[13] Possible applications of ERLs include clinical and industrial applications where rapid, multi-analyte quantification is often required.

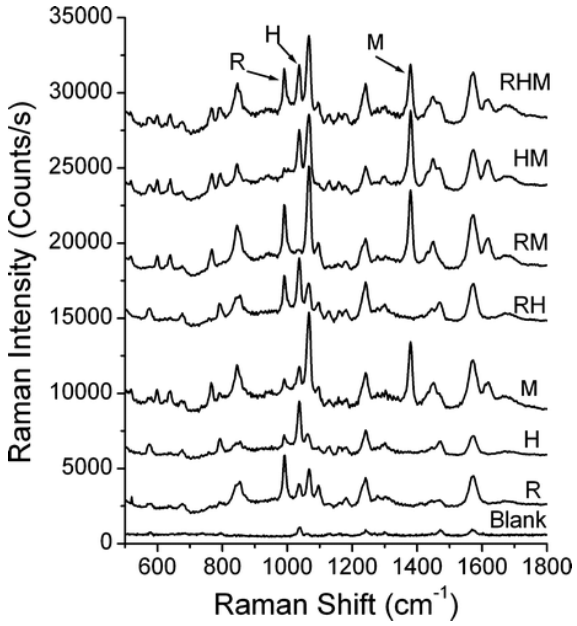

Figure 1.3. Simultaneous detection of three analytes: rabbit IgG (labeled as R), human IgG (labeled as H), as mouse IgG (labeled at M). The reporter molecules are 3-methoxybenzenethiol, 2-methoxybenzenethiol, 4-nitrobenzenethiol, respectively (reprinted (adapted) with permission from reference 13, Copyright 2009 American Chemical Society).

Small molecules can also be detected directly (*i.e.* without the use of ERLs). Advantages of direct detection include reduced assay times and improved selectivity in complex matrices *vs*. indirect detection methods. Previously, label-free SERS biosensors for the detection of protein in a complex sample matrix (*i.e.* milk) was achieved using silver dendrites.[11,12] First, ovalbumin was extracted from milk using an immunomagnetic separation. After extraction and drying, molecule identification was achieved using principle component analysis to exploit differences between the background and analyte. Higher sensitivity was observed for the dried sample *vs*. solution-phase measurements in 0 – 5 μg/mL ovalbumin concentrations. As the ovalbumin concentration increased further, SERS intensities saturated and provided no quantitative information regarding ovalbumin concentration. All in all, the combination of immunomagnetic separation and SERS detection resulted in detection limits <1 μg/ml ovalbumin in less than 20 minutes

(total assay time) in complex matrices making the technology extremely useful in the milk processing industry where rapid and accurate detection of contaminate proteins is required.

1.3 Artificial Recognition Elements

Previously, plastic antibodies provided alternative and more environmentally stable recognition elements than traditional antibodies.[27] Here, a general overview of plastic antibody synthesis, limitations, and recent advances in plastic antibody technology is presented.

MIPs are formed by polymerizing functional and cross linking monomers around a template molecule.[60,68] Initially, functional monomers bind with template molecules forming template-monomer complexes. Upon polymerization, the template-monomer complexes are held in place by the highly crossed-linked polymer.[28,60] Ideally, when template molecules are removed, molecular-specific cavities remain in the MIP that are shape and size-specific for the templated molecule.[28,60,69] A schematic representation of MIP formation is shown in Figure 1.4.[60]

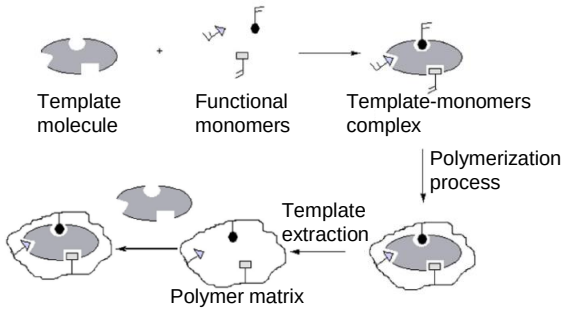

Figure 1.4. Scheme of molecular imprinting (reproduced with permission from reference 60).

Molecular imprinted polymer based biosensors are becoming increasingly popular because of increased stability, ease of use, and low cost *vs*. natural recognition elements.[28,55] Previously, a MIP-based flow-through fluorosensor for digoxin detection in serum samples was compared to a traditional immunosensor.[37] Briefly, a digoxin templated MIP was polymerized, ground, extracted, and integrated into a flow-through injection system where the fluorescence intensity of FITC-digoxin was monitored to determine digoxin binding. For comparison, a traditional immunosensor was constructed by functionalizing glass beads with anti-digoxin. Normalized fluorescence signals for both the MIP fluorosensor and immunosensor were monitored as a function of digoxin concentration. The MIP fluorosensor outperformed the traditional immunosensor with decreased detection limits (1.7×10^{-5} *vs*. 1.2×10^{-3} mg/L), improved precision (n=6) (2 *vs*. 7 % RSD), as well as an increased shelf life (18 *vs*. 3 months).37 The MIP fluorosensor illustrates some advantages of using molecular imprinted polymers in place of naturally occurring antibodies.

Two major challenges associated with MIP-based sensors are the incomplete removal of template during extraction and non-specific binding.[27,28,55] Incomplete extraction can lead to template bleeding in subsequent assays resulting in an over-estimation of target biomolecule concentrations.[36,42] Template bleeding can be reduced by using a structurally similar or "dummy" template molecule with minimal loss of signal from target molecules. In addition to template bleeding, MIPs are often plagued by non-specific binding responses.[42] Tov *et. al.* proposed incorporating a second polymerization step into the MIP synthesis to reduce the number of non-specific binding sites. The secondary polymerization step used monomers designed to react with only the polymer chains which do not actively bind to the template thereby effectively blocking the non-specific binding sites. Using this approach, selectivity of the target analyte lysozyme to the recognition sites increased by an order of magnitude. Additional modifications of

MIP synthesis either through dummy templates or additional polymerization steps will likely lead to more selective and sensitive recognition capabilities in sensor applications.

Recognition of small molecules using MIPs can also be improved by mechanical grinding and sieving to improve polymer particle uniformity. Traditionally, MIPs are synthesized in bulk, ground, and then sieved before use which leads to heterogeneous structures with a distribution of recognition sites.[47] Alternatively, purification of MIP particles is possible through the use of affinity column purification.[47,70] Hoshino and coworkers synthesized fluorescently labeled MIP particles templated with melittin that were passed through a melittin functionalized agrose bead column where retention of the MIP particles was dictated by the degree of template affinity for the agarose column.[47] After passing through the column, the eluted MIP particles were analyzed using fluorescence spectroscopy. Approximately 40% of the particles eluted from the column indicating no interaction with melittin. Washing the affinity column using 1 °C water facilitated the removal of the plastic antibodies from the column and revealed a K_d = 0.66 – 2.3 nM which is comparable to typical antibody-antigen interactions. All in all, affinity purification yielded MIP nanoparticles with a more narrow affinity distribution than unpurified polymer particles. Affinity purification can be applied to many different MIP-template systems and will likely become an integral step in plastic antibody template synthesis for biosensor applications.

Industrial applications of MIPs require an automated, direct, reproducible, and large scaled synthesis of high affinity plastic antibodies.[33,59] Piletsky *et. al*. proposed an automated MIP synthesis on an immobilized solid-phase template for the production of reproducible, high affinity MIP particles.[58,59] In the automated synthesis, MIP particles were polymerized around solid-phase immobilized templates where unreacted monomers and low binding affinity particles were easily removed with washing. Three unique MIP syntheses which took place over five days were found to exhibit similar binding properties ($K_d = 6.3 \times 10^{-8} \pm 1.7 \times 10^{-9}$ M).[58] In addition to producing high-affinity MIP

particles, solid-phase synthesis methods readily allowed for further surface modification with a variety of ligands for use in biosensing applications.[59] These high affinity MIP particles were functionalized with labels for fluorescence studies, electrochemical labels for cyclic voltammetry detection, or thiol groups for immobilization onto gold surfaces. The ease of surface modification on high-affinity MIP particles further improved biosensor integration for industrial applications.

1.4 Incorporating Plastic Antibodies into Nanosensors towards Real Applications

In recent years, the incorporation of nanomaterials into MIPs produced sensitive and selective biosensors. There are three methods to incorporate nanomaterials into MIP sensors: suspending nanomaterials into the MIP matrix, polymerizing nanoparticles into the MIP matrix, and polymerizing the MIP onto a nanomaterial surface. In addition to the method of nanomaterial incorporation into the MIP sensor, fundamental nanomaterial properties such as nanomaterial shape, size, surface chemistry, and stability in the MIP matrix must also be considered. Specifically, noble metal nanoparticle and MIP networks yielded selective detection of biomolecules,[71-75] drugs,[69,76-81] environmental contaminates,[82,83] and explosives.[84] Herein, noble metal nanomaterials and their incorporation into MIP electrochemical, fluorescence, SERS, and SPR sensors will be described.

1.4.1 Fluorescence MIP Sensors

Detection of biomolecules using fluorescence MIP sensors allows for rapid and selective solution-phase measurements.[72-75,85] Introduction of noble metal nanoparticles facilitates large changes (increases or decreases depending on the mechanism) in fluorescence signals yielding highly sensitive and selective biosensors.[72-75] For instance, Gültekin and coworkers polymerized a MIP layer onto organically modified gold nanoparticles for the sensitive and selective detection of dipicolinic acid, a main

component of *Bacillus* spores where some of its species are attributed to bioterrorism (*Bacillus anthracis*) and food poisoning (*Bacillus cerus*).[73]

This was achieved in a multi-step process. First, gold nanoparticles were functionalized with methacryloylamidocysteine. Next, a dipicolinic acid MIP was polymerized around the gold nanoparticles producing a MIP nanoshell. After the removal of the template molecules, target dipicolinic acid was added, and the fluorescence intensity decreased significantly via photoluminescence quenching from the gold nanoparticle through specific interactions with dipicolinic acid in the MIP binding sites.[73,74] Fluorescence emission spectra at 600 nm were collected after incubating the MIP nanoshell in $0 – 1 \times 10^{-4}$ M dipicolinic acid solutions which resulted in a detection limit of 0.1 μM dipicolinic acid (spore concentration = 3.2×10^{4} CFU mL^{-1}). The MIP nanoshells were then used to quantify dipicolinic acid in *Bacillus cerus* spore samples. This integration of MIPs and the photoluminescence properties of gold nanoparticles yielded promising results toward the rapid and sensitive detection of *Bacillus cerus* spores for food safety applications.

Since this work, development of fluorescence MIP sensor applications continued.[72,75] Fluorescence MIP nanobiosensor responses can be magnified by incorporating silver nanomaterials.[72,75] For example, silver coated gold nanoclusters were functionalized with methacryloylamidocysteine and coated with a dipicolinic acid MIP.[72] After the dipicolinic acid MIP cluster and non-imprinted nanoclusters were polymerized and prepared for sensor use, dipicolinic acid (concentration = $10^{-7} – 10^{-4}$ M) solutions were allowed to incubate with the samples. As expected, the fluorescence intensity decreased systematically for the MIP nanocluster but did not change for the non-imprinted nanocluster. The detection limit decreased by 1.5x for the gold/silver MIP nanocluster *vs*. the gold MIP nanoshell sensors.[72,73] While incorporation of noble metal nanoparticles into fluorescence MIP biosensors yielded selective biosensor responses,

sub-μM detection limits are typically required for trace biomolecule detection but were unrealized using this device.

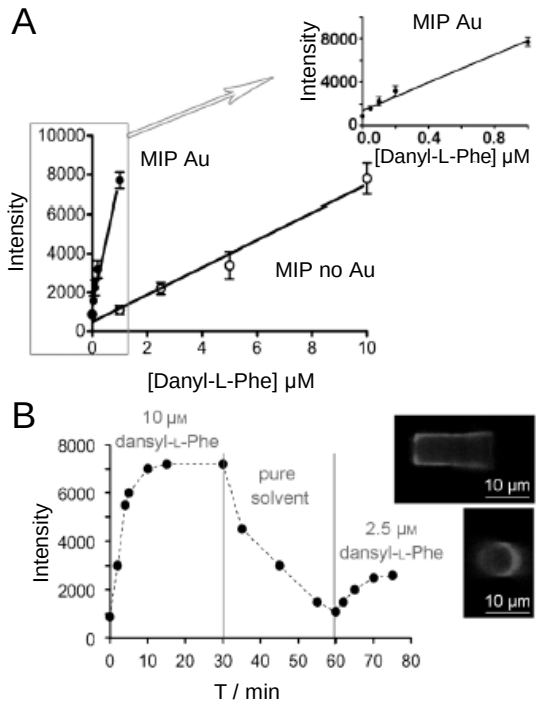

Figure 1.5. Fluorescence MIP sensor for dansyl-L-phenylalanine (dansyl-L-Phe). A) Fluorescence response of the MIP sensor tip without gold ("MIP no Au", λ_{EM} = 495 nm) and the composite gold-MIP tip ("MIP Au", λ_{EM} = 489 nm) after incubation with increasing concentrations of dansyl-L-Phe. Integration time: 100 ms. B) Kinetics of the fluorescence response of the thin-film MIP tip incubated with dansyl-L-phenylalanine. Inset: Confocal fluorescence image of the thin-film MIP tip after incubation. Experiments were performed in triplicate; error bars represent standard deviations. The blank signal was recorded before each set of experiments (adapted with permission from reference 85, Copyright 2013, Wiley).

Recently, Ton and et. al. demonstrated sub-μM detection limits of the fluorescent probe dansyl-L-phenylalanine with gold nanoparticles incorporated into a MIP functionalized optical fiber.[85] First, a molecular imprinted polymer was polymerized

onto an optical fiber tip with or without gold nanoparticles. Next, the fibers were incubated in dansyl-L-phenylalanine solutions (concentration = 0 – 10 μM) for 45 minutes, and the fluorescence response was measured (Figure 1.5A). Integrating gold nanoparticles into the MIP optical fiber sensor decreased the limit of detection *vs*. controls by a factor of 50 (1 μM to 20 nM). To decrease the incubation time required for sensing by decreasing the analyte diffusion distance, optical fibers with a thin (0.7 μm) MIP layer were fabricated. Binding of 10 μM dansyl-L-phenylalanine was observed within 2 minutes and fluorescence intensity saturated within 10 minutes (Figure 1.5B). In addition, the sensor was rinsed with solvent and subsequently used to detect 2.5 μM dansyl-L-phenylalanine. The reversibility of the sensor response indicated close to real-time detection of fluorescent molecules. While incorporation of noble metal nanoparticles into the fluorescence MIP optical fiber yielded sub-μM detection limits, a fluorescent functional monomer was required limiting the application of this optical fiber MIP biosensor.

1.4.2 Electrochemical MIP Sensors

In an effort to improve detection limits without the use of labeled monomers, MIPs can be combined with the simplicity, high sensitivity, and low-cost of electrochemical methods.[80] Incorporation of noble metal nanomaterials into electrochemical MIP sensors can increase the number of binding sites as well as the probability of electron transfer events between the electrode surface and analyte.[81] For instance, there are three methods to modify electrode surfaces with gold nanomaterials: direct deposition of gold nanoparticles on the electrode,86 electrode surface functionalization with ligands,[71,80,81] and nanoparticles grown directly onto the electrode.[83] Previously, gold coated silica MIP ($Au@SiO_2$) nanoparticles were synthesized and deposited onto a gold electrode surface for the electrochemical detection

of dopamine. Differential pulse voltammetry was used to detect 4.8 x 10^{-8} to 5.0 x 10^{-5} M dopamine (Figure 1.6A).[86] A systematic increase in the dopamine oxidation peak current was observed which resulted in a linear response and dopamine detection limits of 2.0 x 10^{-8} M (Figure 1.6B). Importantly, incubation of the Au@SiO_2 nanoparticle modified electrode in epinephrine, norepinephrine, ascorbic acid, and uric acid solutions exhibited smaller current response *vs*. dopamine which indicated high specificity of the MIP to dopamine.

While this study demonstrated the simplicity and specificity of MIPs, the performance of electrochemical MIP sensors depends on the adhesion and stability of the sensing layer to the electrode surface.[71] In an effort to overcome these sensor limitations, two devices were fabricated. First, the electrode surface was functionalized with a thiol anchoring agent for gold nanoparticle attachment and end groups which are then available for attachment to the dopamine MIP sensing layer. As a control, electrochemical sensors without a gold nanoparticle layer were also fabricated. After incubating both devices in 1 mM dopamine, the current was measured using square wave voltammetry. Current was enhanced by ~120 % when gold nanoparticles were incorporated into the MIP sensing layer *vs*. the control device by increasing electrical conduction between dopamine and the electrode surface. The gold nanoparticle MIP electrochemical sensor also exhibited improved dopamine detection limits (0.35 nM) *vs*. sensors without anchoring agents (20 nM).[71,86] The anchored gold nanoparticle MIP-electrochemical sensors further illustrated the advantages of integrating gold nanoparticles into MIP sensors for small molecule detection.

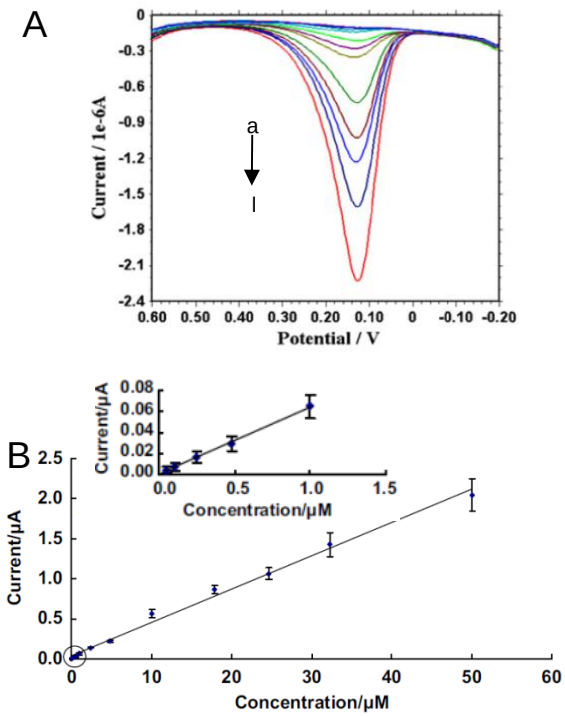

Figure 1.6. Electrochemical MIP sensor for dopamine quantification. (A) Differential pulse voltammograms of increasing dopamine concentration in 0.2 PBS (pH = 7.0). Dopamine concentration were (a) 0.05, (b) 0.1, (c) 0.3, (d) 0.5, (e) 1, (f) 2.5, (g) 4.8, (h) 10, (i) 17.9, (j) 24.6, (k) 32.4, (l) 50 μM (from top to bottom), respectively. (B) The response curve for dopamine. The inset reveals low dopamine concentration responses (reprinted from reference 86, with permission from Elsevier).

While MIP based sensors exhibit many sensing advantages, practical challenges in the wide-spread use of these remain. For instance, attaching gold nanoparticles to electrode surfaces with subsequent MIP polymerization requires multiple fabrication steps which can be time consuming.[71,86] To address this limitation, Li and coworkers proposed a one-step growth and electrodeposition of gold nanoparticles to an electrode procedure using a silica imprinted hydrogel templated with p-nitrophenol.[83] The one-step synthesis yielded an imprinted silica gel with well-dispersed gold nanoparticles onto a gold coated electrode. Cyclic voltammetry promoted template extraction by scanning the

potential from +0.6 and -1 V (three times) effectively disrupting the interactions between p-nitrophenol and the binding sites. Next, the current at +0.12 V was measured using differential pulse voltammetry for sensors incubated in p-nitrophenol (concentration = 3.0 x 10^{-8} – 3.5 x 10^{-4} M). Plotting the voltammetric magnitude *vs*. p-nitrophenol concentration yielded a linear response with a detection limit of 5.0 x 10^{-9} M. In addition, the molecular imprinted silica gel exhibited a 6-fold enhancement *vs*. non-imprinted controls. This one-step electrochemical nanoparticle MIP sensor approach could be applied to many different MIP-template systems which would reduce biosensor fabrication requirements.

1.4.3 SPR MIP Sensors

While electrochemical MIP sensors exhibit low detection limits (10^{-9}) and selectivities, real-time detection is not always possible. Alternatively, SPR MIP sensors exhibit real-time sensing capabilities and have been used to rapidly and selectively detect biomolecules,[87,88] drugs,[89] explosives,[90,91] and proteins.[92,93] MIPs can be incorporated into SPR sensors by coating an SPR surface with MIP,[89,93] embedding nanomaterials in a MIP matrix,[87,88] or polymerizing nanoparticle crosslinked MIPs onto an SPR surface.[90,91] For instance, a MIP SPR sensor successfully quantified lysozyme, a model protein, by first immobilizing lysozyme imprinted MIP particles to a gold surface and measuring the change in refractive index through changes in the SPR response in 21 – 1400 nM lysozyme.[93] The lysozyme MIP SPR sensor was shown to selectively detect lysozyme in a complex protein mixture in 45 minutes which is ~5x faster than quartz crystal microbalance measurements.

The detection limits of the MIP SPR sensors can be further improved by crosslinking Au nanoparticles around a template to form a gold nanoparticle MIP which is then immobilized on a SPR surface.[90,91] Specifically, gold nanoparticles are first functionalized with thioaniline electropolymerizable units and are then

electropolymerized on a thioaniline-monolayer-modified Au electrode in the presence of hexahydro-1,3,5-trinitro-1,3,5-triazine to form a bisaniline-crosslinked gold nanoparticle SPR sensor. Upon template binding, the π-donor bisaniline units associate with the π-acceptor nitro groups of the hexahydro-1,3,5-trinitro-1,3,5-triazine. The charge-transfer complexes in the nanoparticle matrix resulted in an amplified shift in the SPR spectrum. As expected, an immediate and systematic shift in the SPR curve occurred after treating the SPR sensor with 0 -10 μM hexahydro-1,3,5-trinitro-1,3,5-triazine resulted in a detection limit of 4 nM.[91] Additionally, the use of a more soluble, "dummy" template (Kemp's Acid) decreased the detection limits of hexahydro-1,3,5-trinitro-1,3,5-triazine to 12 fM as a result of the increased number of templates sites in the MIP matrix.

Riskin and coworkers further investigated the role of the "dummy" template structure in the bisaniline-crosslinked gold nanoparticle SPR sensor sensitivity by varying the template carboxylic acid for the detection of the explosives pentaerythritol tetranitrate, nitroglycerin, and ethylene glycol dinitrate.[90] For example; when citrate is employed as the template, the sensitivity is 200 fM for the structurally similar pentaerythritol tetranitrate. Nitroglycerin and ethylene glycol dinitrate, however, exhibited sensitivities of 100 pM, and 400 nM, respectively, in the citrate template MIP. The differences in sensitivity indicated that that the structure of the template molecule and resulting binding site is vital for selective detection of explosives. The decreased detection limits will likely lead to increased applications of gold nanoparticle MIP SPR sensors for explosives detection.

1.4.4 SERS MIP Sensors

While SPR sensors exhibit low detection limits (10^{-15}), the sensors were plagued with non-specific molecule responses. To combat this detection limitation, SERS can be utilized for molecular identification by combining MIP sensors with narrow and unique Raman vibrational bands.[69,76-79,82,84] Previously, MIPs were polymerized directly onto

patterned SERS-active grids for the detection of propranolol.[69,77,78] Droplets of MIP monomer were deposited onto SERS-active patterned grids using a nano fountain pen and polymerized. This resulted in MIP droplets with diameters of 6 - 12 μm.[69,77] SERS spectra were collected from the MIP droplet after polymerization, extraction, and rebinding of propranolol. The presence of the propranolol vibrational bands revealed identification of propranolol;[69,77] however, the thickness of the MIP droplet varied in each single droplet as well as from droplet to droplet limiting the quantitative detection of propranolol.[69,77,78]

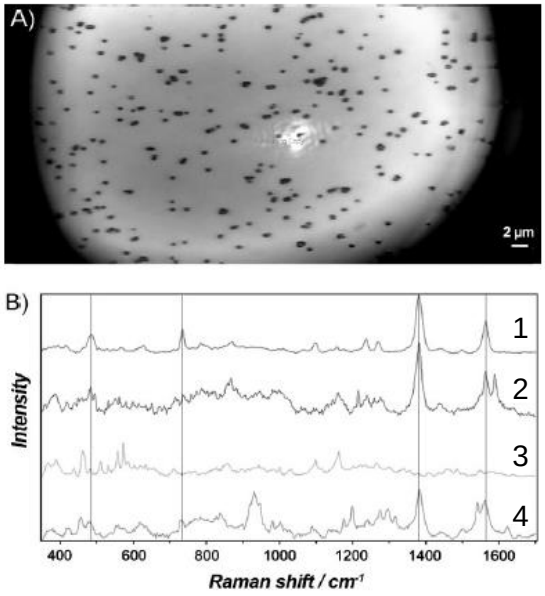

Figure 1.7. Development of a SERS MIP sensor. A) Optical microscopy image (100x magnification) of composite MIP particles during SERS measurements (defocused laser spot). B) SERS spectra of propranolol: 1) on aggregated gold colloids; 2) single composite MIP particle incubated in 10^{-5} M propranolol; 3) single composite MIP particle after washing with 9 methanol:1 acetic acid, followed by methanol to remove the propranolol; and 4) single composite non-imprinted polymer particle incubated in 10^{-5} propranolol (adapted with permission from reference 74, Copyright 2010, Wiley).

To facilitate quantitative detection using SERS MIP sensors, 2,4,6-trinitrotoluene imprinted xerogel films were fabricated on SERS substrates.[84] First, a MIP xerogel film was cast over the entire SERS substrate using spin coating, and template molecules were extracted. After extraction was verified, SERS spectra were then measured from solutions containing 0 - 0.6 mM 2,4,6-trinitrotoluene. Plotting the SERS intensity of the asymmetric nitrate stretch at 1352 cm^{-1} yielded a linear response over the concentration range and a detection limit of 3 x 10^{-6} M. In contrast to both fluorescence and electrochemical detection methods, unique vibrational bands of 2,4,6-trinitrotoluene allowed for both qualitative and quantitative detection even in the presence of structurally similar molecules. Unfortunately, the 2,4,6-trinitrotoluene MIP SERS sensor sensitivity was not adequate for sub-μM detection of trace explosives.

The small signals observed in the previous example were limited by either 1) the number of molecules near the SERS substrate and/or 2) the distance dependence of the SERS effect.[76,84] Clearly, polymerizing a thin MIP layer directly onto a nanoparticle surface can increase the number of template binding sites close to the metal surface thereby increasing biosensor sensitivity.[76,82] Bompart *et. al*. fabricated a MIP SERS sensor by functionalizing gold nanoparticles to carboxylate polymer particles and subsequently coated the composite with propranolol MIP shells (Figure 1.7A).[76] SERS spectra of the MIP composite (Figure 1.7B-2) and a control (Figure 1.7B-1) were collected after incubating the device in a 10^{-5} M propranolol solution. The presence of characteristic propranolol bands at 483, 733, 1380, and 1563 cm^{-1} indicated the presence of propranolol in the MIP composite. After the MIP composite was washed with (9 methanol:1 acetic acid), the propranolol vibrational bands were no longer observed (Figure 1.7B-3). In contrast, propranolol vibrational bands were observed for the non-imprinted polymer composite incubated in 10^{-5} M propranolol thereby indicating non-specific binding (Figure 1.7B-4). All in all, the MIP composite successfully demonstrated a lower detection limit (10^{-7} M) *vs*. the non-imprinted polymer composite (10^{-5} M) and

MIP particles (10^{-4} M). Additionally, the MIP composite facilitates successful quantification of propranolol in a complex biological matrix. The decreased detection limits using MIP composite SERS sensors will likely lead to more selective and sensitive recognition capabilities for biosensor applications.

1.5 Conclusions and Thesis Outline

In summary, biosensors facilitate quantification of a variety of biomolecules for clinical, industrial, and safety applications. Antibodies, aptamers, and DNA are widely used as recognition elements in affinity biosensors. The addition of noble metal nanomaterials to these devices improves signal transduction by allowing for numerous "enhanced" detection methods resulting in decreased assay times and detection limits *vs.* traditional immunoassays.

Furthermore, artificial recognition elements such as plastic antibodies were shown to mimic traditional receptors and were more environmentally stable, easier to synthesize, and cheaper than traditional antibodies. The incorporation of a purification step after MIP synthesis using affinity purification yielded high affinity MIP particles with a more narrow affinity distribution than unpurified MIPs for a particular molecule but resulted in a low yield of high affinity MIP particles. Finally, automated immobilized solid-phase template methods yielded reproducibly synthesized, high affinity MIP particles for industrial applications.

Further improvements in MIP sensor sensitivity were achieved with the addition of noble metal nanomaterials into electrochemical, fluorescence, SERS, and SPR detection platforms. Nanomaterial shape, metal, and surface functionalization were found to greatly impact signal enhancements in MIP biosensors. Additionally, decreasing the MIP sensing layer thickness significantly decreased the assay time required for sensitive detection. Specifically, fM detection limits with real-time detection were observed using a gold surface functionalized with a cross-linked nanoparticle MIP SPR sensor; however,

the SPR MIP sensor was plagued with issues of non-specific binding. To overcome inherent non-specific binding limitations of MIPs, molecular identification was achieved using SERS MIP sensors using both SERS-active substrates and solution-phase gold nanoparticles. Importantly, signal enhancements from nanomaterial incorporation required short distances between the nanomaterials and template sites which can ultimately limit quantitative detection. Tuning the polymer matrix allows for the sensitive and selective detection of a seemingly endless variety of analytes in complex, real-world applications.

In this dissertation, the synthesis and characterization of noble metal nanoparticles and drug-specific molecular imprinted polymers are demonstrated and applied toward the Raman and SERS-based detection of small molecules. This rigorous evaluation of primary nanoparticle formation and growth along with mechanistic studies of surface chemistry modification demonstrate key attributes regarding the resulting nanoparticle behavior in complex samples. Furthermore, these results along with spectroscopic characterization of MIPs and drug binding capacity studies serve as a foundation for a better mechanistic understanding of nanomaterial incorporation into MIPs for applications in Raman and SERS-based biosensors.

First, Chapters 2 and 3 describe the optimization, characterization, and modeling of primary gold nanoparticle nucleation and growth as well as surface functionalization via self-assembled monolayers. Specifically, Chapter 2 systematically investigates the implications of varying citrate concentration during gold nanoparticle synthesis. Implications of ionic double layer effects during nanoparticle growth yield either heterogeneous (in terms of crystallinity, shape, and/or size) or homogeneous nanomaterials. Chapter 3 focuses on the synthesis and characterization of thioctic acid functionalized gold nanoparticles. Lowering the ionic strength of the solution during molecular self-assembly promotes large electrostatic interfacial energies between

molecules thereby relatively reducing monolayer densities and worsening nanoparticle stability.

Next, Chapter 4 explores the synthesis, characterization, and binding capacity of methacrylate-based MIPs for specific recognition of three drugs commonly used to treat migraines. Specifically, acetaminophen, aspirin, and caffeine templated MIPs are synthesized, extracted, characterized, and used to quantitatively and directly detect over-the-counter drugs in complex samples using Raman microscopy. Because MIP selectivity often limits real-world use of these materials as recognition agents in mixtures, detection specificity is improved via the narrow and unique vibrational bands observed using Raman microscopy. Methods which overcome some of the traditional limitations of MIPs for sensor applications are evaluated for the successful detection and quantification of three drug molecules in mixtures as well as in an over-the-counter migraine medication sample.

Because Raman microscopy results in high linear dynamic ranges (mM – M are standard), Chapter 5 examines how the concentration of CTAB stablizied gold nanorods influences surface-enhanced Raman scattering (SERS) responses of the same drugs using MIPs as pre-concentration and recognition elements. This combination of materials, theory, and application forms a solid foundation which should aid in the design and development of MIP nanobiosensors for specific and sensitive detection in complex matrices. Chapter 6 presents the conclusions and future directions of Raman-based nanobiosensors using plastic antibodies as artificial recognition elements. This promising approach is envisioned to provide a viable alternative to traditional recognition agents for assays where long reagent shelf-lives and low reagent costs are necessary to achieve the detection goal. Improved nanomaterial homogeneity coupled with modest MIP recognition abilities and the water-compatible and finger-printing capabilities of Raman microscopy facilitate this exciting sensor foundation which could be extended to solve problems in biology, environmental science, forensics, and medicine.

CHAPTER 2 IMPLICATIONS OF CITRATE CONCENTRATION DURING THE SEEDED GROWTH SYNTHESIS OF GOLD NANOPARTICLES

2.1 Introduction

In recent years, the tunable chemical and physical properties of nanoparticles are more easily exploited because of improvements in direct[94] and seeded[95] growth synthetic techniques which yield discrete nanomaterial sizes with various shapes (i.e. spheres,[94] rods,[96] and nanoflowers[97]). In all cases, the stability of a solution-phase nanostructure depends on its overall Gibb's free energy, which is dictated by inherent structural properties (i.e. crystallinity, shape, size) and external environment (i.e. ionic strength, pH).

During nanoparticle growth, atom lattice reorganization results in reduced numbers of internal and surface defects thereby minimizing the overall energy and surface tension of the system.[98] To further decrease nanoparticle free energy, capping agents such as citrate or cetyltrimethylammonium bromide (CTAB) can bind preferentially to the relatively higher energy crystal planes and if this occurs during growth, asymmetric nanoparticle morphologies will develop.[95] Moreover, the ionic speciation of the nanoparticle solution will influence the double layer thickness on the nanoparticle which improves its stability by reducing its surface tension but can interrupt and reduce the uniform flux of growth species to these same surfaces.

[1] Adapted from *Implications of Citrate Concentration during the Seeded Growth Synthesis of Gold Nanoparticles*, Anna A. Volkert, Varuni Subramaniam, and Amanda J. Haes, Chemical Communications, **2011**, 47, 478-480.

Once synthesized, nanoparticle stability will dictate their ultimate usefulness for applications, shelf-life, as well as their chemical and physical properties. As a result, various methods are used to monitor the stability of nanostructures. Flocculation parameter studies,[99] for instance, yield semi-quantified information by monitoring a size-dependent chemical or physical property of a nanomaterial as a function of time and/or solution pH.[99,100]

Herein, we report a novel strategy to vary gold nanoparticle structure and resulting stability in solution by varying citrate concentration during seeded growth syntheses. Citrate stabilized gold (Au@citrate) nanoparticles with a relative standard deviation (RSD) less than 10% were considered monodisperse.[101] Increasing the citrate concentration during the seeded growth synthesis of gold nanoparticles yields materials with decreased aspect ratios and increased defect densities. The stability of these nanoparticles is attributed to variations in their overall Gibb's free energy. Better control of nanomaterial growth conditions will provide important insights into the behavior of the nanoparticles for their integration in various biological applications.

2.2 Experimental

2.2.1 Seeded Growth Synthesis of Au@Citrate Nanoparticles

The nanomaterials are synthesized in three steps. First, gold nanoparticle seeds are synthesized using standard citrate reduction techniques.[94] The as-synthesized seeds (diameter, d = 10.8 ± 0.8 nm, number of samples analyzed, N = 225) are diluted with Nanopure water (18.2 MΩ cm^{-1}) and grown via the addition of gold salt and hydroxylamine hydrochloride (reducing agent).[94] The first generation seeds are

monodisperse (d = 18.0 ± 1.8 nm, N = 203). Next, six second generation gold nanoparticle samples are synthesized from the first generation nanoparticles. For each sample, 6.25 mL of freshly synthesized first generation nanoparticles are diluted with 18.7 mL water to a final nanoparticle concentration of ~0.2 nM. Citrate, a stabilizing agent, is then added to 25 mL of ~0.2 nM first generation nanoparticles to this solution in incremental concentrations (0.10, 0.30, 0.50, 0.70, 0.90, or 1.10 mM) using either a 0.10 or 2.0 M sodium citrate tribasic dihydrate stock solution. Next, 200 mM hydroxylamine hydrochloride (141 μL) is added to the nanoparticle solution and allowed to equilibrate. After 15 minutes, the pH of the nanoparticle solution is measured (Table 2.1) and 250 μL $HAuCl_4$ (1% w/v) is added and stirred for at least four hours in the dark at room temperature to ensure equilibrated nanoparticle growth.

2.2.2 Ionic Strength Calculations During Seeded Growth

Using the measured pH values, the ionic strengths of each sample was calculated (Table 2.1) using the following equation:

$$\text{Ionic Strength} = \mu = 0.5 \sum c_i z_i^2 \quad (1)$$

where c_i is the concentration of the *i*th species and z_i is its charge.

The ion concentrations were determined using the following pertinent equilibria for sodium citrate in water:

$$H_3cit \leftrightarrow H_2cit^- + H^+ \qquad K_{a1} = 7.44 \times 10^{-4}$$

$$H_2cit^- \leftrightarrow Hcit^{2-} + H^+ \qquad K_{a2} = 1.73 \times 10^{-5}$$

$$Hcit^{2-} \leftrightarrow cit^{3-} + H^+ \qquad K_{a3} = 4.03 \times 10^{-7}$$

The concentration ratio between the predominant citrate species at the measured pH for each second generation sample was determined using the Henderson-Hasselbalch equation. Next, the concentration of the predominant citrate species was estimated by considering the total sodium citrate concentrations added (and diluted). The calculated concentrations and ion charges were used in equation 2.

When determining the concentrations for the NH_3^+OH, Cl^-, Na^+, H^+, and OH^-, the following equilibra were considered.

$$NH_3^+OH \leftrightarrow NH_2OH + H^+ \qquad K_a = 1.1 \times 10^{-6}$$

The Henderson-Hasselbalch equation was used to calculate the concentration ratio between the acid and base forms of the molecule. The concentration of each species was then calculated using the total NH_3^+OH present in the second generation samples. Both the NH_3^+OH remaining after the reduction reaction in the first generation synthesis and NH_3^+OH added during the second generation were included. Total Cl^- concentration was calculated by accounting for the Cl^- from the $HAuCl_4$ in the seeds and first generation synthesis and $NH_3^+OH{\cdot}HCl$ added in each step. This concentration of chloride remained constant at 1.90_2 mM for all samples studied. Total Na^+ concentration was determined by accounting for the sodium citrate added during each synthesis. Finally, the measured pH was used to calculate the H^+ concentration and the dissociation of water equilibrium was applied to estimate the OH^- concentration.

Table 2.1. Measured pH and calculated ionic strength for the various nanoparticle samples

Sample	[Citrate] (mM)	pH	Ionic Strength (mM)
1	0.10	3.47	2.07
2	0.30	4.31	2.45
3	0.50	4.64	3.05
4	0.70	4.97	3.77
5	0.90	5.13	4.46
6	1.10	5.55	5.34

As a result, the ionic strength for the second generation sample is as follows:

$$\mu = 0.5[c_{H_3cit} \cdot z_{H_3cit}^2 + c_{H_2cit^-} \cdot z_{H_2cit^-}^2 + c_{Hcit^{2-}} \cdot z_{Hcit^{2-}}^2 + c_{cit^{3-}} \cdot z_{cit^{3-}}^2 + c_{NH_3^+OH} \cdot z_{NH_3^+OH}^2 + c_{Cl^-} \cdot z_{Cl^-}^2 + c_{Na^+} \cdot z_{Na^+}^2 + c_{H^+} \cdot z_{H^+}^2 + c_{OH^-} \cdot z_{OH^-}^2] \quad (2)$$

Using equation 2, the ionic strength was calculated for the second generation samples (Table 2.1). Throughout nucleation and growth, no ions were removed (until optical and stability characterization was performed).

2.2.3 Transmission Electron Microscopy (TEM)

The aspect ratio, homogeneity, and mean diameter of the nanoparticles were characterized using TEM (JEOL JEM-1230). Samples were prepared by applying 30 μL of a diluted nanoparticle solution (50% mixture in ethanol) to a carbon Formvar coated copper grid (400 mesh, Electron Microscopy Sciences, Hatfield, PA). Excess solution was removed with filter paper, and the sample was allowed to dry. The resulting images were analyzed using Image Pro Analyzer, and at least 100 nanoparticles were evaluated per sample.

2.2.4 Extinction Spectroscopy

Extinction spectra of Au@Citrate nanoparticles were acquired using a UV-visible spectrometer (Ocean Optics HR4000) configured in transmission geometry. Before acquiring spectra, samples were washed three times (2,773 xg for 20 - 25 minutes) in water (pH adjusted to 11 with NaOH) and suspended in 3.0 mS cm^{-1} sodium phosphate (pH = 12). All spectra were collected in disposable methacrylate cuvettes (path length = 1 cm) using the following parameters: integration time = 20 msec, average = 20 scans, and boxcar = 10.

2.2.5 Nanoparticle Flocculation Measurements

To monitor flocculation, gold nanoparticles were centrifuged, and redispersed in 3.0 mS cm^{-1} sodium acetate and phosphate buffer (pH 4and pH 12, respectively). The citrate concentration in all samples is maintained at ~0.02 mM after centrifugation. The solution was stirred, and extinction spectra were collected every 5 seconds. Spectra collected in pH 4 buffer were baseline adjusted and normalized to the spectra collected in the pH 12 buffer to account for slight variations in spectrometer function and nanoparticle concentration. Integrated areas were calculated from these normalized spectra (from ~600 – 800 nm) collected in pH 4 buffer and plotted as a function of time. The maximum flocculation time was determined by taking the first derivative of the flocculation curves.

3.3 Results and Discussion

2.3.1. TEM analysis of Au@Citrate Nanoparticles

Representative transmission electron microscopy (TEM) images and analysis of seed, first, and second generation gold nanoparticles are found in Figure 2.1 and Tables 2.2 and Table 2.3. Qualitative and quantitative inspections of these TEM data reveal that shape and size homogeneity varies among the six second generation nanomaterials. In all cases, the minimum, mean, and maximum nanoparticle dimensions as well as the mean aspect ratios are evaluated (including standard deviations and percent relative standard deviations (% RSD)).

Several important trends are noted. First, the average nanoparticle size for all six samples is ~30 nm. Second, gold nanoparticles grown in the presence of 0.10, 0.30, and 0.50 mM citrate contain a small population of rod-like structures with aspect ratios greater than 2 (8 %, 7 %, and 2 %, respectively) whereas no rod-like structures are observed for materials grown in 0.70, 0.90, and 1.10 mM citrate (Figure 2.2). Above 1.10 mM citrate concentrations, spherical but heterogeneous nanoparticles (% RSD > 30%) form (data not shown). Third, the average aspect ratio for the six second generation

nanoparticle samples are 1.30 (±33 %), 1.27 (±31 %), 1.22 (±16 %), 1.16 (±6 %), 1.13 (±4 %), and 1.13 (±6 %) for 0.10 to 1.10 mM citrate concentrations.

Table 2.2. TEM analysis of second generation nanoparticles prepared in 0.10 – 1.1 mM citrate solutions.

Sample	[Citrate] (mM)	Mean Diameter (nm)	Mean Aspect Ratio	Aspect Ratio >2	N
1	0.10	31.0 ± 2.7 (9 %)	1.30 ± 0.43 (33 %)	8 %	138
2	0.30	31.4 ± 2.6 (8 %)	1.27 ± 0.39 (31 %)	7 %	146
3	0.50	30.2 ± 2.6 (9 %)	1.22 ± 0.20 (16 %)	2 %	131
4	0.70	30.3 ± 3.0 (10 %)	1.16 ± 0.07 (6 %)	0 %	129
5	0.90	28.4 ± 3.8 (13 %)	1.13 ± 0.04 (4 %)	0 %	110
6	1.10	30.4 ± 4.1 (13 %)	1.13 ± 0.05 (6 %)	0 %	114
Control[a]	0.10	32.2 ± 3.4 (11 %)	1.27 ± 0.37 (29 %)	6 %	119

[a] The control sample was grown in the presence of 0.10 mM citrate and pH 4.97.

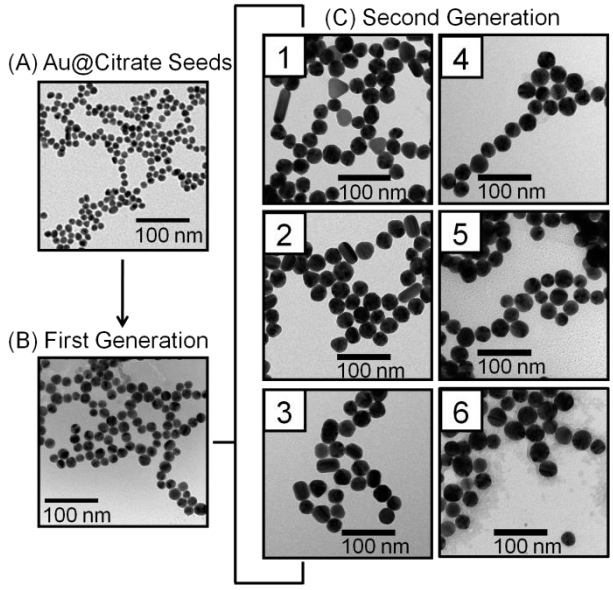

Figure 2.1. Representative TEM images. (A) Au@citrate nanoparticles (d = 10.8 ± 0.8 nm), (B) first generation nanoparticles (d = 18.0 ± 1.8 nm), and (c) second generation nanoparticles prepared in (1) 0.1, (2) 0.3, (3) 0.5, (4) 0.7, (5) 0.9, and (6) 1.1 mM citrate concentrations, respectively.

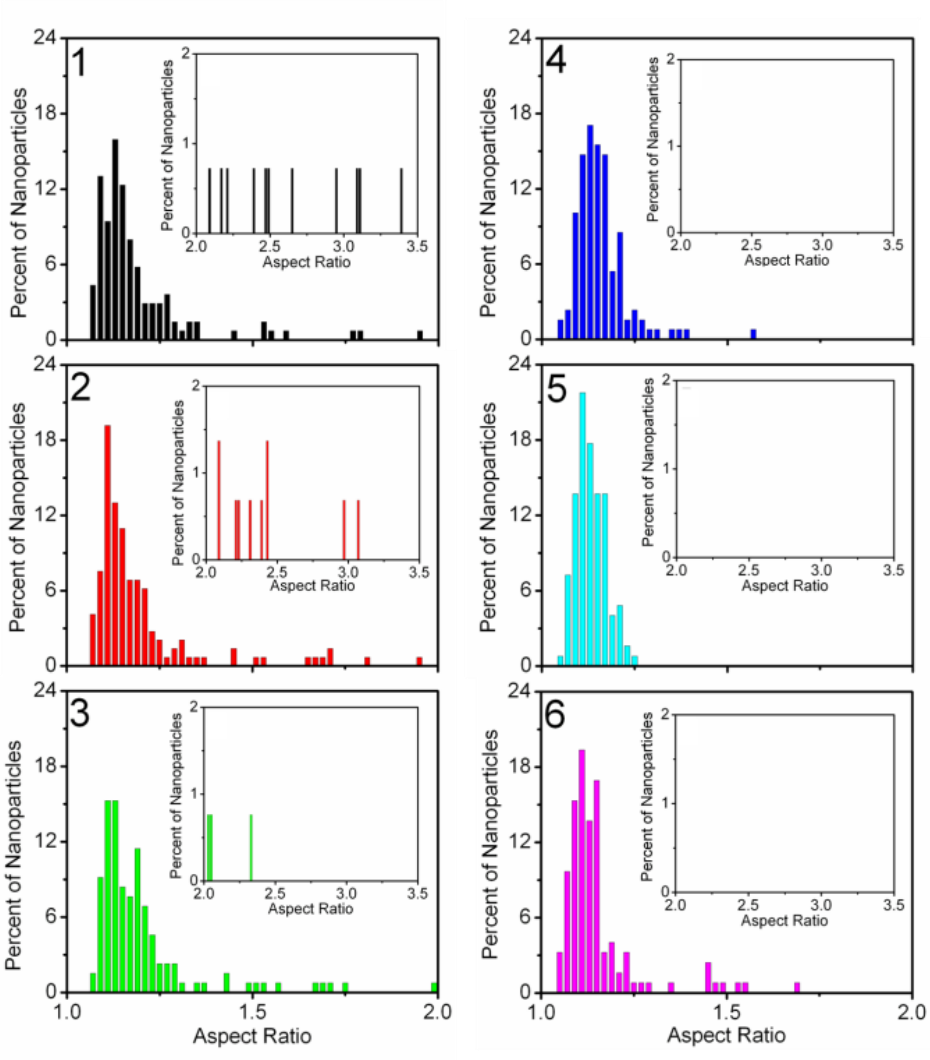

Figure 2.2. Histograms containing the aspect ratios for nanoparticles grown in the presence of 0.10, 0.30, 0.50, 0.70, 0.90, or 1.10 mM citrate for samples 1 – 6, respectively. The insets reveal the distribution of nanoparticles with an aspect ratio value greater than 2 which are (1) 8 %, (2) 7 %, (3) 2 %, (4) 0 %, (5) 0 %, and (6) 0%.

These data suggest that citrate (the stabilizing agent) and/or solution pH influence the homogeneous growth of gold nanoparticles. Previous studies revealed that as the $AuCl_4^-$ to NH_2OH ratio decreased[95] or solution pH increased (3.5 - 7.5),[102] nanoparticle homogeneity improved. To understand the role of citrate and/or pH in homogeneous growth syntheses, a control study was performed where nanoparticles were grown in the

presence of 0.10 mM citrate (most heterogeneous sample) at pH = 4.97 (pH of most homogeneous sample). The pH was adjusted using 1.00 M NH_4OH. Interestingly, this control sample yielded similar structures to the nanoparticles grown in 0.10 mM citrate (Figure 2.3). Analysis of these data are summarized in Table 2.2 and reveal that ~6 % of rod-like structures with aspect ratios greater than 2 and a mean aspect ratio of 1.27 (±29 %) form, thereby indicating that citrate concentration is more important than pH for homogeneous nanostructure growth in these conditions.

Clearly, citrate stabilizes nanoparticles during growth by impacting double layer properties and/or the inherent rate of gold reduction by hydroxylamine on the nanoparticle surface. Regardless of concentration, citrate preferentially adsorbs onto the gold nanoparticle surface vs. other ions in solution (i.e. $AuCl_4^-$, Cl^-, etc.). At low (< 0.70 mM) citrate concentrations, the formation of nanoparticles with aspect ratios greater than 2 indicate faceted growth. At higher citrate concentrations, no nanoparticles with aspect ratios greater than 2 are observed but the heterogeneity, as measured by the % RSD in the mean diameters of the resulting structures, increases.

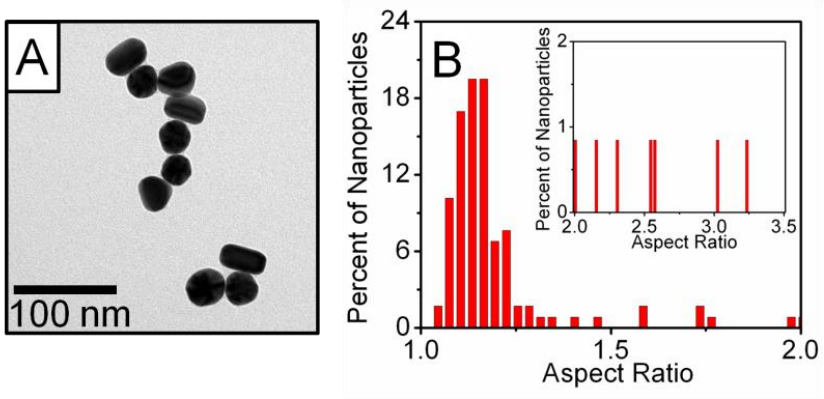

Figure 2.3. Characterization of the control sample. (A) Representative TEM image and (B) aspect ratio ratios (1.27 ± 0.37, N = 119) for the sample. The percent of nanoparticles with an aspect ratio greater than 2 is 6 %.

2.3.2 Optical Characterization of Second Generation Gold Nanomaterials

To further investigate subsequent impacts of citrate present during nanoparticle growth, the optical properties of the nanoparticles are monitored using extinction spectroscopy. Extinction spectra of gold nanoparticles are a measure of the localized surface plasmon resonance (LSPR) which will vary predictably based on the composition, shape, size, and homogeneity as well as the local dielectric environment surrounding the nanostructures.[63] Only nanoparticle samples grown where no rod-like nanostructures formed are evaluated (citrate concentrations = 0.70 – 1.10 mM). These samples are centrifuged, washed in water (pH adjusted to 11 with NaOH) to remove excess citrate from the nanoparticle solution, and suspended in pH 12 buffer (sodium phosphate, conductivity 3.0 mS cm^{-1}) to ensure a consistent dielectric environment.

The three second generation gold nanoparticle samples all exhibit similar extinction maxima, λ_{max}, which are centered at ~520 nm (Figure 2.4). Closer evaluation of these data, however, reveals slight differences in the LSPR peak widths (full width at half maxima, Γ). As citrate concentration increases from 0.70, 0.90, to 1.10 mM, the Γ systematically increases from 102 nm, 106 nm, to 114 nm, respectively. Because the average extinction maxima among the samples are statistically similar, this slight dampening or broadening of the LSPR band is likely attributed to increased electron scattering in the nanostructures – a phenomenon which arises with increased surface and internal defects.[103]

To understand why LSPR dampening is occurring, the Debye length present during nanoparticle growth is calculated using the ionic strengths found in Table 1 and the Debye-Hückel parameter.[104] For nanoparticles grown in 0.70, 0.90, and 1.10 mM citrate concentrations, Debye lengths are 11.5, 10.1, and 9.2 nm, respectively. As the citrate concentration increases, the Debye length decreases by compressing the double layer and increasing the association of citrate with the gold surface. As the degree of

interaction between a capping agent (citrate) and the metal surface increases, metal reduction will be limited in the growth plane.[105] We hypothesize that citrate at relatively higher concentrations likely disrupts the flux of $AuCl_4^-$ to the seed nanoparticle during growth which results in more internal and/or surface defects, and as a result, induces plasmon dampening.

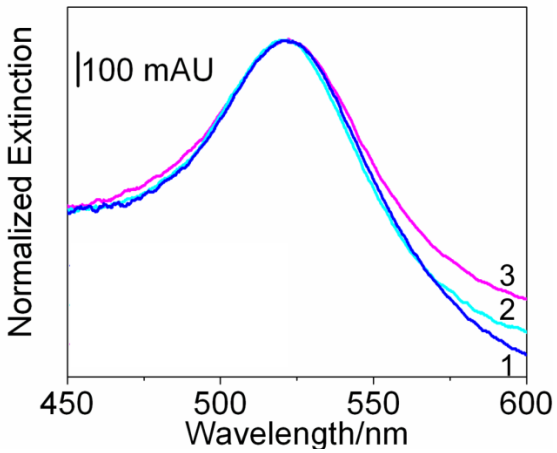

Figure 2.4. Extinction spectra for Au nanoparticles grown in the presence of (1) 0.70, (2) 0.90, (3) 1.10 mM citrate. The λ_{max} and Γ is 519.7 nm and 102.3 nm, 519.1 nm and 105.8 nm, and 522.1 nm and 113.6 nm for Au nanoparticles grown in in the presence of 0.70, 0.90, and 1.10 mM citrate, respectively.

2.3.3 Evaluation of Au@Citrate Nanoparticle Stability

If citrate impacts both nanoparticle structure (morphology) and atomic defect density, then the stability of nanoparticles grown in these studies could vary. As a result, nanoparticle stability is semi-quantified using flocculation parameter estimations. To collect these data, nanoparticles are centrifuged and resuspended in 3.0 mS cm^{-1} sodium phosphate buffer (pH 4 and 12) three times. The citrate concentration in all the samples is maintained at ~0.02 mM after centrifugation. TEM is used to evaluate structural

differences for the nanostructures before and after centrifugation. With the exception of nanoparticles grown in the presence 0.10 mM citrate, statistically similar nanoparticle structures are observed. As a result, the nanoparticle sample grown in the presence of 0.10 mM citrate was not evaluated for stability (Figure 2.5).

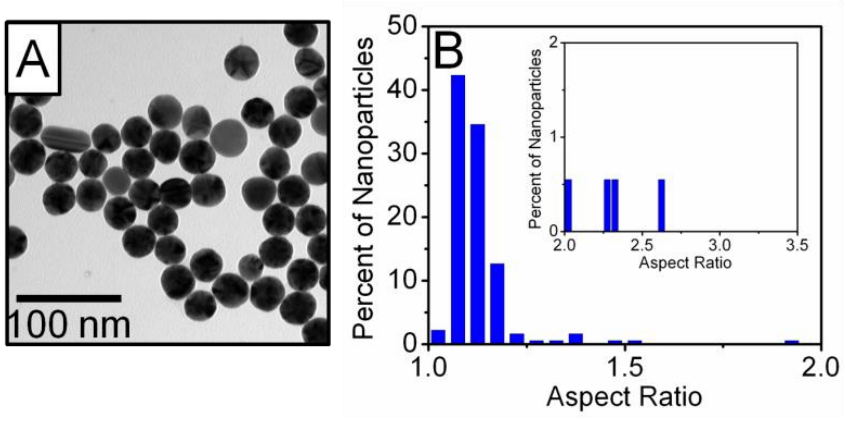

Figure 2.5. Characterization of second generation gold nanoparticles grown in the presence of 0.10 mM citrate after centrifuging once at 2773 x g for 25 minutes. (A) Representative TEM image (d_{max} = 33.1 ± 3.8 nm, d_{min} = 29.0 ± 2.9 nm, d_{mean} = 31.0 ± 2.5 nm, N = 182) and (B) aspect ratio analysis (1.15 ± 0.20, N = 182) for this sample. The percent of nanoparticles with an aspect ratio greater than 2 is 2 %.

To monitor flocculation, extinction spectra were collected every 5 seconds for 5 minutes. Spectra collected at 2.5 minutes for the pH 4 buffer were baseline adjusted and normalized to the spectra collected in the pH 12 buffer to account for slight variations in spectrometer function and nanoparticle concentrations. For example, Figure 2.6A reveals the time dependent LSPR spectra of gold nanoparticles grown in the presence of 0.70 mM citrate. As flocculation increases, the extinction intensity at 520 nm decreases while a new lower energy band centered at 650 nm intensifies. After 100 seconds, the extinction intensities which correspond to both wavelengths decrease denoting

irreversible nanoparticle aggregation and precipitation which is consistent with Figure 2.6. Similar behavior was observed for all of the nanoparticle samples.

Next, the integrated area between ~600 – 800 nm was calculated using Grams AI to quantify the degree of nanoparticle flocculation as a function of time (Figure 2.7). Nanoparticle flocculation increases with time (at pH 4) and at different rates for the various nanoparticle samples. In order to compare the various nanoparticle samples, the first derivative of the flocculation curves were computed and plotted vs. citrate concentration (Figure 2.6B).

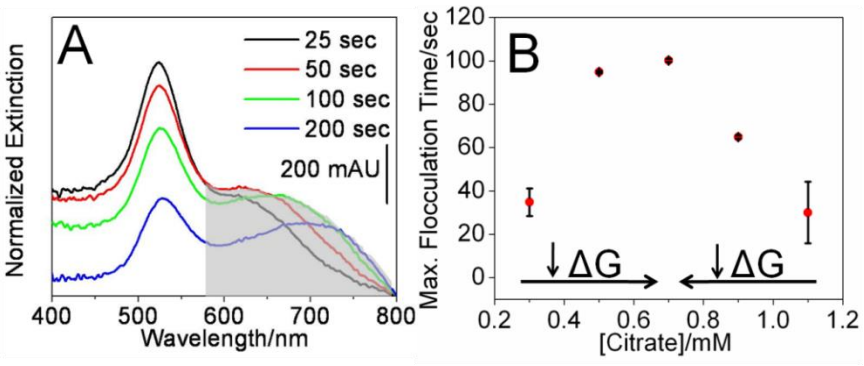

Figure 2.6. Optical characterization of second generation Au nanoparticles. (A) Normalized extinction spectra for second generation gold nanoparticle sample prepared in 0.7 mM citrate when exposed to pH 4 buffer over time. Shading indicates area of integration for flocculation calculations. (B) Time of peak flocculation for second generation samples prepared in 0.3 – 1.1. mM citrate. The arrows represent decreasing Gibbs free energy (ΔG). The error bars were determined by calculated the standard deviation of 30 seconds before and after the flocculation peak maximum.

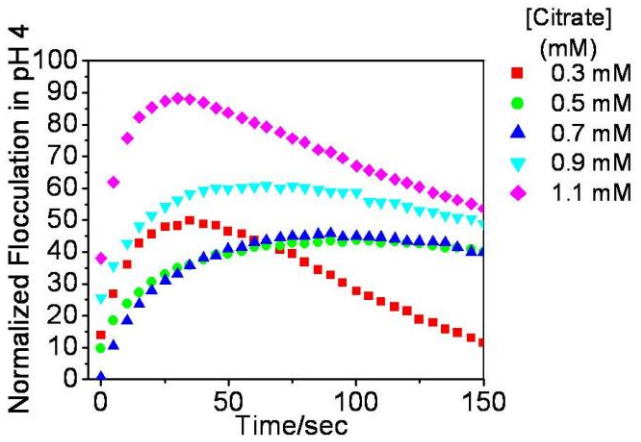

Figure 2.7. Normalized flocculation parameters for the various nanoparticle sample incubated in pH 4 as a function of time.

Two important trends are observed in these data. First, nanoparticle samples which contained rod-like nanoparticles (aspect ratios >2), flocculated within ~1.5 minutes. We attribute this result to the relatively high Gibb's free energy (i.e. surface tension) of rod-like structures vs. spheres.[106] Second, for the three nanoparticle samples which did not contain rod-like structures with aspect ratios greater than 2 but exhibited similar mean diameters and extinction maxima wavelengths, the time required to achieve maximized flocculation increased with decreased citrate concentration present during growth. As indicated previously by the LSPR dampening studies, increased internal and/or external atomic defect densities are likely forming with increased citrate concentrations. We hypothesize that as the degree of defects in the nanoparticles increases, the surface energies of the resulting nanostructures also increase.[107] Because the nanoparticle sample grown in 0.70 mM citrate exhibited the narrowest LSPR band, defect density and as a result, Gibb's free energy is minimized yielding the most stable sample studied.

2.4 Conclusions

In summary, gold nanoparticles were grown in the presence of varying citrate concentrations. Citrate stabilized these nanostructures during growth and impacted the overall solution pH and ionic strength. We observed that increased citrate concentrations initially reduced the population of rod-like structures (aspect ratios > 2). In comparison to previous studies, citrate concentration rather than pH was found to dominate the formation of these rod-like structures. Between citrate concentrations of 0.70 – 1.10 mM, no rod-like structures formed; however, the LSPR band of these samples dampened with increased citrate concentration. This spectroscopic characterization suggested that the number of internal and/or external atomic defects was increasing. This hypothesis was further supported via time-dependent flocculation studies which indicated that the materials with the most dampened LSPR properties were the most unstable nanoparticles evaluated. The thickness of the citrate-dominated Debye length likely impedes nanoparticle growth at the relatively higher citrate concentrations. It is known that aging of nanoparticles reduces the surface energy and defect density through atom reorganization;[108,109] therefore, future studies which evaluate trends in LSPR dampening and flocculation as a function of aging and solution temperature will further validate these findings.

CHAPTER 3 SALT-MEDIATED SELF-ASSEMBLY OF THIOCTIC ACID ON GOLD NANOPARTICLES

3.1 Introduction

Surface modification via self-assembled monolayers (SAMs) is revolutionizing how surfaces and interfaces are modified for applications in biosensors, biotechnology, chemical sensors, and molecular electronics.[110-121] A wide variety of ligands (i.e. amine, carboxylate, isocyanide, phosphine, and thiol)[122-127] form SAMs on gold films[110] and colloidal particles;[114,128-133] however, thiol/disulfide surface attachment groups are widely employed because of the strong bond that forms between gold and sulfur.[110] Self-assembly of alkanethiols onto a metal surface can occur in either organic[113,115,122] or aqueous[126,134,135] phases with the latter being predominate for solution-phase nanoparticles with diameters greater than 10 nm.[121,122,133,136] In all cases, the stability of solution-phase nanoparticles can be improved with SAMs thereby increasing their usefulness in biology, catalysis, and nanotechnology.[114,131,135-151]

Predictable utilization of thiol functionalized gold nanoparticles in any application relies on the reproducible assembly of SAMs on their surfaces. Alkanethiol chains composed of more than 10 carbon atoms produce SAMs which are more highly ordered and oriented with increased molecular packing densities than shorter chains.[152,153] These SAMs, however, generally contain at least three types of defect sites: pinholes, gauche defects in alkyl chains,[154] and collapsed-site defects which arise from (1) imperfect adsorption of alkanethiols during the self-assembly process, (2) thermally and tilt-order driven chain dynamics, (3) loss of thiols during rinsing, storage, and use.[152,155] For thiols on flat gold surfaces, the fraction of these defect sites to the total surface area is estimated

[1] Adapted from *Salt-mediated Self-Assembly of Thioctic Acid on Gold Nanoparticles*, Anna A. Volkert, Varuni Subramaniam, Michael Ivanov, Amanda Goodman, and Amanda J. Haes, ACS Nano, **2011**, 5, 4570-4580.

at ~5-10%.[156-158] While the influence of alkanethiol chain length, anchoring group, chemical composition, immersion time, and substrate topography was previously investigated for nanoparticles;[152,159-161] no evaluation of defect sites on solution-phase nanoparticles and implications thereof was performed.

In these studies, we will investigate how the ionic strength of the dielectric medium impacts the self-assembly of thioctic acid on the surface of gold nanoparticles. Specifically, an increase in NaCl concentration during alkanethiol incubation increases the packing density of thioctic acid SAMs on homogeneous gold nanoparticles by 17% while their stability increases by approximately the same magnitude vs. control studies. During SAM modification, the core size and optical properties of the gold nanoparticles will be shown to remain statistically unchanged as revealed by transmission electron microscopy (TEM) and extinction spectroscopy, respectively. In contrast, zeta potential and X-ray photoelectron spectroscopy (XPS) will reveal that the effective surface charge and sulfur to gold atomic ratio of functionalized gold nanoparticles, respectively, vary systematically then saturate as the estimated SAM packing density equilibrates. Estimations of the ionic strength dependent electrostatic interaction energy between carboxylic acid terminal groups in the SAM provide a rational explanation for these experimental observations. Significantly, nanoparticles functionalized in the presence of salt will be shown to be approximately twice as stable as nanoparticles prepared in the absence of salt. These data support that SAM packing density increases as a function of increasing NaCl concentration thereby suggesting that the density of pinhole and/or collapsed-site defects on nanoparticle surfaces are reduced. Better control in alkanethiol packing density as a result of a salt-mediated SAM assembly on gold nanoparticles will be fundamental in achieving reproducible gold nanoparticle covalent functionalization and their subsequent utility in applications and new technologies.

3.2 Experimental

3.2.1 Preparation of Citrate-Stabilized Au (Au@citrate) Nanoparticles

All glassware used in the preparation and storage of Au nanoparticles was cleaned with aqua regia (3:1 $HCl:HNO_3$), rinsed with water, and oven dried. Gold nanoparticles were prepared according to previous reports.[162] Briefly, a 200 mL aqueous solution of 1 mM $HAuCl_4$ was refluxed while stirring vigorously. Next, 20 mL of 38.8 mM citrate was quickly added, refluxed for 10 minutes, and allowed to cool to room temperature while stirring. The resulting gold nanoparticles had a diameter of $11.6_9 \pm 0.9_8$ nm as determined by TEM and an extinction maximum, $\lambda_{max} = 518$ nm.

3.2.2 Preparation of thioctic acid functionalized Au (Au@TA) Nanoparticles

Au@TA nanoparticles were prepared by modifying a previously published method.[163] First, Au@citrate nanoparticles were filtered (0.45 μm filter) (Whatman, Middlesex, UK) and centrifuged (Eppendorf – Model centrifuge 5424, Germany; 11,500 RPM (8,797 x g) for 40 minutes) to remove large aggregates and excess citrate, respectively. The resulting pellet was suspended in pH adjusted water (pH = 11 with 1 M NaOH) to a nanoparticle concentration of 10 nM according to the method described by Haiss.[164] Thioctic acid functionalization was carried out by adding 10 mM thioctic acid (100 μL in ethanol) to 10 mL aliquots of 10 nM Au@citrate nanoparticles. This solution was allowed to stir in the dark for at least 16 hrs at 20°C.

During the slow addition of salt,[165] a 2 M NaCl solution was added drop-wise to Au@TA nanoparticles until the salt concentration of salt reached 3.6 mM. This solution was allowed to stir (slowly) for 8 hours. The NaCl concentration was then increased to 7.2 and 14.4 mM in similar subsequent steps. After each of these incubation periods, excess thioctic acid and NaCl were removed by centrifugation at 11,500 RPM (8,797 x g)

for 40 minutes. In order to investigate the effect of time on the samples incubated in the presence of 16 mM NaCl, the samples were allowed to equilibrate for an additional 32 hours. Prior to measurements, these samples were centrifuged at 11,500 RPM (8,797 x g) for 40 minutes. Following removal of the supernatant, the nanoparticle pellet was resuspended in pH adjusted water (pH = 11). This rinsing process was repeated three times. Samples in which no salt was added but allowed to incubate in thioctic acid solutions were used as a control.

3.2.3 Transmission Electron Microscopy (TEM)

The homogeneity and diameter of the nanoparticles were characterized using TEM (JEOL JEM-1230). Samples were prepared by applying 30 μL of a diluted nanoparticle solution (50% mixture in ethanol) to a carbon Formvar coated copper grid (400 mesh, Electron Microscopy Sciences, Hatfield, PA). Excess solution was removed with filter paper, and the sample was allowed to dry. The resulting images were analyzed using Image Pro Analyzer, and at least 100 nanoparticles were evaluated per sample.

3.2.4 NMR Spectroscopy

^{1}H NMR and 2D COSY spectra were recorded on a Bruker 600 mHz spectrometer (Bruker Biospin Corp., Billerica, MA). Samples were prepared by centrifugation at 15,000 RPM (14,967 x g) for 30 minutes. After the supernatant was removed, the nanoparticles were resuspended in pH adjusted water (pH = 11) (repeated three times). Next, the samples were transferred to a lyophilizing vessel, flash frozen with liquid N_2, lyophilized to remove water, and resuspended in D_2O to a 50 nM nanoparticle concentration. Spectra were analyzed using Topspin and Nuts. Chemical shifts were referenced to the residual shifts of the deuterated solvent. 2D COSY spectra were acquired using standard pulse sequences optimized to the individual parameters of each sample. These data were used for proton assignments in the 1D spectra.

3.2.5 Extinction Spectroscopy

Extinction spectra of Au@TA nanoparticles were acquired using a UV-visible spectrometer (Ocean Optics HR 4000) configured in transmission geometry. Before acquiring spectra, samples were centrifuged at 11,500 RPM (8,797 x g) for 40 minutes and redispersed in 20 mM sodium borate buffer (pH = 9). The solution was diluted to a final nanoparticle concentration of 2 nM using the same buffer. All spectra were collected in disposable methacrylate cuvettes (path length = 0.5 cm) using the following parameters: integration time = 20 msec, average = 20 scans, and boxcar = 10.

3.2.6 Zeta Potential Measurements

Effective gold nanoparticle surface charges (zeta potential) were determined from their electrophoretic mobility at 25°C using a Malvern Zetasizer (Worcestershire, UK). Au@TA nanoparticle samples were centrifuged at 11,500 RPM (8,797 x g) for 40 minutes, redispersed in 20 mM sodium borate buffer (pH = 9), and diluted to a final concentration of 2 nM. Monomodal acquisitions and fits according to the Smoluchowski theory were used. Measurements were performed in triplicate, and error bars represent the standard deviation of these data.

3.2.7 X-Ray Photoelectron Spectroscopy (XPS)

XPS measurements were collected using a Kratos Axis Ultra Spectrometer with a monochromatic Al K_α X-ray source as described previously.[166] Briefly, a 160 eV pass energy, 1 eV step size, 200 ms dwell time, and ~700 μm x 300 μm X-ray spot size were used for a survey scan (range = 1200 – -5 eV). Region scans (O 1s, C 1s, S 2p, and Au 4f) exhibited typical band widths of 20 - 50 eV, 20 eV pass energies, 0.1 eV step sizes, and 1 sec dwell times. All spectra were analyzed using CasaXPS and were charge-calibrated with respect to the adventitious C 1s peak at 285.0 eV. The S 2p peak of thioctic acid was peak fitted using the S 2p doublet with a 2:1 area ratio and an energy difference of 1.2 eV. A Shirley background was used to subtract the inelastic background

from the S 2p and Au 4f signal. The curves were fit using a Gaussian/Lorentzian (GL(30)) lineshape. To account for differences in nanoparticle concentration in sample spots, the S 2p areas were normalized using the Au 4f area. Two areas were analyzed per sample. Error bars represent the standard deviation of these data.

3.2.8 Nanoparticle Flocculation Measurements

Au@TA nanoparticle solutions (10 nM) were prepared in pH 11 water. To monitor flocculation, gold nanoparticles were incubated for 72 hours in the absence and presence of salt, centrifuged, and redispersed to 3.0 mS cm^{-1} sodium acetate and phosphate buffer (pH 5.5 and pH 12, respectively). The solution was stirred, and extinction spectra were collected every 2 seconds. The data were baseline subtracted using an in-house written MatLab program. Briefly, LSPR spectra collected in pH 12 buffer were aligned to 0 AU at 800 nm and subsequently used to determine a normalization factor that was applied to all other spectra. Integrated areas were calculated from these normalized spectra (from 575 – 800 nm) collected in pH 5.5 buffer and plotted as a function of time.

3.3 Results and Discussion

3.3.1. Structural Characterization of Thioctic Acid Funtionalized Au Nanoparticles

Figure 3.1 depicts the self-assembly of thioctic acid on gold (Au@TA) nanoparticles. After initially functionalizing these nanostructures with thioctic acid and allowing them to incubate for 16 hours, NaCl is added incrementally in 8 hour incubation steps to promote thioctic acid self-assembly. Au@TA nanoparticles remain stable up to 14 mM salt concentrations. Above this concentration, Au@TA nanoparticles begin to aggregate as indicated by the growth of a characteristic low energy (~620 nm) extinction band (data not shown). Because each salt containing gold nanoparticle aliquot was

allowed to incubate for 8 hours, time control assays (i.e. equal incubation times in the absence of salt) are included. Structural analysis of these nanostructures via TEM reveals that average nanoparticle size does not change significantly throughout the SAM formation process as both (1) incubation time increases and (2) with the addition of salt (Figure 3.2). A representative TEM image of Au@TA nanostructures is shown in Figure 3.1B. As expected, Au@TA nanoparticles are spherical and exhibit a mean diameter of $11.6_1 \pm 0.9_8$ nm.

Noble metal nanoparticles (i.e. copper, gold, silver, etc.) exhibit strong extinction properties in the visible region of the electromagnetic spectrum[167-174] which are sensitive to changes in nanoparticle shape, size, stability, and local dielectric constant (i.e. the surrounding medium and/or surface modifications).[63,64] Localized surface plasmon resonance (LSPR) spectra arise when the incident photon frequency is in resonance with the collective oscillation of the conduction electrons in the nanoparticles.[66] Figure 3.1D shows the LSPR spectra of citrate stabilized gold (Au@citrate) (0 hours) and Au@TA nanoparticles after being functionalized in thioctic acid at varying salt concentrations. To ensure that bulk refractive index changes are not impacting these sensitive optical properties, the nanoparticles were washed and redispersed in 20 mM borate buffer (pH 9) prior to each measurement. The gold nanoparticles exhibit an extinction maximum (λ_{max}) at ~518 prior to functionalization. After exchange with thioctic acid, the λ_{max} shifts to ~521 nm. This value does not change significantly with increased incubation time and is indicative of stable, electromagnetically isolated nanostructures. Because thioctic acid chemisorbs to the surface of gold nanoparticles, the observed optical properties are consistent with an increase in local refractive index upon thioctic acid conjugation.

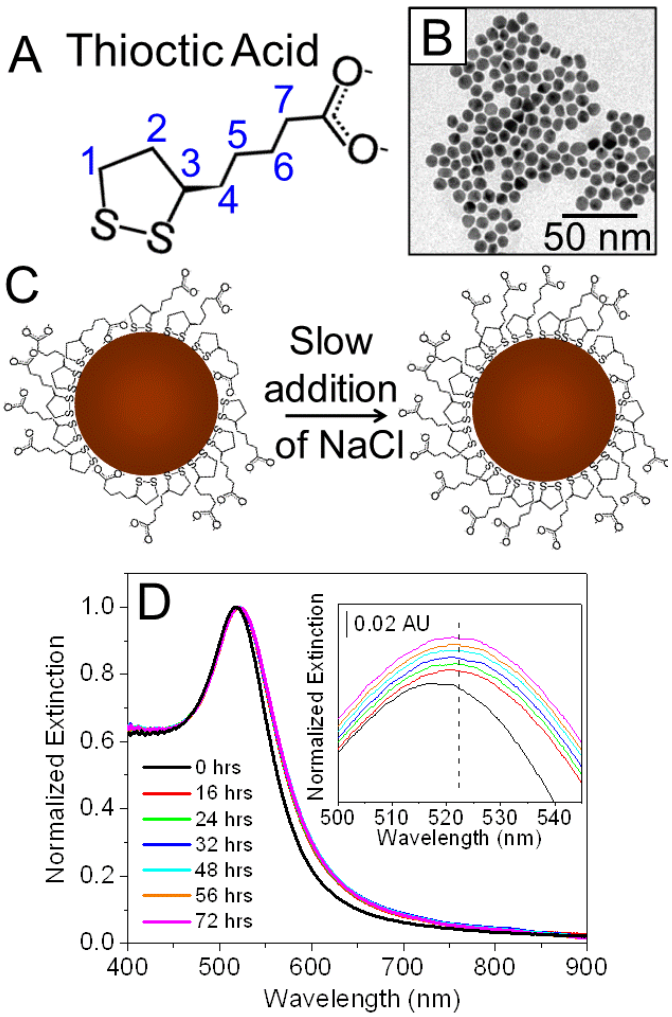

Figure 3.1. Slow addition of NaCl to Au@TA nanoparticles. (A) Structure and proton assignments used for thioctic acid. (B) Representative TEM image of Au@TA nanoparticles (average diameter, $d = 11.6_1 \pm 0.9_8$, N = 311). (C) Schematic of the proposed mechanism for thioctic acid packing with the slow addition of NaCl. (D) Extinction spectra of Au@TA nanoparticles equilibrated for 0 - 72 hours. The inset shows an enlarged view of the extinction maxima (λ_{max} = 518 nm and ~521 nm for 0 and 16 – 72 hours, respectively) in 20 mM sodium borate buffer (pH = 9).

3.3.2 Surface Charge Characterization of Au@TA Nanoparticles

To verify that salt concentration is influencing the surface coverage of thioctic acid on the Au nanoparticle surfaces, zeta potential measurements (in mV) were carried

out as a function of time both in the presence and absence of salt. Figure 3.3 summarizes these average (effective) surface charge data. For clarity, both control (no NaCl) and salt (with NaCl) data are plotted versus time (i.e. the incubation time for gold nanoparticles in the thioctic acid solutions). It should be noted that the surface pK_a for carboxylic acid terminated SAMs differ from solution values ranging from 4.5 - 7.[163,175-177] For all Au@TA nanoparticle samples studied, the surface potentials exhibit a negative value at pH = 9 which arise from the deprotonation of terminal carboxyl acid groups of thioctic acid molecules bound to the nanostructures.

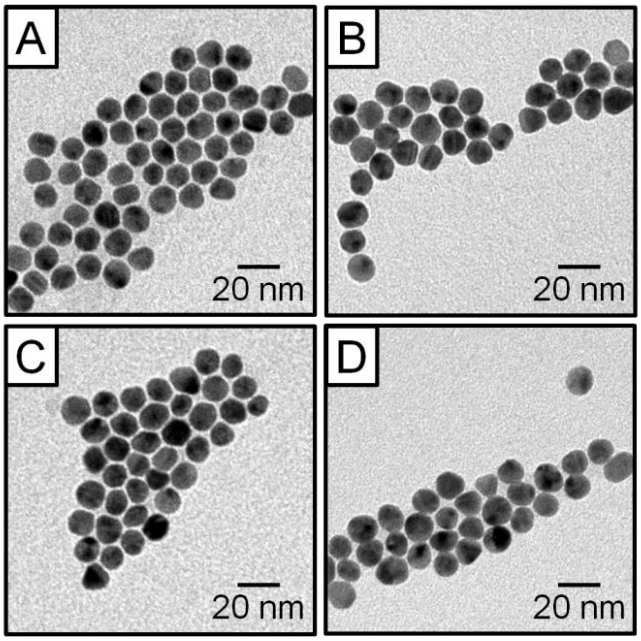

Figure 3.2. Representative TEM images of Au@TA nanoparticles incubated for (A) 16 (no NaCl) (B) 56 (no NaCl) (C) 56 (16 mM NaCl) and (D) 72 (16 mM NaCl) hours exhibited mean diameters $11.6_9 \pm 0.9_8$, $12.0_6 \pm 0.8_1$, $11.6_1 \pm 0.9_8$, and $12.0_0 \pm 0.8_6$ nm, respectively.

Previous studies revealed that carboxylic acid functionalized gold nanoparticles exhibited negative zeta potential values that ranged from 36 – 60 mV (pH 9).[163,178,179] As

shown in Figure 3.3, the zeta potential of Au@TA nanoparticles are dependent on both time and salt addition. In the absence of NaCl, the zeta potential magnitude ranges from -23.9 to -30.1 mV, a change of 6.2 mV, as incubation time increases. Similar trends are observed for Au@TA nanoparticles prepared in the presence of NaCl; however, the surface potentials range from -23.9 to -33.8 mV, a change of 9.9 mV, a change that is 60% greater than when salt is not present during ligand exchange.

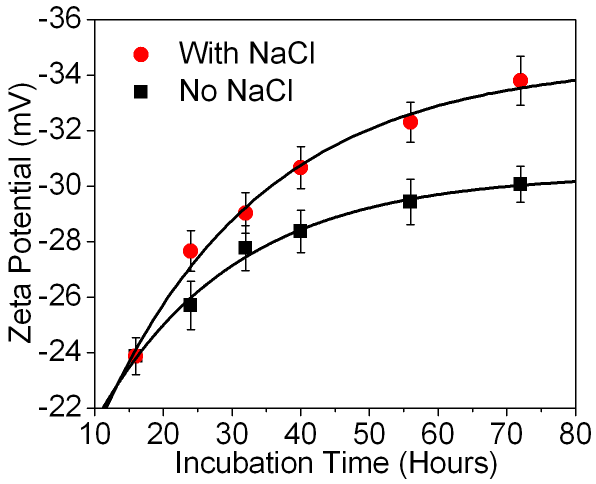

Figure 3.3. Zeta potential measurements for 2 nM Au@TA nanoparticles prepared in the presence and absence of NaCl. Nanoparticles were rinsed and suspended in 20 mM sodium borate buffer (pH = 9) prior to each measurement. The solid lines represent exponential fits for the zeta potential vs. incubation time data: "No NaCl" $y = -14.7_5e^{-x/20.0} - 30.4_3$ and "With NaCl" $y = -20.5_2e^{-x/23.5} - 34.5_0$.

To further investigate the differences between ligand exchange reactions in the absence and presence of salt, the zeta potential curves are fitted with an exponential fit. From this fit, a (theoretical) saturated zeta potential is calculated at -30.4 and -34.5 mV for Au@TA nanoparticles incubated in the absence and presence of NaCl, respectively. Although the zeta potential magnitude increases with increasing incubation time, the addition of NaCl during thioctic acid functionalization produces a greater zeta potential magnitude increase (vs. controls). These surface charge differences support that

molecular surface coverage (i.e. thioctic acid packing density) increases on gold nanoparticles when salt is present during functionalization versus control studies.

3.3.3 ^{1}H NMR of Au@TA Nanoparticles

Recently, ^{13}C and ^{1}H NMR were applied to characterize molecules adsorbed to the surface of nanomaterials.[180] Four significant spectral characteristics are generally observed: (1) peak broadening,[181] (2) free ligand signatures superimposed on the surface-bound ligand spectrum,[182] (3) chemical shift differences between free ligand and surface-bound ligands,[182] and (4) magnetic field variations for the ligand which depend on the distance of the proton from the nanomaterial surface,[183] as well as with nanoparticle composition and size.[184,185] _ENREF_184 Similar observations are made for Au@TA nanoparticles. 2D COSY studies (Figure 3.4A) were performed to determine the proton assignments shown in Figure 3.1A. In comparison to free ligand studies, spectral features for thioctic acid are significantly broadened when bound to gold nanoparticles (Figure 3.4B) thereby verifying the molecules sampled are chemisorbed to the nanoparticle surface and not free in solution. This is an important spectral observation given that no superimposed bands are observed in these spectra.

Table 3.1. ^{1}H NMR Chemical Shifts, δ in ppm, for Thioctic Acid Free in Solution and bound to Au Nanoparticles

Proton Assignment	**Free Ligand (ppm)**	**Nanoparticle Bound (ppm)**	**Chemical Shift Difference (δ ppm)**
7	2.05	2.05	0.00
6	1.50	1.45	0.05
5	1.38	0.80	0.58
4	1.60, 1.70	1.10	0.50, 0.60
3	3.65	Not observed	-
2	1.90, 2.40	1.70, 2.10	0.20, 0.30
1	3.15	Not observed	-

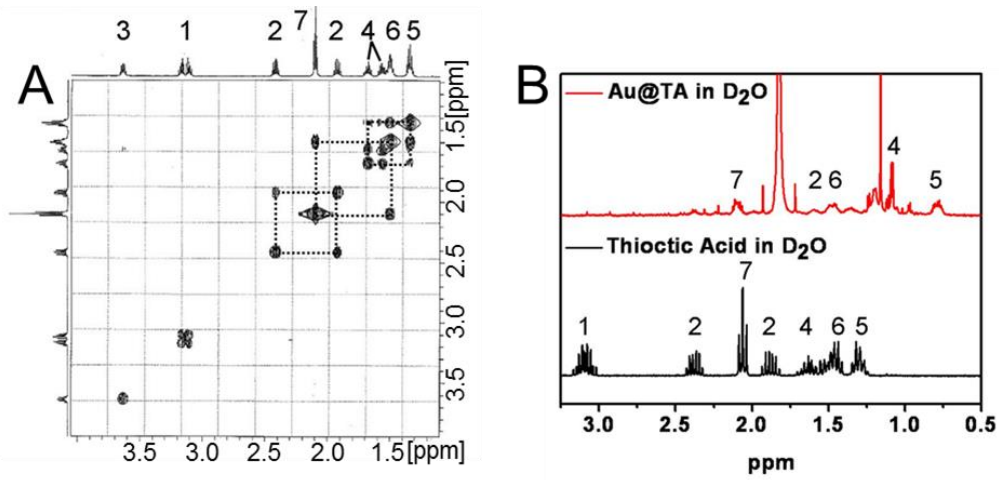

Figure 3.4. ^{1}H NMR characterization of (A) 2D COSY ^{1}H NMR spectra of 10 mM thioctic acid dissolved in D_2O.(B) ^{1}H NMR spectra of 10 mM thioctic acid and 50 nM Au@TA nanoparticles in D_2O. The numbers represent proton assignments for thioctic acid.

Table 1 summaries the average chemical shift data for thioctic acid free in solution (no nanoparticles) and bound to nanoparticle surfaces. At least four spectral features are notable. First, the methylene protons on carbons 7 and 6 exhibit no significant chemical shift differences between free and surface bound ligands. This suggests that these protons are farthest from the nanoparticle surface and thereby possess the highest degree of entropy or solution-like behavior relative to the other protons.[186,187] Second, a greater degree of up-field chemical shift difference is observed for the methylene protons on carbons 5 and 4. As discussed previously, chemical shift differences between free and nanoparticle bound NMR signatures increase as the distance from the nanoparticle surface decreases.[183] Following this reasoning, the degree of up-field shift differences for a given proton can be used to gauge its average distance from the nanoparticle surface relative to other protons. Finally, although the protons on carbon 2 are detectable, the protons on carbons 3 and 1 are not observed because of significant signal broadening which leads to minimization of the signal to noise ratio of these peaks.

As expected, these data suggest thioctic acid is attached to the surface of the gold nanoparticle via the dithiol ring with the carboxylic acid extending out into solution.

3.3.4 X-ray Photoelectron Spectroscopy of Au@TA Nanoparticles

Both LSPR and zeta potential data indicate that the slow addition of salt increases the packing density of thioctic acid on the gold nanoparticle surface. To verify this, quantitative information regarding the efficiency of thiol immobilization and the nature of thiol-gold interactions are probed using X-ray photoelectron spectroscopy (XPS). Previously, thioctic acid functionalized gold thin film analysis revealed that the S 2p region exhibited a doublet with a 1.2 eV splitting energy centered at ~162 and 163.2 eV for molecules directly bound to the gold surface.[99,134,188-191] As shown in Figure 3.5A, Au@TA nanoparticles that are rinsed once exhibit S 2p photoelectron spectral features consistent with bound and unbound thioctic acid molecules. Repeated rinsing, however, leads to the disappearance of the high binding energy (BE) S 2p bands associated with unbound thioctic acid.[192] Figure 3.5B reveals XPS spectra of Au@TA nanoparticles prepared in the absence and presence of salt after sufficient rinsing. In these data, a single S 2p doublet (centered at ~162.5 eV) is observed. While the S 2p photoelectron spectra exhibit weak signal strengths because of the sub-monolayer to monolayer thioctic acid surface coverage on the nanoparticle surfaces, these findings indicate that the majority of the signal is attributed to surface bound thioctic acid molecules.

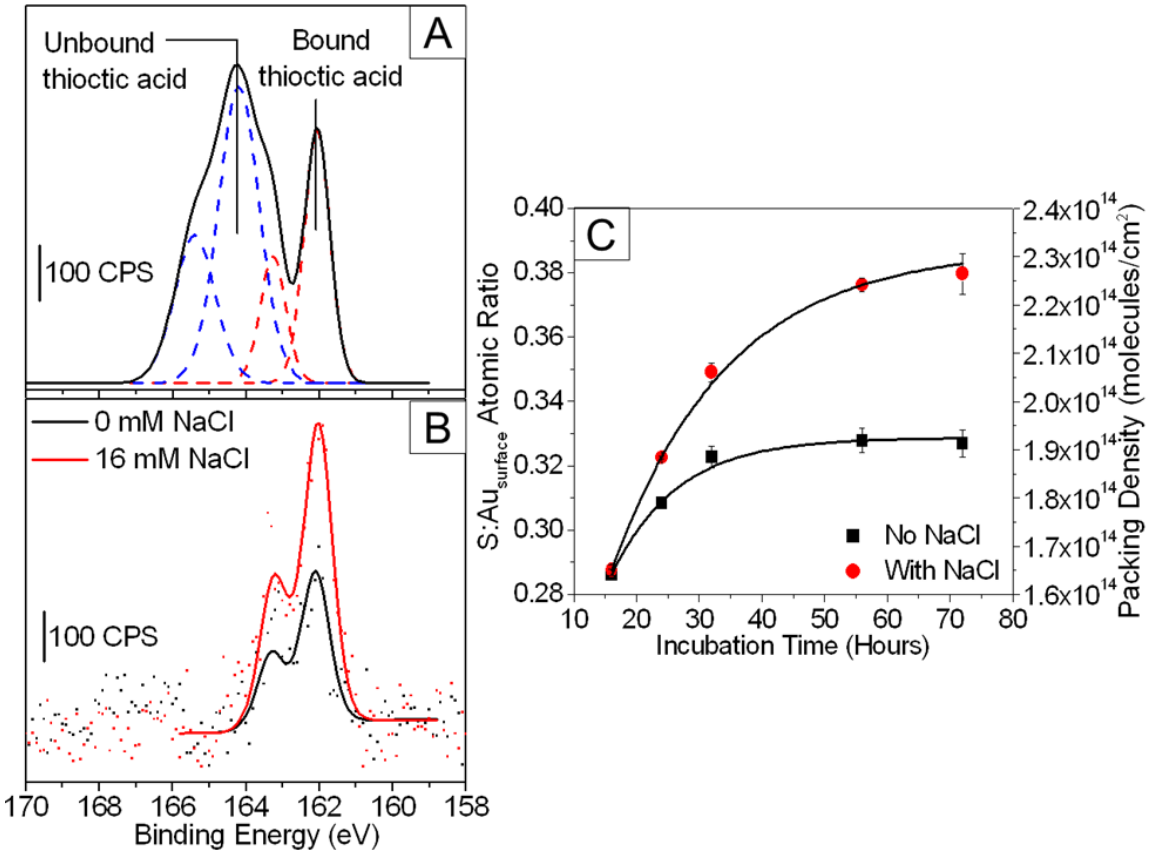

Figure 3.5. XPS characterization of Au@TA nanoparticles. (A) Normalized XPS spectra (S 2p) of Au@TA nanoparticles after one rinsing cycle. A S 2p doublet is observed for thioctic acid (doublet BE = 162.0 and 163.2 eV). (B) Normalized XPS spectra of Au@TA nanoparticles prepared in 0 and 16 mM NaCl (equilibration time = 72 hours) where the solid lines and dots correspond to the fitted and raw data, respectively. (C) Comparison of the $S:Au_{surface}$ atomic ratio (right-hand y-axis) and packing density (left-hand y axis) vs. incubation time for Au@TA nanoparticles prepared in the presence and absence of NaCl. The solid lines represent exponential fits for the $S:Au_{surface}$ atomic ratio vs. incubation time: "No NaCl" $y = -0.19_8e^{-x/10.4} + 0.32_9$ and "With NaCl" $y = -0.24_0e^{-x/18.4} + 0.38_8$.

To evaluate how incubation time and/or salt concentration impacts thioctic acid surface coverage, the S 2p doublet signal strength was monitored. Figure 3.5B compares S 2p spectra for Au@TA nanoparticles prepared after the addition of a 0 and 16 mM NaCl upon incubation for 72 hours. Signal correction of the S 2p peak are to the gold 4f peak area removed any interference caused by evaluating slightly different nanoparticle

concentrations and samples. These data reveal that the addition of NaCl during thioctic acid functionalization increases the normalized S 2p peak are versus conditions when no salt is added. Moreover, the C 1s peak area and the O 1s area did not show any trends as a result of organic species contamination as the samples were prepared in ambient conditions (Figure 3.6).[193]

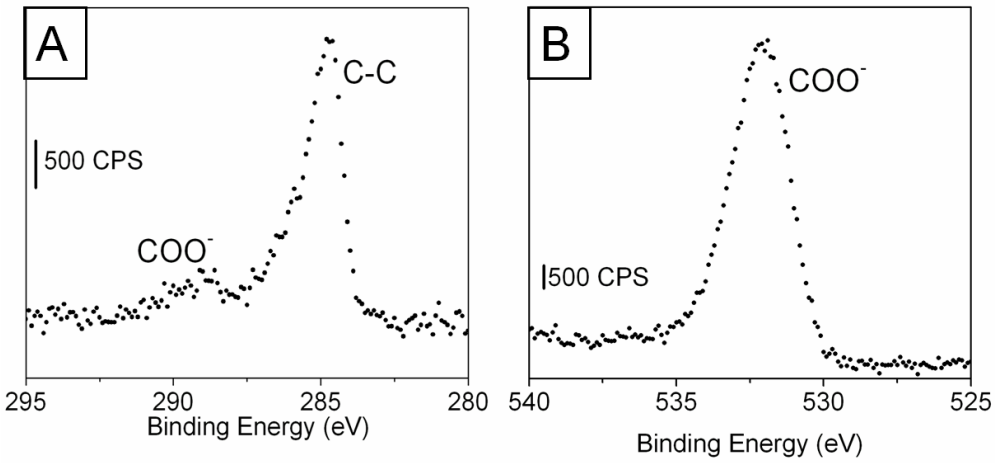

Figure 3.6. Representative normalized XPS spectral regions for (A) C 1s (BE = 284.4 and 289 eV) and (B) O 1s (BE = 531.9 eV) regions of Au@TA nanoparticles.

To quantitate the XPS data, the S 2p and Au 4f peak areas were converted to a S:Au atomic ratio using the empirical atomic sensitivity factor (SF) for each element (SF = 0.54 and 4.95 for S 2p and Au 4f, respectively).[194] Furthermore, because XPS interrogates a fraction of the total atomic layers, the Au XPS area must be corrected for the electron escape depth as follows:

$$\text{escape depth} = \lambda\cos(\theta) \quad (1)$$

where λ is the inelastic mean free path (IMFP) and θ is the angle between the surface normal and the direction of the emitted electron.[193,194] For these experiments θ is 0 and λ

is $1.78 \pm 0.00_2$ nm where the IMFP is determined using the NIST Electron Inelastic Mean Free Path Database and the average kinetic energy of the Au 4f peaks.[195-197]

To apply this to a nanoparticle, the shell method must first be used to calculate the total number of atomic layers in a nanoparticle.[131,198] 198,199 The shell method models a nanoparticle as a central atom which is surrounded by n shells (i.e. layers) of gold atoms where the number of gold atoms in the n^{th} shell can be calculated using the equation $10n^2+2$.[131,198] _ENREF_198 Next, the total number of shells per nanoparticle is calculated by dividing the nanoparticle radius ($r=d_{NP}/2$) by the gold atom diameter (d_{Au} = 2.882Å) (Figure 3.7A). Dividing the escape depth by the diameter of a gold atom will yield the number of atomic layers signaled (N_{layer}) as follows:

$$N_{layers} = \frac{\lambda}{r_{Au}} = 6._2 \text{ layers} \qquad (2)$$

where the number of layers is rounded to the closest whole number of shells in subsequent calculations.

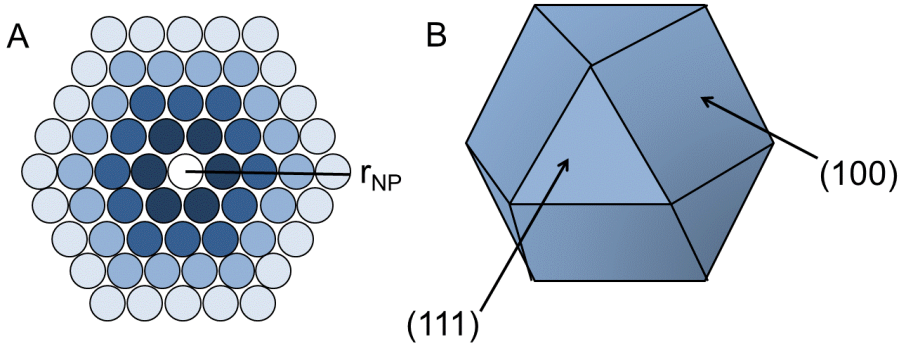

Figure 3.7. Schematic representation of a (A) gold nanoparticle cross section which reveals concentric shells of gold atoms surrounding a central atom, and (B) Au atom Miller indices on the nanoparticle surface.

Using these equations, a gold nanoparticle (d = 11.6 nm) contains 20 shells total but ~6 are sampled in these XPS conditions. The shell method can be applied to correct the S to Au atomic ratio ($S/Au_{surface}$) using the following equation:

$$\frac{S}{Au_{surface}} = \left[\frac{\sum_{n=15}^{20}(10n^2+2)}{(10n^2+2)}\right]\left[\frac{S}{Au}\right] \quad (3)$$

where the numerator in the first set of brackets is the number of total gold atoms signaled (n = 15 to 20) and the denominator is the number of surface gold atoms (n = 20). In the second set of brackets, S/Au represents the (sensitivity factor) corrected XPS signal. In order to distinguish if increased thioctic acid SAM packing density arises from the systematic addition of NaCl, or from increased incubation time with thioctic acid, the $S/Au_{surface}$ atomic ratio for gold nanoparticles incubated with thioctic acid in the absence and presence of NaCl are compared (Figure 3.5C). In both ligand exchange environments, the $S/Au_{surface}$ atomic ratio increases systematically with increasing thioctic acid incubation times. Figure 3.5C clearly displays that the $S/Au_{surface}$ atomic ratio saturates after an incubation period of 72 hours. Additionally, while longer incubation times increase the number of thioctic acid molecules on the Au nanoparticle surfaces; salt mediates this process.[131,193-198] By applying an exponential fit to these data, a saturated $S/Au_{surface}$ atomic ratio of 0.32_9 and 0.38_8 is calculated for Au@TA nanoparticles incubated in absence and presence of NaCl, respectively. In the absence of NaCl, these values imply that at least three gold atoms interact with one sulfur atom. In comparison, this value decreases to ~2.5 gold atoms interacting with each sulfur atom for SAMs prepared in the presence of NaCl. While the difference between the $S/Au_{surface}$ atomic ratio is small, a significant difference in the number of molecules on nanoparticle surfaces are indicated.

Expanding on these data, the packing density of thioctic acid SAMs on gold nanoparticle surfaces can be estimated. It should be noted that (1) the core size of

Au@TA nanoparticles incubated in the absence and presence of NaCl do not change (Figure 3.2) and (2) the surface of ~12 nm gold nanoparticles contain predominately (100) surface planes (Figure 3.7B).[95,199] As a result, the packing density of atoms on the surface on the nanoparticle (σ_{hkl}) can be calculated as follows:

$$\sigma_{hkl} = \frac{4}{Qa^2(h^2+k^2+l^2)^{0.5}} \quad (4)$$

where Q is 2 for (100), and a is the bulk lattice parameter.

Next, the packing density of thioctic acid on Au@TA nanoparticle surfaces prepared in the absence and presence of salt can be approximated from XPS data as follows:

$$\text{packing density} = \left[\frac{S}{Au_{surface}}\right]\left[\frac{TA}{S}\right][\sigma_{100}] \quad (5)$$

where the corrected XPS signal (Equation 3), the thioctic acid to sulfur ratio (2 sulfur atoms per thioctic molecule), and the gold atom packing density for a (100) surface plane are found in the first, second, and third brackets, respectively. For Au@TA nanoparticles prepared in the absence of salt, surface coverage is ~1.72 x 10^{14} molecules/cm^2 after 16 hours of equilibration time and increases to 1.97 x 10^{14} molecules/cm^2 after equilibrating for 72 hours. With systematic NaCl additions, Au@TA nanoparticles equilibrated for 16 hours exhibit thioctic acid packing densities of 1.73 x 10^{14} molecules/cm^2 and increases to 2.29 x 10^{14} molecules/cm^2 after equilibrating for 72 hours. The packing density calculations demonstrate that the slow addition of salt increases thioctic acid SAM packing density by 17% relative to the absence of salt after a 72 hour incubation period. These values agree well with previously reported thioctic acid packing densities on flat gold surfaces which range from 1.8x10^{14} – 2.1x10^{14} molecules/cm^2,[176,200-207] indicating XPS is an excellent technique to calculate SAM packing density on gold nanoparticles.

3.3.5 Electrostatic Interaction Energy and TA Self-Assembly

The LSPR, XPS, and zeta potential measurements suggest that the slow addition of salt increases the chemisorption of thioctic acid on gold nanoparticle surfaces thereby resulting in an overall larger SAM surface coverage than when NaCl is omitted during ligand exchange reactions. We hypothesize that the mechanism of this effect is attributed to electrostatic interaction energy[208] differences (i.e. decreased energy) between adjacent carboxylic acid terminal groups in the SAM as salt concentration increases. To model this, bulk ionic strength is used to estimate relative permittivity (ε_s) as follows:[209,210]

$$\varepsilon_s = 78.45 - \delta_s C_s + bC_s^{1.5} \quad (6)$$

where δ_S is the permittivity decrement (15.8 $L \cdot mol^{-1}$ when NaCl is the electrolyte), C_S is the electrolyte concentration, and b is a constant with a value of 3.01 $L^{2/3} \cdot mol^{-3/2}$. Next, Bjerrum lengths[211] are calculated as follows: $l_b = e^2/(4\pi\varepsilon_s\varepsilon_r k_b T)$ where e is the elementary charge, ε_r is permittivity of free space, k_b is the Boltzman constant, and T is the temperature (294.3 K)). Additionally, inverse Debye lengths are calculated as follows: $\kappa = \sqrt{8\pi l_b I}$. Subsequently, Debye lengths (κ^{-1})212 are then calculated (Table 2) as a function of ionic strength (I). Finally, the electrostatic interfacial energy (E_{ij}^{EL}) between two charged (carboxylic acid) molecules (i and j) is computed as follows:[208]

$$E_{ij}^{EL} = \frac{Z_i Z_j e^2}{4\pi\varepsilon_s\varepsilon_r} \frac{e^{-\kappa(l_b-\sigma)}}{(1+\kappa\sigma)l_b} \quad (7)$$

where Z_i and Z_j are the charge numbers for two deprotonated carboxylic acid groups, σ is the Leonard Jones Fluid-Fluid potential for carboxyl groups (0.305 nm).[212]

As shown in Figure 3.8A, increasing the ionic strength of the solution increases inverse Debye lengths and subsequently, decreases the normalized electrostatic interfacial energy (E/E_o) between two adjacent molecules. This result is expected[208] as the effective spacing between two (i.e. l_b) and the effective Debye length of a charged molecule(s) should increase and decrease, respectively as ionic strength increases. This model

supports the hypothesis that the electrostatic interfacial energy between two molecules decreases as salt concentration increases.

Table 3.2. Calculated Debye Lengths as a Function of NaCl Concentration and Ionic Strength.

[NaCl] (mM)	I (mM)	κ^{-1} (nm)
0	1.2_6	8.5_1
3.6_3	4.8_8	4.3_2
7.2_5	8.5_0	3.2_7
14.4_4	15.6_9	2.4_1

To investigate how the electrostatic interfacial energy impacts SAM formation and packing density saturation on gold nanoparticles in the presence and absence of salt, the average spacing between TA molecules was estimated using XPS packing densities and Spartan. Importantly, the dimension of the carboxylic acid terminal group is estimated using the length between the oxygen atoms (2.23 Å) and the covalent radius of an oxygen atom (0.63 Å). Assuming a rectangular molecular footprint for the carboxylic acid group, the average spacing between TA molecules is calculated. Finally, the electrostatic interfacial energy is determined using equation 7 where l_b is the average distance between two SAM ligands.

As shown in Figure 3.8B, the electrostatic interfacial energy between SAM ligands increases with packing density when formed both in the presence and absence of salt. Dashed lines indicate saturated packing densities in the absence and presence of salt. Notably, this energy increases more rapidly and saturates at a lower packing density when the SAM forms in the absence of salt (ionic strength = $1._3$ mM) vs. the presence of salt. In the presence of salt the normalized electrostatic interfacial energy between surface bound ligands decreases by ~4% vs. the low ionic strength time control studies. We attribute this difference to shorter Debye lengths in the relatively higher ionic strength

ligand exchange conditions. Importantly, these interfacial energetic differences would facilitate the accessibility of pinhole defects in the SAM layer[213] allowing these sites to be more easily accessed and filled by additional thioctic acid molecules.

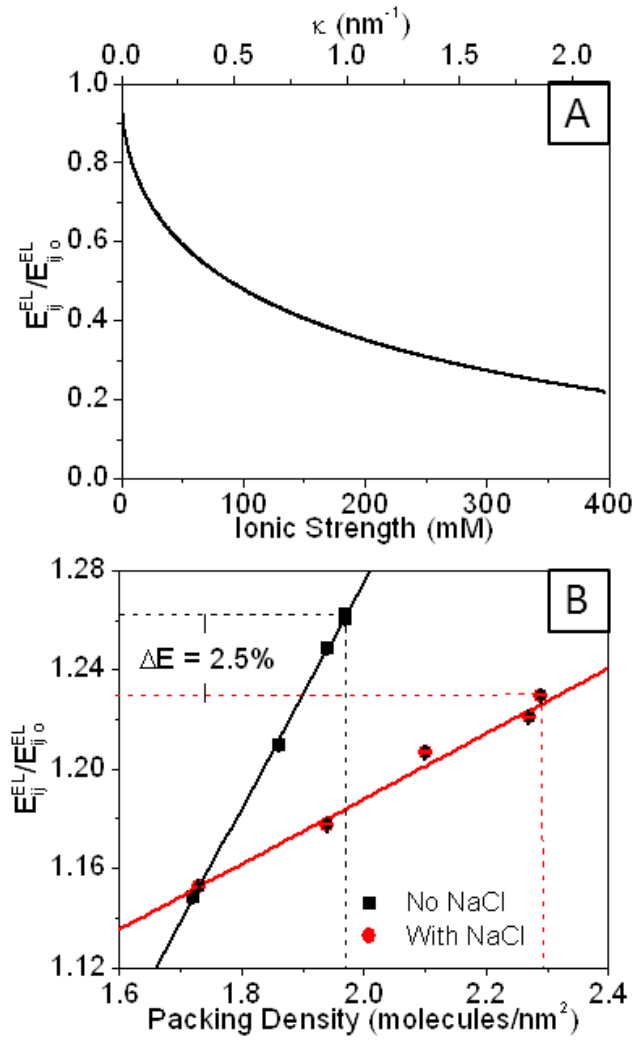

Figure 3.8. Calculated electrostatic interfacial energies between two terminal carboxylic acid groups. (A) Normalized electrostatic interfacial energy as a function of ionic strength (lower x axis) and inverse Debye length (upper x axis). (B) Normalized electrostatic interfacial energy as a function of thioctic acid packing density for exchange reactions that occurred in the absence and presence of salt. Dashed lines indicate the estimated packing density saturation values and corresponding normalized electrostatic interfacial energies. Error bars are contained within the size of the data points and represent propagated error.

3.3.6 Evaulation of Au@TA Nanoparticle Stability

To further investigate how SAM packing density impacts nanostructure stability, the flocculation parameter[67,99,100] for Au@TA nanoparticles incubated for 72 hours in the absence and presence of NaCl was evaluated. Flocculation parameter studies can be used to gain semi-quantitative information about the nanostructure stability by monitoring changes in extinction as a function of solution pH and/or time.[67,99,100] As nanoparticle flocculation increases, the extinction intensity at ~521 nm decreases while a new lower energy band at 650 nm intensifies (Figure 3.9). Next, the extinction spectra were integrated from 575 – 800 nm to quantify the degree of nanoparticle flocculation as a function of time (Figure 3.10). In pH 5.5 buffer, the integrated area increases as a function of time and at different rates for the two nanoparticle samples. To compare the stability of the Au@TA nanoparticles, the integrated data was used to determine when flocculation reached its maximum. Larger values are indicative of more stable nanostructures.[67] The Au@TA nanoparticles incubated without NaCl flocculated within 26 seconds whereas the Au@TA nanoparticles incubated in the presence of NaCl flocculated in twice the time. Significantly, these flocculation studies reveal that salt-mediated thioctic acid self-assembly increases the stability of the Au@TA nanoparticles by ~20% vs. controls.

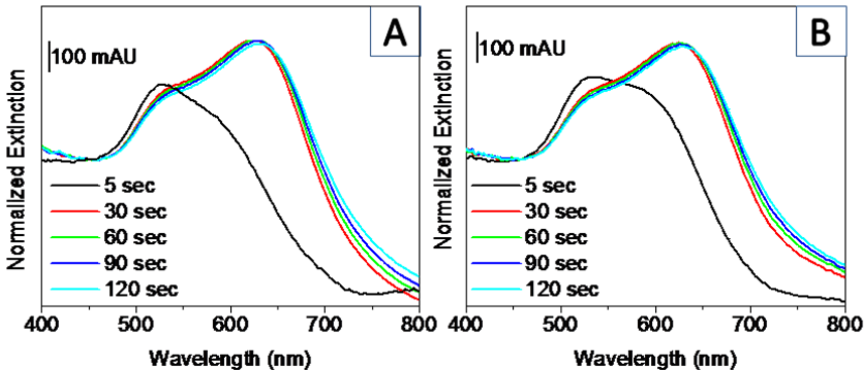

Figure 3.9. Normalized extinction spectra for Au@TA nanoparticles incubated for 72 hours in the (A) absence and (B) presence of 16 mM NaCl. Nanoparticles were centrifuged, dispersed in buffer (pH 5.5), and monitored while stirring as a function of time.

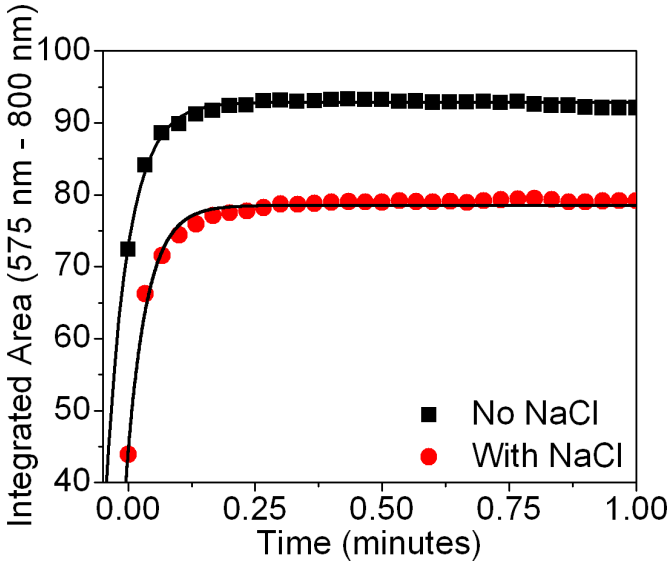

Figure 3.10. Normalized integrated area for Au@TA nanoparticles incubated for 72 hours in the presence and absence of salt. Extinction spectra of Au@TA nanoparticles in buffer (pH=5.5) were integrated from λ = 575-800 nm to semi-quantify flocculation.

3.4 Conclusions

In summary, gold nanoparticles functionalized with thioctic acid were prepared with the slow addition of NaCl. TEM, ^{1}H NMR, extinction spectroscopy, zeta potential, XPS, and flocculation studies determined that the self-assembly of thioctic acid on gold nanoparticles increases with increasing NaCl concentration. Quantitative information regarding the fraction of pinhole and collapsed defect sites on gold nanoparticles was not evaluated; however, salt facilitated the self-assembly process. First, an increase in NaCl decreases the Debye length and area occupied by deprotonated carboxylate groups on the assembled thioctic acid molecules thereby reducing the electrostatic interfacial energy between adjacent molecules and as a result, facilitating increased SAM packing densities. Furthermore, the slow addition of NaCl to gold nanoparticles during thioctic acid self-assembly increased subsequent functionalized nanoparticle stability vs. controls as determined from flocculation studies. We expect these results to improve strategies for reproducible SAM formation on solution-phase nanostructures. Future studies could be expanded to investigate how nanoparticle shape, size, and radius of curvature impact this self assembly process for ultimate improvements in the reproducible synthesis and use of nanomaterials in a variety of applications.

CHAPTER 4 DIRECT NORMAL RAMAN DETECTION OF DRUGS USING MOLECULAR IMPRINTED POLYMERS

4.1 Introduction

Recently, molecular imprinted polymers (MIPs),[28,32,214] which can exhibit affinities and selectivities comparable to antigen-antibody couples[28-32] were developed and incorporated into biosensors to provide specific recognition sites for target molecules including drugs, explosives, enzymes, hormones, and sterols.[28,33-37] The most successful non-covalent imprint approaches for MIP synthesis and subsequent detection applications includes the functional monomer methacrylic acid (MAA) and the cross-linker ethylene glycol dimethacrylate (EGDMA). MAA which contains a carboxylic acid group that serves as a hydrogen-bond donor as well as a hydrogen bond-acceptor,[215] interacts non-covalently through multiple hydrogen bonds with target molecules thereby forming selective recognition sites.[68]

Ideally, when a template molecule is removed from a MIP, cavities that are shape and size specific for the templated molecule remain as nanocavities in the MIP.[28,69] Using the methacrylate polymer system, recognition efficiency was demonstrated to be 13 times greater than with non-imprinted polymers for cholesterol;[69] however, introduction of binding site heterogeneity during synthesis, template removal, and grinding; resulted in lower affinities for target molecules.[214] This heterogeneity is often amplified because MIPs are grounded and sieved to improve particle size uniformity. Furthermore, the grinding process often produces an additional degree of heterogeneity by increasing the distribution of surface and interior recognition sites.[47] As a result, the template sites exhibit a range of affinities for the target drug molecules which can lead to an increase in non-specific binding interactions.

Previous studies utilized infrared spectroscopy and other techniques to indirectly detect target molecules using MIPs.[35,36,42] While these methods yielded large signals, the

observed spectral signatures are often broad and difficult to measure in aqueous environments.[216] To combat these inherent spectroscopic limitations for small molecule detection, Raman spectroscopy can be used. Despite the inherently weak S/N associated with this methodology, employment of Raman spectroscopy allows for the direct monitoring of target species in complex samples through their narrow and unique narrow vibrational bands[11-14,16] As such, the identification and quantification of analytes in MIPs using unique vibrational bands assignment is possible. Furthermore, the dependence of these unique vibrational features to the chemical environment[217] could facilitate identifying molecules in solution or bound to MIP recognition sites. Importantly, monitoring unique Raman bands of target species plus those associated with the MIP would also provide an internal standard signal response which allow for molecular recognition even in the presence of nonspecific binding.

Herein, perm-selective MIPs are synthesized, characterized, and used to identify and quantify acetaminophen, aspirin, or caffeine in a complex sample. The viability of using Raman spectroscopy to quantitatively and directly detect these over-the-counter drugs using templated methacrylate-based polymers is investigated. Unique Raman bands for caffeine, acetaminophen, aspirin, and non-imprinted polymer are identified. Environmental-dependent shifts in these unique Raman vibrational bands are used to identify drug molecules bound to the MIP or free in solution. Next, size analysis of MIP particles is performed using transmission electron microscopy (TEM) and dynamic light scattering (DLS) for dried and hydrated MIP particles, respectively. Numerical analyses based on a standard binding model are applied for each drug-MIP couple using Raman intensities of the unique vibrational bands as a function of known drug concentration that are relative to an internal standard. The binding capacity, drug binding site density in the MIPs, and equilibrium binding constant (K_{eq}) of each drug-MIP complex are estimated. Importantly, these results are used to analyze drug mixtures in complex samples including in an over-the-counter migraine medication. While MIP recognition capabilities

provide modest selectivity, Raman microscopy successfully overcomes this recognition limitation by facilitating quantitative and qualitative detection of the three molecules. Finally, response times for drug binding decrease to less than 30 minutes when MIPs are packed in flow-through devices. This approach dramatically decreases the amount of MIP required per assay through sample reusability while also allowing for shorter analysis times vs. steady state measurements. All in all, the combination of modest MIP selectivity and the environmentally sensitive vibrational band frequencies associated with Raman spectroscopy is expected to facilitate new methods for complex biological and chemical analysis.

4.2 Experimental Methods

4.2.1 Materials

Acetonitrile (C_2H_3N), 2-acrylamideo-2-methyl-1-propanesulfonic acid ($C_7H_{13}NSO_4$), acetaminophen ($C_8H_9O_2N$), aspirin ($C_{11}H_{11}O_6$), azobisisobutylonitrile (AIBN), caffeine ($C_8H_{10}N_4O_2$), ethyl acetate ($C_3H_8O_2$), ethylene glycol dimethacrylate ($C_{10}H_{14}O_4$), glycidyl methacrylate ($C_7H_{10}O_3$), 1-hydroxy-cyclohexyl-phenyl-ketone (Irgacure 184), 4-(2-hydroxyethyl)-1-piperazineethanesulfonic acid (HEPES), tetrahydrofuran (THF) (C_4H_8O), toluene (C_7H_8), and 3-trimethoxysilylpropyl acrylate ($C_8O_8H_{12}Si$) were purchased from Sigma-Aldrich (St. Louis, MO). An over-the-counter migraine medication was purchased from a local discount store. All other chemicals were purchased from Fisher Scientific (Pittsburgh, PA). Chemicals were used as received unless otherwise stated. Water (18.2 MΩ cm^{-1}) was obtained using a Nanopure System from Barnstead (Dubuque, IA).

4.2.2 Molecular Imprinted Polymer (MIP) Synthesis

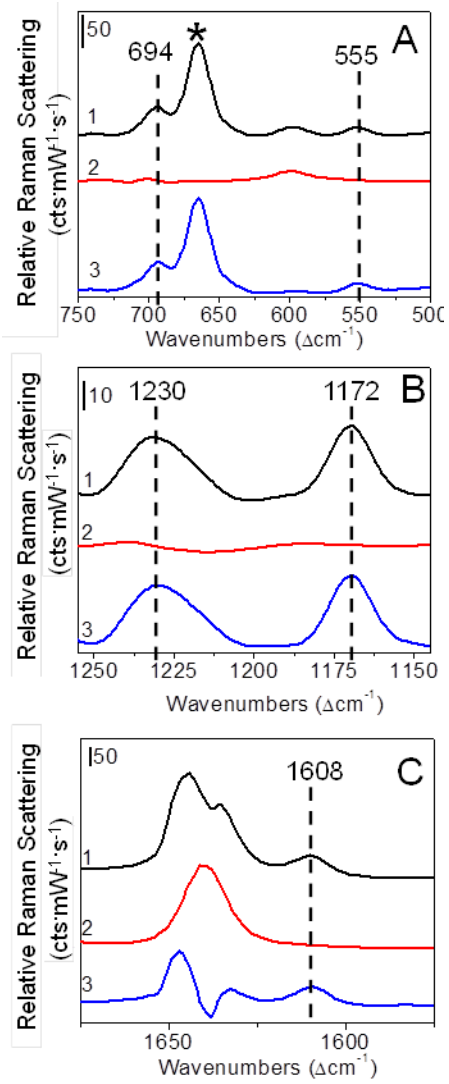

Figure 4.1. Representative relative Raman spectra for (A) caffeine, (B) acetaminophen, and (C) aspirin molecular imprinted polymers (1) before and (2) after template removal. (3) Representative Raman difference plots were generated by subtracting spectrum (2) from spectrum (1). The Raman spectra are relative to the polymer C-C-O stretch at 600 cm^{-1}. The unique vibrational modes are labeled for aspirin (1608 cm^{-1}, C=C ring stretch), acetaminophen (1230 cm^{-1}, phenyl rocking and 1172 cm^{-1}, phenyl bending), and caffeine (694 cm^{-1}, O=C-N deformation and 555 cm^{-1}, C-N-CH_3 deformation). Peaks denoted with an asterisk correspond to DMSO. Raman parameters: λ_{ex} = 532 nm, (A) t_{int} = (1) 5 s, (2) 4 s, P = 40 mW; (B) t_{int} = (1) 14 s, (2) 13 s, P = (1) 24.9 mW, (2) 26.7 mW; (C) t_{int} = (1) 2s, (2) 2.5 s, P = 24 mW.

MIPs were prepared according to previous reports.[34,218] Briefly, caffeine imprinted MIPs ($MIP_{caffeine}$) were prepared by combining and equilibrating the following for 30 minutes: 20 mg caffeine, 30 µL methacrylic acid, 235 µL ethylene glycol dimethacrylate, 0.7 mg of the photo initiator Irgacure 184, 184 µL DMSO, and 551 µL THF. Aspirin templated methacrylate-based polymers ($MIP_{aspirin}$) were prepared by combining and equilibrating (30 minutes) 48 mg aspirin, 0.7 mg Irgacure, 30 µL methacrylic acid, 235 µL ethylene glycol dimethacrylate, and 735 µL THF. For both $MIP_{aspirin}$ and $MIP_{caffeine}$, polymerization occurred using an OmniCure Series 1500 ultraviolet lamp with a 250 - 450 nm filter (P = 15 mW) for 30 minutes.

Lyophilization of the polymer samples took place in a Thermo Scientific Modulyo Freeze Dryer for at least 24 hours. Acetaminophen imprinted MIPs ($MI_{Pacetaminophen}$) were prepared by combining and equilibrating (30 minutes) 17 mg acetaminophen, 30 µL methacrylic acid, 235 µL ethylene glycol dimethacrylate, 5 mg AIBN, and 735 µL THF. Next, the monomer solution was purged with N_2, and the vial was capped. The vials were placed in a 60 °C oven for 24 hours to cure. The resulting $MIP_{acetaminophen}$ were lyophilized for at least 24 hours to remove solvent.

Drug templates were removed from the MIP via Soxhlet extraction for 8 hours with dichloromethane, methanol, and ethyl acetate for caffeine, acetaminophen, and aspirin, respectively. Drug removal was confirmed using Raman difference spectra (Figure 4.1). To improve polymer uniformity, the MIPs were ground using a mortar and pestle and sieved (mesh size 707 – 230). The 0 – 63 µm fraction was collected and used for subsequent analysis and use.

4.2.3 Size Analysis of the MIPs

Size analysis of fractionated MIPs was performed using DLS (Beckman Coulter DelsaNano C Particle Analyzer) and TEM (JEOL JEM-1230. The MIPs were prepared for DLS by suspending 1.74 mg of the dried MIP in 10 mM NaCl in water, sonicating for

~2 minutes, and incubating the samples at room temperature for 30 minutes prior to analysis. The resulting hydrated diameters were estimated assuming a Gaussian distribution. Non-hydrated particle diameters and MIP particle morphology were imaged using TEM and bright field microscopy. These samples were prepared by suspending 0.25 mg MIP in 50 % ethanol, pipetting 10 μL of the solution onto a carbon Formvar coated copper grid (400 mesh, Ted Pella, Redding, CA), and air drying overnight. The resulting images were analyzed using Image Pro Analyzer, and at least 35 polymer particles were evaluated per sample to estimate dried particle dimensions.

All Raman spectra were collected using an Examiner532 Raman spectrometer (DeltaNu) mounted on an Olympus IX71 microscope equipped with a 10x objective lens and a Hamamatsu ORCA-ER camera. Raman spectra were collected using the following parameters: excitation wavelength (λ_{ex}) = 532 nm, power (P) = 15 – 21 mW, integration time (t_{int}) = 3 – 15 seconds, and at least 30 averages. Raman intensities were collected in terms of photon counts (cts) but reported in units of $cts \cdot mW^{-1} \cdot s^{-1}$ to account for slight laser power variations. To determine vibrational peak intensities, the fluorescence background was removed using an Excel macro which determines a baseline by averaging 101 data points and subtracting this value from the middle point. Next, the spectral intensities were divided by the Raman intensity of the polymer C-C-O stretch at 600 cm^{-1} to account for sampling differences. Measurements were performed in triplicate, and error bars represent the standard deviation of these data.

4.2.4 Flow-Through Device Fabrication.

A methacrylate-based polymer weir was synthesized using a previously reported procedure.[219] Briefly, standard chromatography fittings (Cole-Parmer) were attached to a quartz capillary tube (outer diameter = 1 mm, inner diameter = 0.7 mm) and connected to PDMS tubing. A syringe pump (KD Scientific) was used to promote solution from a syringe into a waste reservoir. The capillary was rinsed in triplicate with 1 M HCl (15

min), water (5 min), 1 M NaOH (10 min), and water (5 min) at a 0.5 $mL \cdot min^{-1}$ flow rate. The capillary was then rinsed for 10 minutes with methanol, and vacuum was applied for 10 minutes to dry the device. Next, the capillary was filled with 1 % (v/v) solution of 3-trimethoxysilylpropyl acrylate in toluene and allowed to incubate overnight at 4 °C. The pendent acrylate groups were used for subsequent reaction with the methacrylate thereby forming a porous polymer plug in the capillary.[220]

The monomer solution for weir formation was prepared by combining 440 µL glycidyl methacrylate, 305 µL ethylene glycol dimethacrylate, 1.69 mg 2-acrylamido-2-methyl-propane-sulfonic acid, 7.98 mg AIBN, 227 µL methanol, and 1293 µL ethanol. (Note: aluminum oxide was used to remove the radical inhibitors from glycidyl methacrylate and ethylene glycol dimethacrylate.) After filling the capillary with the monomer solution (on ice), a transparent window (~2 mm) was formed on the capillary, and polymerization took place over 45 minutes using an OmniCure Series 1500 ultraviolet lamp with a 250-450 nm filter (P = 15 mW). After curing, the unreacted monomer was rinsed from the capillary using copious amounts of methanol. The resulting polymer weir contained pores with less than 1 µm diameters which simultaneously retained the ground MIP in the capillary while still allowing buffer to pass through the device for use in subsequent flow-through assays.

Fractionated MIP particles were packed into the flow-through devices by loading non-hydrated MIP particles into the capillary until a ~1 cm MIP phase formed and equilibrated by subsequently flowing HEPES buffer (~20 µL/min) through the device. Assays were then performed by flowing a 50 mM acetaminophen, aspirin, or caffeine solution (1.9 – 7 µL/min) through the device for 8 hours and by collecting Raman spectra every 15 minutes. A typical experimental set-up for flow through assays is shown in Figure 4.2. After each assay, the devices were rinsed with HEPES buffer until analyte peaks were no longer observed (6 - 8 hours).

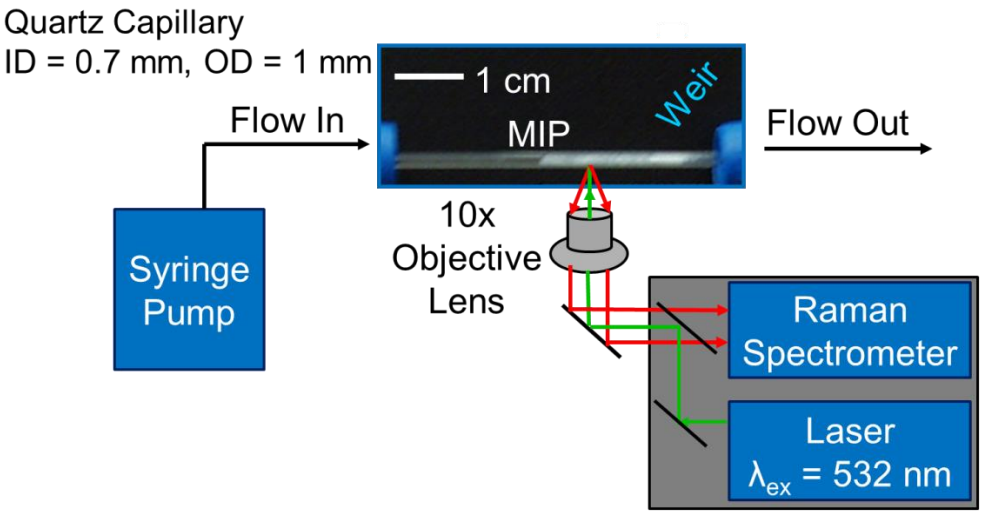

Figure 4.2. Experimental set-up for flow-through assays.

4.2.4 MIP Assays

A 25 mM HEPES buffer (pH 8.5) was prepared from HEPES, and slight pH adjustments were made with 1 M NaOH. All aspirin solutions were titrated with 1 M NaOH to prevent the formation of salicylic acid.[221] The ionic strength of acetaminophen and caffeine solutions was adjusted to 75 mM using NaCl. All solutions were filtered using a 0.2 µm nylon filter (Whatman, Middelsex, UK) prior to use. For detection assays under steady-state conditions, fractionated MIP samples were suspended in drug solutions (2 mg/mL) and incubated for at least 12 hours. The dissociation constant and concentration of binding sites for each MIP was estimated using a binding model (vide infra) and quantified using numerical approximations (DynaFit 3). Over-counter drug assays were performed by grinding and dissolving a pill in HEPES buffer so that the final concentrations of the drugs equaled 70, 58.7 and 14.1 mM for acetaminophen, aspirin, and caffeine, respectively. The solution was sonicated for 2 hours, and the non-soluble

drug fillers were removed by centrifuging the solution for 5 minutes at 5000 xg. The supernatant was collected and used for subsequent over-the-counter drug assays.

4.2.5 Imprint Site Geometries.

The imprint site volume/orientation was modeled using Spartan (Spartan '10, Version 1.1.0). In order to model the imprint site using Spartan, the complex polymer matrix was assumed to not significantly impact the binding site geometry or hydrogen bonding between the functional monomer (methacrylic acid) and the drugs; therefore, the imprint site was simplified by optimizing binding site geometries using multiple methacrylic acid monomers and either acetaminophen, aspirin, or caffeine.

Calculations were performed in series starting with a Hartree Fock 3-21G basis set, followed by DFT B3LYP 6-31G, DFT B3LYP 6-31+G, and finally DFT B3LYP 6-31+G* (or until the results converged).[222] Performing the calculations in a series ensured that the calculations were successfully completed (i.e., energy minimized and optimized binding site geometries obtained). The optimized binding site geometry provides insight into which drug functional groups would participate in hydrogen bonding with the imprint site thereby inducing predictable changes in vibrational band energies.

4.3 Results and Discussion

4.3.1 Unique Vibrational Band Assignments

Narrow, unique vibrational features observed with Raman spectroscopy and simplified using MIP recognition elements provide an ideal detection and recognition platform for bioassays and complex drug mixture analysis.[214] For instance, Figure 4.3 depicts the molecular structures and Raman spectra of 70 mM (1) caffeine, (2) acetaminophen, and (3) aspirin in 25 mM pH 7.0 HEPES buffer along with the (4) methacrylate-based non-imprinted polymer. The drugs and polymer exhibit both overlapping and unique vibrational bands (complete assignments found in Table 4.1);

however, unique vibrational modes located at 556 cm^{-1} (C-N-CH_3 deformation),[223] 1172 cm^{-1} (phenyl stretch),[224] and 1033 cm^{-1} (CH_3 rocking)[225] for caffeine, acetaminophen, and aspirin, respectively (Table 4.2) allow for drug identification and quantification using MIPs. Additional advantages of this approach include the large S/N of pre-concentrated drugs in the MIP and unique vibrational modes of these molecular species in buffer, MIP, and complex sample mixtures (vida infra). Finally, the Raman band associated with the methacrylate stretch at 600 cm^{-1} serves as an internal reference for the assays because this polymer feature neither changes upon polymerization nor overlaps with the identified unique spectral features for each drug.[226,227]

Table 4.1. Raman vibrational band assignments for acetaminophen, aspirin, caffeine, and polymer

Raman Shift (Δcm^{-1})		Assignment	Molecule
Solution	MIP		
558	555	d(C-N-CH_3)	Caffeine
	600	ν(C-C-O)	Polymer
703	696	d(O=C-N)	Caffeine
	708	δ(C-H out of plane)	Polymer
764	746	d(O-H), δ(C-H ring)	Aspirin
801	799	ν(Phenyl ring)	Acetaminophen
	809	ν_s(C-C-C)	Polymer
834	828	ν(C-N-C)	Acetaminophen
	857	ν(C-COOH)	Polymer
867	860	Ring breathing	Acetaminophen
928	910	δ(In-plane O-CO-CH_3)	Aspirin
934	912	ν_s(N-CH_3)	Caffeine
	954	r($C(CH)_3$)	Polymer

Table 4.1. -Continued

	1010	r(CH_3)	Polymer
1037	1033	r(CH_3)	Aspirin
	1049	ν(C-C)	Polymer
	1126	r(CH_3)	Polymer
	1160	δ(C-H ring)	Aspirin
1174	1172	δ(Phenyl)	Acetaminophen
	1192	ν(C-O), δ(O-H in plane)	Polymer
1238	1235	r(Phenyl amide OH)	Acetaminophen
1245	1241	ν(Ester),ν(C-N)	Polymer, Caffeine
1255	1255	ν_a(ester C-O)	Aspirin
1284	1281	d(O-H),ν(C-O)	Acetaminophen
1296	1290	$(CH_3)_n$ twisting vibration, ν(C-	Polymer, Caffeine
1330	1324	ν(Phenyl OH)	Acetaminophen
1338	1332	ν(C-N)	Caffeine
1380	1377	$d_a(CH_3)$, $d_s(CH_3)$	Polymer, Acetaminophen
	1452	δ(CH_2)	Polymer
1518	1518	ν(C-NH)	Acetaminophen
1565	1563	ν(O=C-N)	Acetaminophen
1609	1608,	ν(C=C)	Aspirin, Caffeine
1619	1619	ν(C=C)	Acetaminophen
	1643	ν(C=C)	Polymer
	1725	ν(C=O)	Polymer

Note: Abbreviations: δ = bending; d = deformation; ν = stretching, r = rocking, a = asymmetric, s = symmetric.

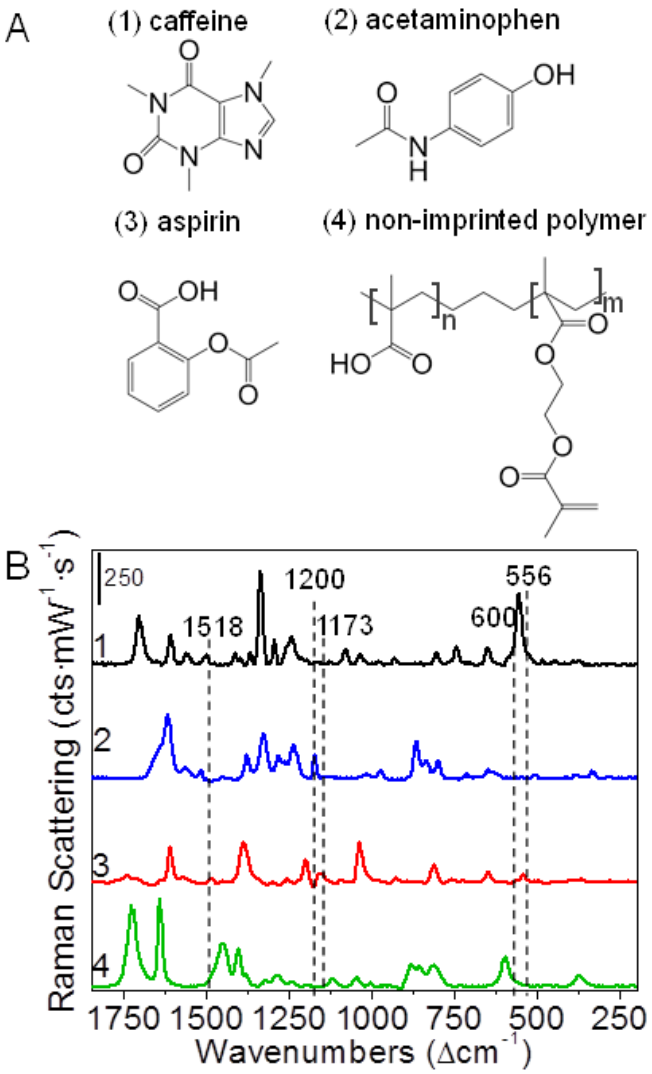

Figure 4.3. (A) Structures and (B) Raman spectra of 70 mM (1) caffeine, (2) acetaminophen, (3) aspirin in 25 mM HEPES buffer (pH = 7.0), and (4) methacrylate polymer. The unique vibrational modes are labeled and listed in Table 1. Raman parameters: λ_{ex} = 532 nm, P = 40 mW for caffeine, aspirin, and non-imprinted polymer and 24 mW for acetaminophen, t_{int} = 7, 6, 11, and 1 s for caffeine, acetaminophen, aspirin, and non-imprinted polymer, respectively.

Table 4.2. Unique vibrational band assignments for acetaminophen, aspirin, caffeine, and polymer.

Raman Shift (Δcm^{-1})		Assignment	Molecule
In Solution	MIP-Bound		
558	555	d(C-N-CH_3)	Caffeine
Not applicable	600	ν(C-C-O)	Polymer
1037	1033	r(CH_3)	Aspirin
1330	1324	ν(Phenyl OH)	Acetaminophen

Note: Abbreviations: d = deformation; ν = stretching, r = rocking.

4.3.2 Raman Vibrational Shift Analysis

Molecules in solution or bound to a MIP exhibit local environmental dependent Raman vibrational energies and peak widths.[77,228-230] Hydrogen bonding between the MIP and drug results in an increased bond length for the relevant vibrational stretch/bend.[222,229,231] This causes the relevant vibrational force constant to decrease thereby resulting in a red-shift in those observed Raman band frequencies for a drug bound to a MIP vs. in solution.

As shown in Figure 4.4, standard methacrylate polymerization procedures employing methacrylic acid as the functional monomer and ethylene glycol dimethacrylate as the cross-linking monomer enables the formation of acetaminophen, aspirin, and caffeine templated-MIPs. Subsequent analysis using Raman microscopy allows for the quantification of drugs via molecular vibrational energy changes by comparing sample spectra in MIPs and buffer.[232] Gaussian fits (red dashed lines) illustrate shifts in the unique Raman modes after polymerization indicating drug molecule interactions with the polymer template (Figure 4.4).

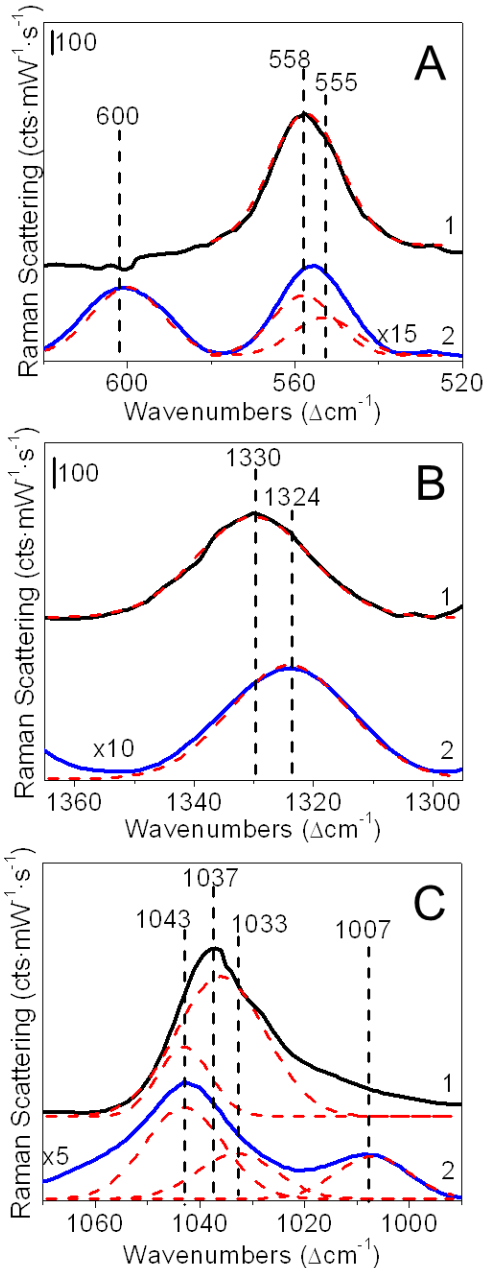

Figure 4.4. Representative Raman spectra for (A) caffeine, (B) acetaminophen, and (C) aspirin (1) in solution and (2) templated in the MIP. The unique vibrational modes are determined with Gaussian fits (red dashed line) and labeled for aspirin (1037 and 1033 cm^{-1}, CH_3 rocking), acetaminophen (1330 and 1324 cm^{-1}, phenyl OH stretch), caffeine (558 and 555 cm^{-1}, C-N-CH_3 deformation), and polymer (600 cm^{-1}, C-C-O stretch; 1043 cm^{-1}, C-C stretch; 1007 cm^{-1}, CH_3 rocking). The spectra are offset and spectra are multiplied by (A-1) 15, (B-2) 10, and (C-2) 5 for clarity. Raman parameters: λ_{ex} = 532 nm, (A) tint = (1) 7 s, (2) 5 s, P = 40 mW; (B) t_{int} = (1) 6 s, (2) 14 s, P = 24.9 mW; (C) tint = (1) 11 s, (2) 2 s, P = (1) 40 mW, (2) 24 mW.

For instance, the unique Raman band for caffeine red-shifts from 558 cm^{-1} in buffer to 555 cm^{-1} (C-N-CH_3) when bound to the MIP (Table 4.2, Figure 4.4A). Importantly, this 3 cm^{-1} red-shift indicates that the oxygen containing functional groups form hydrogen bonds with the methacrylate polymer near the C-NCH_3 functional group. The energy-minimized imprint geometry calculated by Spartan for methacrylic acid hydrogen bonded to caffeine further supports the Raman data that suggests methacrylic acid hydrogen bonds to caffeine near the C-NCH_3 functional group (Figure 4.4A). Similarly, unique Raman bands for acetaminophen (Figure 4.4B-1) red-shift by 1 cm^{-1} to 1172 cm^{-1} from 1173 cm^{-1} (phenyl bending) and by 6 cm^{-1} to 1324 cm^{-1} from 1330 cm^{-1} (phenyl OH bend) when bound to the templated polymer vs. in solution, which also indicates that the OH group in acetaminophen participates in hydrogen bonding to the polymer backbone (Table 4.1). Furthermore, the energy-minimized imprint geometry for methacrylic acid undergoes hydrogen bonding to acetaminophen via the OH group in acetaminophen (Figure 4.5B). Finally, the unique Raman bands for aspirin bound to the MIP are centered at 1608 cm^{-1} from 1609 cm^{-1} in buffer (C=C benzene stretch, a 1 cm^{-1} red-shift) and 1033 cm^{-1} from 1037 cm^{-1} in buffer (CH_3 rocking, a 4 cm^{-1} red-shift) (Table 4.2, Figure 4.4B). Consistent with the other two drugs, this significant 4 cm^{-1} red shift observed for the CH_3 rocking vibrational mode in aspirin when MIP-bound vs. suspended in buffer indicates that the oxygen in the carbonyl group hydrogen bonds to the methacrylic acid polymer background. Again, energy-minimized imprint geometries of aspirin in the MIP verify this experimental observation (Figure 4.5C).[222,232]

Importantly, not all vibrational features in a molecule undergo spectral changes in response to their local environment. Several are noted in these data. The insignificant (red) shifts associated with the 1172 cm^{-1} vibrational mode for acetaminophen and 1609 cm^{-1} vibrational mode for aspirin indicate a lack of environmental sensitivity of these modes thereby precluding the use of these features for identifying bound drug. The lack

of overlap of the 1172 cm^{-1} acetaminophen vibrational feature with other spectral features, however, facilitates the use of this peak for quantification purposes.

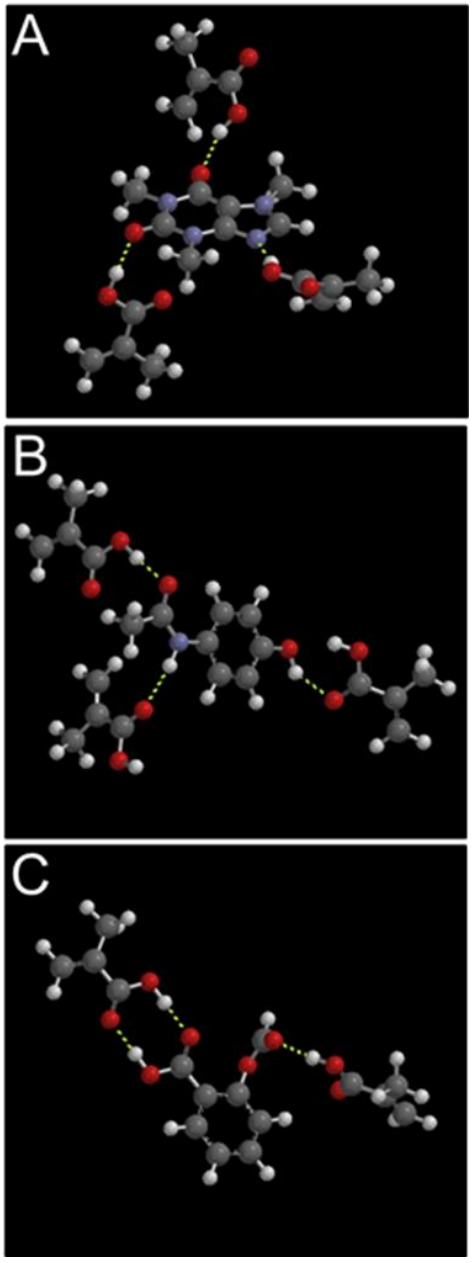

Figure 4.5. Spartan models of the energy minimized imprint geometries for (A) caffeine, (B) acetaminophen, and (C) aspirin hydrogen bonded to methacrylic acid in the polymer backbone (Red = Oxygen, Dark Gray = Carbon, Light Gray = Hydrogen, Dotted yellow lines = Hydrogen bonds).

4.3.3. Analysis of MIP Size and Morphology

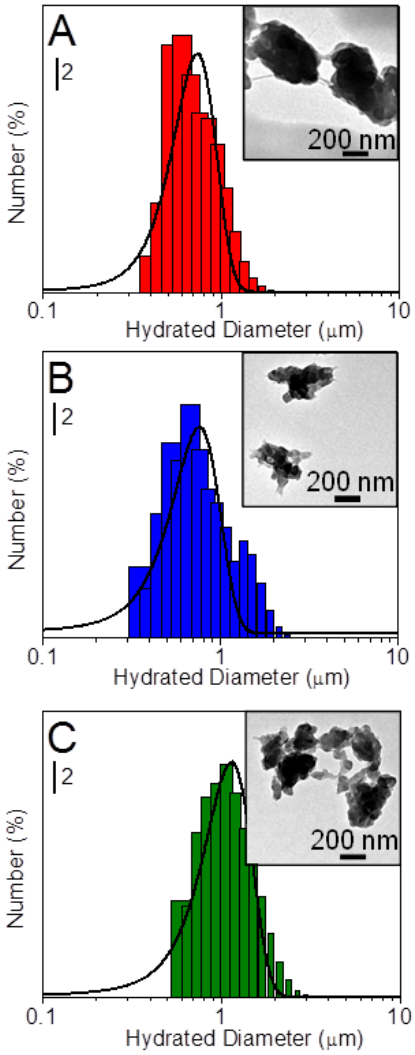

Figure 4.6. Size analysis using DLS and TEM (inset) of (A) $MIP_{caffeine}$, (B) $MIP_{acetaminophen}$, and (C) $MIP_{aspirin}$. Using a Gaussian fit of the data (black line), hydrated mean diameters were 740 ± 200, 760 ± 230, 1140 ± 350 nm for $MIP_{caffeine}$, $MIP_{acetaminophen}$, and $MIP_{aspirin}$, respectively (9 measurements were averaged for all samples). The mean dimension from TEM is 421 ± 128 nm (n = 50), 345 ± 113 (n = 51), and 284 ± 117 (n = 35) for $MIP_{caffeine}$, $MIP_{acetaminophen}$, and $MIP_{aspirin}$, respectively.

While preparation of the MIP samples is straight forward, the inherent fragility of the MIP samples, which easily break into small pieces after lyophilization, limits practical handling and reproducible usage of these materials. To overcome this drawback, MIPs are ground using a mortar and pestle and sieved to improve particle size homogeneity. The number of accessible binding sites available during assays increase which should improve the uniformity of drug recognition capabilities. Additionally, fractionating the ground polymers using a sieving stack (mesh size 707 – 230) and collecting only the 0 – 63 µm fraction, improves polymer particle size homogeneity.

To evaluate the morphology and size of the MIP samples, 0.25 mg of the polymer powder is suspended in 1 mL of 50% ethanol and then spotted onto a TEM grid which is dried for 24 hours at room temperature. Analysis of the resulting TEM images yields mean MIP particle dimensions of 421 ± 128 (number of particles (N) = 35), 345 ± 113 (N = 51), and 284 ± 117 (N = 35) nm for $MIP_{caffeine}$, $MIP_{acetaminophen}$, and $MIP_{aspirin}$ samples, respectively (Figure 4.6, Insets). As expected, these average particle dimensions are within the collected fraction window which indicates that grinding the polymer particles with a mortar and pestle followed by sieving successfully yields fractionated polymer particles.

While TEM provides valuable details regarding non-hydrated particle morphology, DLS reveals hydrated particle diameters. For DLS measurements, ground polymer particles are suspended in 10 mM NaCl (1.74 mg polymer/mL NaCl), sonicated for 5 – 10 seconds, and incubated at room temperature for 30 minutes. Fitting the resulting DLS data with a Gaussian function facilitates the determination of the hydrated diameters of these samples. Mean hydrated diameters are 740 ± 200, 760 ± 230, and 1140 ± 350 nm for $MIP_{caffeine}$, $MIP_{acetaminophen}$, and $MIP_{aspirin}$, respectively (Figure 4.6). The differences in mean diameters observed between DLS and TEM are attributed to polymer swelling in aqueous environments and irregular particle morphologies. Importantly, both

DLS and TEM indicate relatively monodisperse (RSD < 40%) fractionated polymer particle samples, and these morphologies can be used for subsequent binding studies.

4.3.3 Evaluation of Drug Binding under Steady State Conditions

After grinding and characterizing the MIPs, incubation of a known mass of MIP (2 mg polymer/mL) with varying drug concentrations ranging from 0 – 300 mM for at least 12 hours allows for the saturation of drug binding sites in the MIPs and quantitative drug detection. These drug concentrations correspond to relevant drug concentrations[233] as well as drug solubility limits in buffer at 20 °C. Figure 4.7 shows representative Raman spectra for each drug which is concentrated in the polymer matrix at MIP recognition binding sites. As a result, the Raman signal should and are observed to increase linearly until the recognition sites in the MIP are filled (Figures 4.75A-4.7C). The unique vibrational bands at 555 cm^{-1}, 1172 cm^{-1}, and 1032 cm^{-1} for $MIP_{caffeine}$, $MIP_{acetaminophen}$, and $MIP_{aspirin}$, respectively, are relative to the polymer band and used for quantification (Figure 4.7D-4.7F). As expected, these relative Raman intensities increase as the drug concentration increases from 0 to 100 mM which is a typical range in quantitative Raman responses. Signals exhibit non-linearity, however, at higher drug concentrations. Both drug supersaturation and precipitation contribute to this non-linearity and result in large error bars in estimated aspirin and caffeine concentrations.

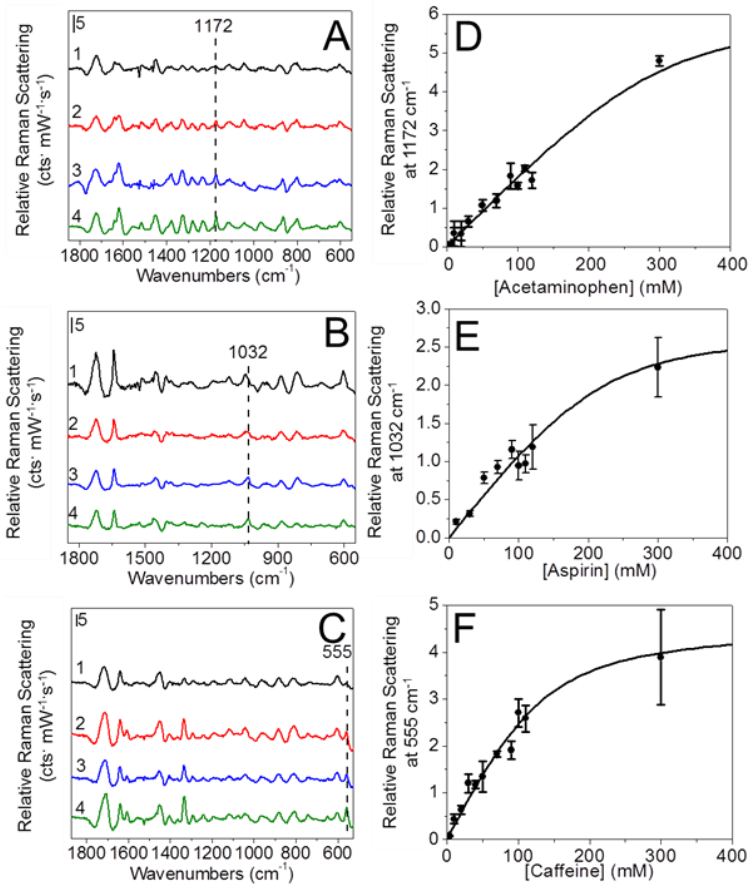

Figure 4.7. (A) Relative Raman spectra of $MIP_{acetaminophen}$ incubated in (1) 10, (2) 30, (3) 50, and (4) 90 mM acetaminophen. Acetaminophen Raman band at 1172 cm^{-1} (phenyl bending) is labeled with a dotted line. (B) Relative Raman spectra of $MIP_{aspirin}$ incubated in (1) 10, (2) 30, (3) 50, and (4) 90 mM aspirin. Aspirin Raman band at 1032 cm^{-1} (CH_3 def.) is labeled with a dotted line. (C) Relative Raman spectra of $MIP_{caffeine}$ incubated in (1) 10, (2) 30, (3) 50, and (4) 90 mM caffeine. Caffeine Raman band at 555 cm^{-1} (C-N-CH_3 def.) is labeled with a dotted line. Raman parameters: λ_{ex} = 532 nm, t_{int} = 4 – 15 seconds, P = 16 mW. The fluorescence background was removed from all spectra using an in-house written Excel program. All spectra are relative to the polymer band at 600 cm^{-1} (C-C-O stretch) to account for sampling differences. (D) Relative Raman intensity at 1172 cm^{-1} as a function of acetaminophen concentration in the incubation solution. (E) Relative Raman intensity at 1032 cm^{-1}as a function of aspirin concentration in the incubation solution. (F) Relative Raman intensity at 555 cm^{-1} as a function of caffeine concentration in the incubation solution. The black line represents a numerical approximation binding model determined using DynaFit. The error bars represent three replicate measurements.

To better assess and quantify the number of saturated binding sites of drug molecules to MIP recognition sites, numerical approximation of this equilibrium interaction is modeled using DynaFit 3.[234] Applying the numerical approximation binding model to Raman intensity as a function of drug concentration allows for an estimation of the K_{eq} and concentration of total drug binding sites for each MIP. The following simplified equilibrium binding model describes the Drug-MIP interaction as follows assuming a single binding site:[235,236]

$$\text{Drug} + \text{MIP} \rightleftharpoons \text{Drug-MIP} \qquad \text{where } K_{eq} = \frac{[\text{Drug-MIP}]}{[\text{MIP}][\text{Drug}]} \tag{1}$$

where additional hydrogen bonding interactions between the drug molecules and the MIP imprint sites increases the equilibrium constant[237] which promotes Drug-MIP complex formation.

To quantify the binding interactions between the drug and MIP, the apparent maximum binding capacity of the drug to the MIP thereby forming drug-MIP complex, total number of drug binding sites in the MIP, molar response coefficient (i.e., signal response as a function of drug concentration), and finally K_{eq} values are numerically approximated by minimizing the fit for the concentration dependent Raman signals. First, the apparent maximum binding capacities of the drug to the MIP at equilibrium are approximated and equal 302.6 ± 17.6, 215.7 ± 15.5, 124.1 ± 7.4 mM for Acetaminophen-$MIP_{acetaminophen}$, Aspirin-$MIP_{aspirin}$, and Caffeine-$MIP_{caffeine}$ respectively. These concentrations represent the total concentration of binding sites in the hydrated MIP per 2 mg of dry MIP. From these saturated binding capacity values, the total number of binding sites per gram of polymer can be estimated using the amount of MIP used. These binding site densities correspond to (82.6 ± 4.8) x 10^{18}, (58.9 ± 4.2) x 10^{18}, and (33.9 ± 2.0) x 10^{18} binding sites per gram of dry polymer for $MIP_{acetaminophen}$, $MIP_{aspirin}$, and $MIP_{caffeine}$, respectively, which correspond to 50%, 16%, and 24% of the theoretical total binding

sites possible. Differences in the observed binding sites in each polymer are unique because of the templating method as well as variations in drug concentration and solubility used during pre-polymerization steps.

Third, the molar response coefficients from numerical analysis are then used to convert all subsequent experimental data to concentration[238] and are estimated to be 20.0 ± 0.9 µM, 12.8 ± 0.8 µM, and 37 ± 2 µM for $MIP_{acetaminophen}$, $MIP_{aspirin}$, and $MIP_{caffeine}$, respectively. Finally, using the numerically approximated binding site density and molar response coefficients, K_{eq} values for the respective drugs with $MIP_{acetaminophen}$, $MIP_{aspirin}$, and $MIP_{caffeine}$ are estimated to be 6.7 ± 0.03, 8.7 ± 0.1, and 12.3 ± 0.1 M^{-1}, respectively. These calculated K_{eq} values are lower than previously reported equilibrium constants for methacrylate based molecular imprinted polymers, which range from 1 x 10^6 to 1 x 10^3 M^{-1}.[239,240] The low K_{eq} values are predicted to result from the production of non-specific binding sites on the MIP surface that occur after grinding the MIP, which leads to a distribution of recognition sites.[47] While these results suggest that the proposed binding model is an oversimplification of binding interactions between the MIP and drugs, this simple model allows for the determination of equilibration binding constants, warranting the use of the MIPs for steady-state drug-based assays.

Previously, chromatographic enrichment was observed during affinity chromatography studies.[241-243] In particular, low concentrations of target species (i.e., lower than the available number of binding sites in the sample) were amplified by the column material. To determine the amount of amplification possible, an enrichment factor is calculated for the drug templated MIPs using the following equation:[244]

$$\text{Enrichment Factor} = \left(\frac{m_{MIP}}{m_{buffer}}\right)\left(\frac{V_{wet}}{V_{dry}}\right) \quad (2)$$

where m_{MIP} and m_{buffer} are the slopes of the linear portion of the relative Raman Intensity as a function of drug concentration in the presence and absence of MIP, respectively, and V_{dry} and V_{wet} are the volume of the dry and wet polymer, respectively. The volume ratio

(V_{wet}/V_{dry}) corrects for the density changes in the polymer upon swelling and was calculated using the average diameters determined from DLS and TEM for V_{wet} and V_{dry}, respectively.

Using the values reported in Table 4.3, the calculated enrichment factors are 25x, 8x, and 2x for $MIP_{aspirin}$, $MIP_{acetaminophen}$,and $MIP_{caffeine}$, respectively. These calculated values agree with previously reported enrichment factors for methacrylate-based MIPs, which range from 2 – 102x.[245] Both $MIP_{acetaminophen}$ and $MIP_{caffeine}$ exhibit approximately the same enrichment factor while $MIP_{aspirin}$ exhibited approximately 3x enrichment vs. the other two MIPs. These results suggest that the degree of swelling of the hydrated polymer as well as drug solubility in buffer can influence the amount of enrichment observed.

Table 4.3. Parameters used for enrichment factor determination.

	m_{MIP} (cts·mW-1·s-1·mM-1)	m_{buffer} (cts·mW-1·s-1·mM-1)	V_{wet}/V_{dry}
$MIP_{aspirin}$	0.092	0.242	65
$MIP_{acetaminophen}$	0.178	0.233	11
$MIP_{caffeine}$	0.154	0.477	5

4.3.4 Evaluation of Drug Detection using MIPs and an Over-the-Counter Drug Sample

Recognition of any ligand to a receptor is dictated by the binding constant, binding kinetics, competition of interfering species for binding recognition, as well as signal transduction-limited detection capabilities.[235] For instance, the selectivity of these

and other MIPs to target molecules is generally poor in comparison to standard recognition agents.[239,240] While important advances in purification and preparation of these materials increased the effective K_{eq} values and improved the resulting limits of detection,[42,49,59] additional detection advantages are offered using Raman spectroscopy. Raman scattering provides a viable detection alternative to MIP based assays without MIP improvement or purification. Furthermore, drug enrichment in the MIPs is possible for trace detection in complex sample analysis. Both effects are hypothesized to be advantages of drug detection using MIP recognition agents and Raman microscopy for detection.

To evaluate the effectiveness of Raman microscopy coupled with MIPs, a commercial migraine medication that contains caffeine, acetaminophen, and aspirin is selected to assess the recognition and enrichment capabilities of each MIP and drug couple. Incubation of $MIP_{caffeine}$, $MIP_{acetaminophen}$ or $MIP_{aspirin}$ samples with an over-the-counter migraine solution containing 14.1 mM caffeine, 70.0 mM acetaminophen, and 58.7 mM aspirin reveal spectra with many vibrational features (Figure 4.8). These spectra clearly reveal complex spectral feature characteristics of each drug, polymer, and (competing) drug. While each drug is observed in all MIPs (both selectively and non-selectively), evaluation of the unique Raman vibration features reveal that each drug binds to the partner MIP with some specificity. To quantify and compare the amount of target drug recognized by each MIP, the derived binding response curves in Figure 4.7 are used. Table 4.4 summarizes the concentration of all three drugs in the over-the-counter drug solution as well as the detected drug concentration using the partner MIP. In all cases, more than 85% of the drugs available in the sample are successfully detected by their partner MIP. Acetaminophen and aspirin detection approached ~90% of the original sample while caffeine detection is on average 174% as determined by dividing the drug concentration detected in the MIP by the drug concentration in the over-the-counter drug solution. These data can be understood by considering the amount of caffeine originally

present in each sample as well as the drug binding site densities in each MIP and estimated dissociation constant. As stated previously, the MIPs exhibit enrichment capabilities in simple drug mixtures. Similar effects are hypothesized using the over-the-counter drug solution. On average, 64.5 mM acetaminophen is detected from the original, 70 mM sample. Aspirin concentrations of ~51 mM are easily detected from the same solution which contained 58.7 mM drug. Caffeine, which was present in the relatively lowest level (14.1 mM) is observed at levels of 24.5 mM using MIP recognition.

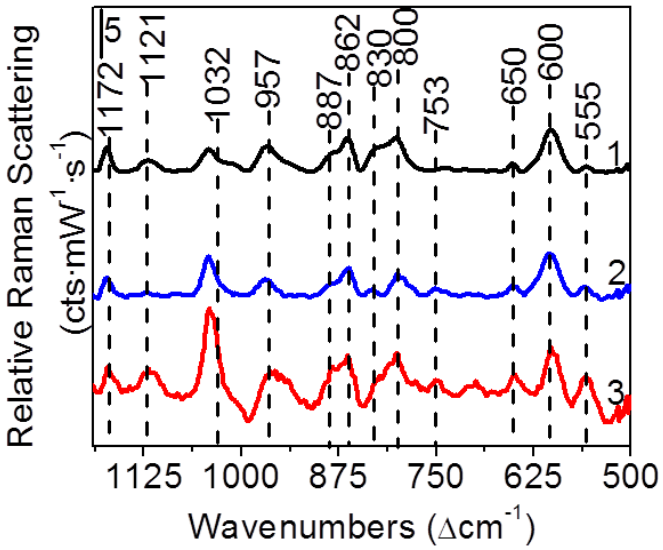

Figure 4.8. Representative relative Raman spectra of an over-the-counter migraine medication MIP assay in (1) $MIP_{acetaminophen}$, (2) $MIP_{caffeine}$, and $MIP_{aspirin}$. The vibrational bands for acetaminophen (1172 cm^{-1}, phenyl bending; 862 cm^{-1}, ring breathing; 830 cm^{-1}, C-N-C stretch), aspirin (1200 cm^{-1}, C-H in-plane deformation;1032 cm^{-1}, CH_3 rocking, 753 cm^{-1}, O-H deformation), caffeine (555 cm^{-1}, C-N-CH_3 deformation), and polymer (1121 cm^{-1}, CH3 rocking; 1044 cm^{-1}, C-C stretch; 957 cm^{-1}, $C(CH_3)_3$ rocking; 887 cm^{-1}, C-C-C(CH) stretch; 800 cm^{-1}, C-C-C stretch; 600 cm^{-1}, C-C-O stretch) are labeled with a dotted line. Raman parameters: λ_{ex} = 532 nm, t_{int} = 10 s, P = 15.5 mW.

Considering the ranges of drug recovery observed with these unpurified mixtures, some enrichment is observed with each of these MIPs for their partner drug. These results

suggest that the ratio of binding sites to drug added to each MIP sample can influence the amount of chromatographic enrichment observed. The ratio of total MIP binding sites to drug was determined by dividing the total concentration of binding sites in the MIP by the drug concentration in the over-the-counter drug solution resulting in 4.3, 3.7, and 8.8 for acetaminophen, aspirin, and caffeine, respectively. While an excess of drug binding sites is present in each sample, the average drug recovery correspond with these binding site:drug trends. Notably, the number of caffeine binding sites is ~two times larger than that for either acetaminophen or aspirin. Similarly, caffeine was observed in ~twice the original concentration. These results suggest that these enrichment effects must be considered for future quantitative detection of small molecules in mixtures using MIPs.

Table 4.4. Concentration of bound drug in the MIP after incubation in the over-the-counter drug solution.

	Acetaminophen	Aspirin	Caffeine
Known Over-the-Counter Drug Solution Concentration (mM)	70	58.7	14.1
MIP (mM)	64.5 ± 11.9	50.8 ± 22.1	24.5 ± 7.9

4.3.5 Implications of Flow in Drug Binding to MIPs.

All binding measurements presented to this point were collected under stagnant conditions which required at least 4 hours to reach steady state. To overcome these long equilibration periods, flow conditions can be utilized.[246,247] To do this, MIP particles are loaded into flow-through devices. Briefly, a methacrylate-based weir is polymerized in a quartz capillary equipped with standard chromatography fittings. Next, ground polymer is loaded into the flow-through device until a ~1 cm MIP phase forms. This polymer plug is equilibrated by subsequently flowing HEPES buffer (~20 µL/min) through the device. To perform a flow-through assay, a 50 mM acetaminophen, aspirin, or caffeine solution (1.9

– 7.14 µL/min) is passed through the device for 4 hours and Raman spectra are collected every 15 minutes.

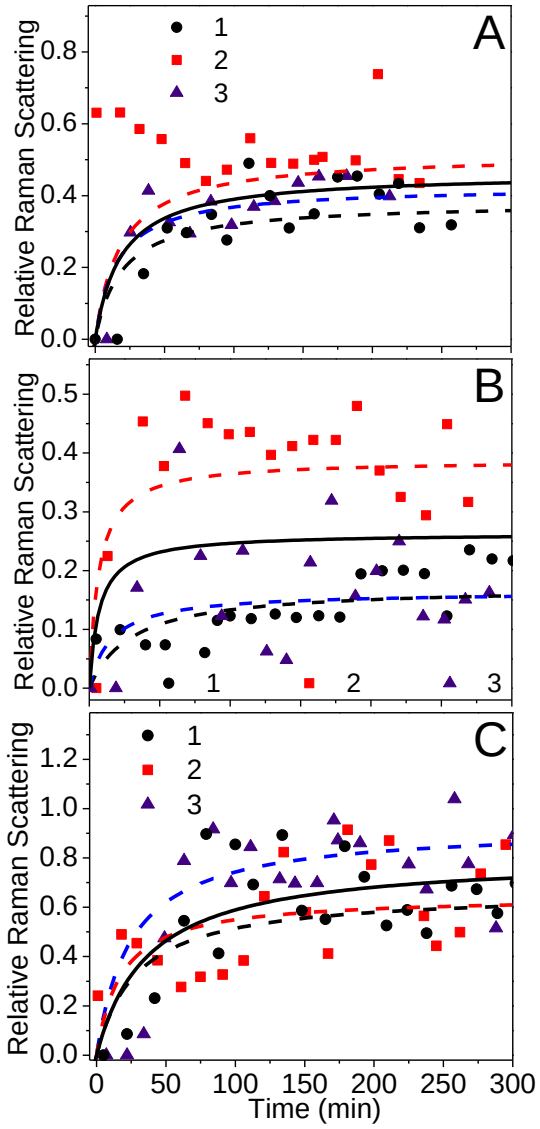

Figure 4.9. Evaluation of drug binding at low flow rates. Binding of 50 mM (A) acetaminophen to MIP at (1) 1.9, (2) 4.1, and (3) 5.6 µL/min; (B) aspirin to MIP at (1) 3.03, (2) 4.65, and (3) 7.05 µL/min; and (C) caffeine to MIP at (1) 2.24, (2) 5.19, and (3) 7.14 µL/min. In each plot, dotted lines represent hyperbolic fits for each individual flow rate while the solid line represents analysis for all flow rates. The maximum value of each y axis (Relative Raman Intensity) is set as the largest signal observed for the drug concentration at steady state conditions.

To evaluate drug binding at low flow rates (i.e., less than 10 µL/min, the relative Raman intensities of the unique drug band are plotted as a function of assay time (Figure 4.9). Dotted lines representing hyperbolic fits[248] for each individual flow rate are included. The maximum value of each y axis (Relative Raman Intensities – unique drug band divided by the polymer band) is the largest signal observed for the drug concentration at steady state conditions. While slight differences in the time dependent responses are observed for acetaminophen, caffeine, and aspirin, no systematic trend is apparent. As a result, the data are averaged and fit to obtain kinetic information about the drug detectability (solid lines). Specifically, the relative Raman intensities saturate at 0.4_6, 0.8_1, and 0.2_6 for $MIP_{acetaminophen}$, $MIP_{caffeine}$, and $MIP_{aspirin,}$ respectively, in the flow-through assay.

These values correspond to ~50% of the relative Raman intensities achieved at steady state conditions for all three drugs. This drop in saturated binding capacity is attributed to transport-limited binding rates of the drugs to the binding sites at the selected low flow rates.[249] While lower effective binding capacities are observed with the flow-through devices in comparison to the stagnant studies, the time required to reach half saturation is ~20, ~40, and ~ 7 minutes for the $MIP_{acetaminophen}$, $MIP_{caffeine}$, and $MIP_{aspirin}$ devices, respectively. These observed response times are 20x faster than that of assays performed under stagnant conditions and is attributed to the active diffusion of drug in the flow-through device.[246] Further optimization of these flow-through conditions could facilitate short assay times while simultaneously allowing MIP samples to be used in repeated assays.

4.4 Conclusions

Numerical analysis of narrow vibrational features in Raman spectra as a function of drug concentration facilitated the successful quantitative and qualitative detection of

three drug molecules in the presence of competing species. First, weakly selective MIPs were synthesized in the presence of a target drug, and the template species were removed leaving behind molecular cavities in the polymer matrix. Next, Raman spectra of the drug in solution and MIP were compared. Shifts in the unique vibrational Raman frequencies between spectra collected in these media for each drug were observed, modeled, and subsequently attributed to hydrogen bonding between the drug and polymer backbone. Third, monitoring and modeling the Raman intensity of the unique vibrational bands for each drug as a function of drug concentration yielded the binding capacity and equilibrium binding constants for each of the MIPs to their drug partner. These response functions were then used for quantitative detection of a complex over-the-counter medication. Of note, chromatographic induced drug enrichment in the MIPs was observed which bolstered detection limits. Finally, MIPs were loaded into flow through devices to reduce the required time per assay and increase the reusability of MIPs as recognition agents. This was achieved and ~half of the drug was detected in ~20 times less time than required in stagnant assays. While MIP selectivity was modest and consistent with previous investigations, detection of the unique Raman band of the target drug molecules allowed for drug identification within a complex sample. As a result, MIP recognition agents in conjunction with Raman microscopy provided a rapid and direct method of quantitative and qualitative detection of drug samples.

CHAPTER 5 INCORPORATION OF GOLD NANORODS INTO MOLECULAR IMPRINTED POLYMERS FOR SERS

5.1 Introduction

In recent years, the incorporation of nanomaterials into molecular imprinted polymers resulted in the development of sensitive and selective biosensors. Specifically, noble metal nanoparticle and MIP networks yielded selective detection of biomolecules,[250-254] drugs,[255-261] environmental contaminates,[262,263] and explosives.[264] Noble metal (Au, Ag, and Cu) nanomaterials are ideal for these sensor platforms because of their unique extinction (absorption + scattering) properties, which can be tuned throughout visible to near-infrared wavelengths by varying the local dielectric environment (*i.e.*, the surrounding medium and/or surface modification), metal, shape, or size.[63,265,266] Extinction spectra arise when the frequency of the incident electromagnetic field is in resonance with the oscillation of conduction band electron energy associated with the nanoparticles. This phenomenon is known as the localized surface plasmon resonance (LSPR) and can be exploited for sensor signal enhancement and transduction.[66]

The localized electromagnetic fields that arise from the LSPR are the primary contributor to the enhanced signals observed in surface-enhanced spectroscopies including surface-enhanced Raman scattering (SERS).[267,268] In addition, interactions between the molecular and nanoparticle electronic structures through charge transfer and resonance enhancements lead to short-range signal contributions which also increase the overall SERS signals for molecules near the metal surface.[269] All in all, SERS improves molecular detection by enhancing the magnitude of Raman scattering signal up to 9 orders of magnitude for a given analyte as a result of both chemical and electromagnetic enhancement effects.[270]

Applications involving SERS range from biological to environmental detection and often rely on recognition agents to provide selective detection. For instance, SERS

enhancements of 2,4,6-trinitrotoluene was demonstrated by Li et al. using imprinted xerogel films coated on a SERS active substrate.[263] Unique vibrational bands of 2,4,6-trinitrotoluene allowed for both qualitative and quantitative detection even in the presence of structurally similar molecules. Unfortunately, the detection limit for the 2,4,6-trinitrotoluene MIP SERS substrate was not adequate for sub-μM detection of trace explosives. The small signals observed were limited by either 1) the number of molecules near the SERS substrate and/or 2) the well-known distance dependence of the SERS effect.[255,264] Clearly, understanding and promoting nanomaterial and MIP interactions are vital for achieving maximum SERS enhancements and realizing biologically-relevant detection limits for small molecules.

Herein, perm-selective molecular imprinted polymers and gold nanorods are synthesized, characterized, and incorporated to better understand the effects of nanomaterial incorporation into a MIP biosensor. Unique Raman bands for caffeine, acetaminophen, aspirin, and non-imprinted polymer are identified. Shifts in these unique Raman vibrational modes are used to identify drug molecules that are bound to the MIP or free in solution. Next, drug templated MIPs are synthesized, extracted, and characterized using Raman spectroscopy. Interactions of nanorods with acetaminophen, aspirin, and caffeine templated MIPs are evaluated using extinction spectroscopy and Raman microscopy. Importantly, extinction spectroscopy and correlated SERS measurements are used to quantify the nanorod-drug interactions with and without molecular imprinted polymer. The magnitude of the SERS response correlates with the number of binding sites in the MIP and electrostatic and hydrogen bonding interactions between the MIP and nanorod. Finally, the nanorod concentration dependent vibrational shifts for acetaminophen, caffeine, and aspirin MIPs indicate that the drugs are partitioning into the CTAB bilayer or are very close to the MIP surface allow for simultaneous nanorod-drug interactions and as a result, SERS enhancements. Future studies could focus on exploiting the nanomaterial and MIP hydrophilic driven

interactions for increased SERS enhancements for complex sample analysis and for SERS-based MIP biosensor development.

5.2 Materials and Methods

Acetonitrile (C_2H_3N), 2-acrylamideo-2-methyl-1-propanesulfonic acid ($C_7H_{13}N_SO_4$), acetaminophen ($C_8H_9O_2N$), aspirin ($C_{11}H_{11}O_6$), azobisisobutylonitrile (AIBN), caffeine ($C_8H_{10}N_4O_2$), ethyl acetate ($C_3H_8O_2$), ethylene glycol dimethacrylate ($C_{10}H_{14}O_4$), glycidyl methacrylate ($C_7H_{10}O_3$), gold (III) chloride trihydrate ($HAuCl_4 \bullet 3H_2O$), 1-hydroxy-cyclohexyl-phenyl-ketone (Irgacure 184), 4-(2-hydroxyethyl)-1-piperazineethanesulfonic acid (HEPES), sodium nitrate ($AgNO_3$), sodium borohydride ($NaBH_4$), tetrahydrofuran (THF) (C_4H_8O), toluene (C_7H_8), and 3-trimethoxysilylpropyl acrylate ($C_8O_8H_{12}Si$) were purchased from Sigma-Aldrich (St. Louis, MO). Ascorbic acid and cetyl trimethylammonium bromide (CTAB) were purchased from Alfa-Aesar and Fluka, respectively. All other chemicals were purchased from Fisher Scientific (Pittsburgh, PA). Water (18.2 MΩ cm^{-1}) was obtained using a Nanopure System from Barnstead (Dubuque, IA).

5.2.1. Molecular Imprinted Polymer (MIP) Synthesis

Molecular imprinted polymers were prepared according to previous reports.[271,272] Briefly, caffeine imprinted MIPs ($MIP_{caffeine}$) were prepared by combining and equilibrating the following for 30 minutes: 20 mg caffeine, 30 µL methacrylic acid, 235 µL ethylene glycol dimethacrylate, 0.7 mg of the photo initiator Irgacure 184, 184 µL DMSO, and 551 µL THF. Aspirin templated methacrylate-based polymers ($MIP_{aspirin}$) were prepared by combining and equilibrating (30 minutes) 48 mg aspirin, 0.7 mg Irgacure, 30 µL methacrylic acid, 235 µL ethylene glycol dimethacrylate, and 735 µL THF. For both $MIP_{aspirin}$ and $MIP_{caffeine}$, polymerization of 1 mL aliquots occurred using an OmniCure Series 1500 ultraviolet lamp with a 250 - 450 nm filter (P = 15 mW) for 30 minutes.

Lyophilization of the polymer samples took place in a Thermo Scientific Modulyo Freeze Dryer for at least 24 hours. Acetaminophen imprinted MIPs ($MIP_{acetaminophen}$) were prepared by combining and equilibrating (30 minutes) 17 mg acetaminophen, 30 µL methacrylic acid, 235 µL ethylene glycol dimethacrylate, 5 mg AIBN, and 735 µL THF. Next, 1 mL aliquots were purged with N_2 and sealed with parafilm. The vials were placed in a 60 °C oven for 24 hours to cure. The resulting $MIP_{acetaminophen}$ were lyophilized for at least 24 hours to remove solvent.

Drug templates were removed from the MIP via Soxhlet extraction for 8 hours with dichloromethane, methanol, and ethyl acetate for caffeine, acetaminophen, and aspirin, respectively. To improve polymer uniformity, the MIPs were ground using a mortar and pestle and sieved (mesh size 707 – 230). The 0 – 63 µm fraction was collected and used for subsequent analysis and use.

5.2.2. Gold Nanorod Synthesis

Gold nanorods were prepared in a multi-step process in water.[108] First, gold seeds were prepared by adding 600 µL of 10 mM $NaBH_4$ to 9.75 mL of 100 mM CTAB (30 °C) and 250 µL of 10 mM $HAuCl_4$. After addition of $NaBH_4$, the gold seed solution was stirred for 2 minutes and allowed to age for 2 hours without stirring at 25 °C. Next, gold nanorods were synthesized by adding 75 µL of 0.01 M $AgNO_3$ to 9.75 mL of 100 mM CTAB. 10 mM $HAuCl_4$ (500 µL) and 150 µL of 1 M HNO_3 were then added to and pipette mixed with the solution. After ~15 seconds, 55 µL of 100 mM ascorbic acid was added and gently mixed with a pipette. As Au^+ ions formed, the solution became colorless. Finally, 12 µL of the synthesized seed solution was added to the solution to initiate nanorods growth, stirred gently, and incubated under stagnant conditions for 24 hours at 25 °C using a sand bath. The resulting nanorods were washed three times with 1 mM CTAB (7500 xg for 15 minutes) and stored until use. Immediately before using the

nanorod samples, aliquots were washed three times with 0.75 mM CTAB using centrifugation (7500 xg for 15 minutes).

5.2.3. Transmission Electron Microscopy (TEM)

The homogeneity and diameter of the polymer particles along with the aspect ratio of the gold nanorods were characterized using TEM (JEOL JEM-1230). The MIP particles were prepared by suspending 0.25 mg MIP in 50 % ethanol, pipetting 10 µL of the solution onto a carbon Formvar coated copper grid (400 mesh, Ted Pella, Redding, CA), and air drying overnight. The Au nanorod samples were prepared by pipetting 10 µL of a dilute nanorod sample (50% mixture in ethanol) onto a carbon Formvar coated copper grid (400 mesh, Ted Pella, Redding, CA), and allowing air drying to occur overnight. The resulting images were analyzed using Image Pro Analyzer, and at least 35 polymer particles and 100 nanorods were evaluated per sample to estimate particle dimensions.

The interaction of nanorods with the polymer particles was examined using TEM. The samples were prepared by adding 100 µL of 1.2 nM nanorods in 0.75 mM CTAB to drug-loaded polymer particles and incubating for 15 minutes. The supernatant was removed, the remaining ~10 µL if the MIP-nanorod complex was diluted (50% mixture in ethanol), pipetted onto a carbon Formvar coated copper grid, and dried overnight.

5.2.4. Dynamic Light Scattering (DLS)

Size analysis of hydrated fractionated MIPs was performed using dynamic light scattering (DLS) (Beckman Coulter DelsaNano C Particle Analyzer). The MIPs were prepared for DLS by suspending 1.74 mg of the dried MIP in 10 mM NaCl in water, sonicating for ~2 minutes, and incubating the samples at room temperature for 30 minutes prior to analysis. The resulting hydrated diameters were estimated assuming a Gaussian distribution.

5.2.5. Raman Microscopy

Raman spectra were collected using an Examiner532 Raman spectrometer (DeltaNu) mounted on an Olympus IX71 microscope equipped with a 10x objective lens and a Hamamatsu ORCA-ER camera Raman spectra were collected using the following parameters: excitation wavelength (λ_{ex}) = 532 nm, power (P) = 15 mW, integration time (t_{int}) = 3 – 15 seconds, and at least 30 averages. An Examiner785 Raman spectrometer (DeltaNu) (λ_{ex} = 785 nm, P = 70 mW, t_{int} = 60 seconds, and at least 10 averages) was also used. Raman intensities were collected in terms of photon counts (cts) but reported in units of $cts \cdot mW^{-1} \cdot s^{-1}$ to account for slight laser power variations. To determine vibrational peak intensities, the fluorescence background was removed using a moving baseline subtraction method (see Appendix 1). Next, spectral intensities were divided by the Raman intensity of the polymer C-C-O stretch at 600 cm^{-1} to account for sampling differences. Measurements were performed in triplicate, and error bars represent the standard deviation of these data.

5.2.6. Extinction Spectroscopy

Extinction spectra of Au nanorods containing samples were acquired using a UV-Visible spectrometer (Ocean Optics USB4000) configured in transmission geometry mounted on an Olympus IX71 microscope equipped with a 10x objective lens. Macroscale Au nanorod solution analysis took place using disposable glass vials (path length = 0.2 cm) using the following parameters: integration time = 20 ms, average = 10 scans, and boxcar = 10.

5.2.7 Molecular Imprinted Polymer SERS Assays

A 25 mM HEPES buffer (pH 8.5) was prepared from HEPES, and slight pH adjustments were made with 1 M NaOH. Note: All aspirin solutions were titrated with 1 M NaOH to prevent the formation of salicylic acid.[273] The ionic strength of acetaminophen and caffeine solutions was adjusted to 75 mM using NaCl. All solutions

were filtered using a 0.2 μm nylon filter (Whatman, Middelsex, UK) prior to use. For detection assays under equilibrium conditions, fractionated MIP samples were suspended in 0.9 mM drug solutions (2 mg/mL) and incubated for 8 hours. The excess drug solution was removed using a pipette and the MIP particles were suspended in 100 μL of 0, 0.6, 1.2, or 1.8 nM gold nanorod solution in 0.75 mM CTAB. The samples were incubated until the MIP particles settled to bottom of the vial (~15 min) at which time the supernatant was removed and the MIP and nanorod mixture was pipetted onto a glass slide and allowed to dry (30 minutes). The samples were then analyzed using both extinction spectroscopy and Raman microscopy.

5.3 Results and Discussion

5.3.1 Optical and Structural Characterization of Materials

Surface enhanced spectroscopic detection limits should depend on the plasmonic properties of the included plasmonic nanomaterials. Specifically, noble metal nanoparticles (copper, gold, silver, etc.) exhibit strong extinction properties in the visible and near-infrared regions of the electromagnetic spectrum,[174,274] which sensitively depend on nanoparticle shape, size, stability, and local dielectric constant.[265,275] These optical properties give rise to LSPR spectra which depend on the photon frequency of the incident electric field which causes the collective oscillation of the conduction band electrons on the nanoparticle surface.[66] Figure 5.1A shows the LSPR spectrum of gold (Au) nanorods fabricated using a silver-assisted seeded growth method.[108] The gold nanorods exhibit a transverse LSPR wavelength maximum ($\lambda_{max,T}$) at 513 nm and a longitudinal LSPR wavelength maximum ($\lambda_{max,L}$) at 719 nm. The extinction coefficient at the $\lambda_{max,L}$ is ~3.8×10^8 M^{-1} cm^{-1} as determined using previously established reports.[276] A representative TEM image of the Au nanorods is shown in Figure 5.1A (inset). Analysis of the TEM images reveals an average length, width, and aspect ratio of 56.7 ± 10.6 nm, 17.8 ± 4.1 nm, and 3.1 ± 0.6 nm, respectively (number of particles analyzed, n = 120). In

conjunction with molecular imprinted polymers, these gold nanorods form a nanosensor for drug molecules.

Molecular imprinted polymers for an over-the-counter migraine medication are fabricated to understand the effects of nanorod incorporation into MIP sensors. Standard methacrylate polymerization procedures employing methacrylic acid as the functional monomer and ethylene glycol dimethacrylate as the cross-linking monomer enables the production of acetaminophen ($MIP_{acetaminophen}$), aspirin ($MIP_{aspirin}$), and caffeine ($MIP_{caffeine}$) templated MIPs.[271] Following syntheses, the template molecules were removed using Soxhlet extraction, dried using lyophilization, ground with a mortar and pestle, and fractionated using a sieving stack (mesh size 707 – 230). In all subsequent studies, only the 0 – 63 μm fraction is used to improve polymer particle size homogeneity.

The resulting MIP samples are evaluated with TEM. Preparation of the MIP samples for TEM analysis requires suspending 0.25 mg of the polymer powder in 1 mL of 50% ethanol then spotting this solution on a TEM grid and allowing the sample to dry for 24 hours at room temperature before evaluation with TEM. Analysis of the resulting TEM images yields mean MIP particle dimensions of 421 ± 128 nm (number of particles (n) = 35), 345 ± 113 (n = 51), and 284 ± 117 (n = 35) for $MIP_{caffeine}$, $MIP_{acetaminophen}$, and $MIP_{aspirin}$ samples, respectively (Figure 5.1A, Inset). As expected, these average particle dimensions are within the collected fraction window, which indicates that grinding the polymer particles with a mortar and pestle followed by sieving, successfully yields fractionated polymer particles.

While TEM provides valuable details regarding non-hydrated particle morphology, DLS reveals hydrated particle diameters. For DLS measurements, ground polymer particles are suspended in 10 mM NaCl (1.74 mg polymer/mL NaCl), sonicated for 5 – 10 seconds, and incubated at room temperature for 30 minutes. Fitting the resulting DLS data with a Gaussian function facilitates the determination of the hydrated

diameters of these samples. Mean hydrated diameters are 740 ± 200, 760 ± 230, and 1140 ± 350 nm for $MIP_{caffeine}$, $MIP_{acetaminophen}$, and $MIP_{aspirin}$, respectively (data not shown). The differences in mean diameters observed between DLS and TEM are attributed to polymer swelling in aqueous environments and irregular particle morphologies. Importantly, both DLS and TEM indicate relatively monodisperse (RSD < 40%) fractionated polymer particle samples.

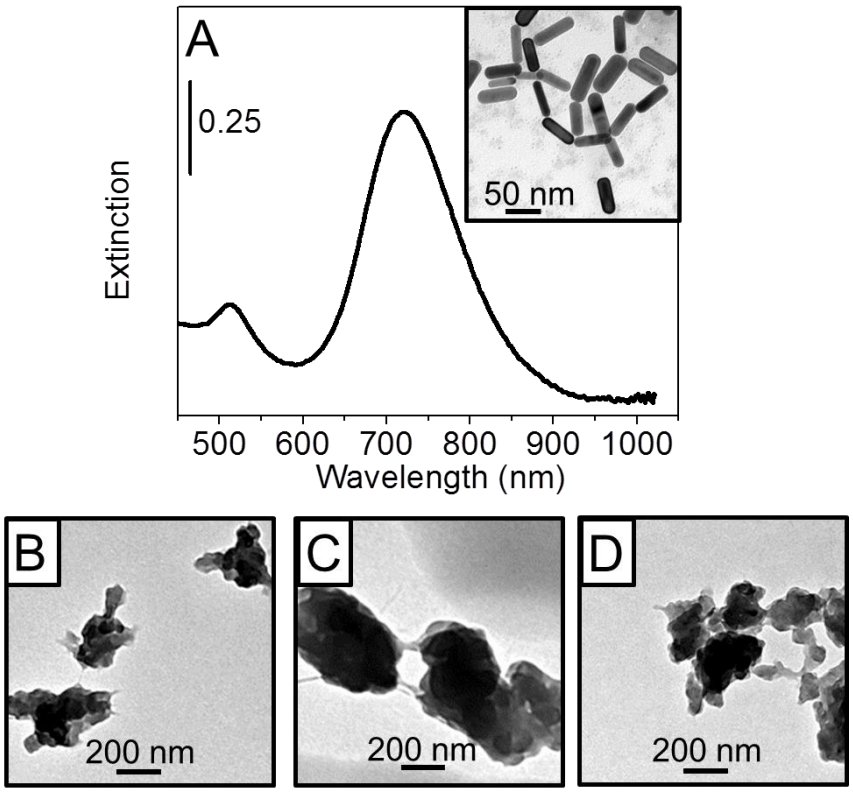

Figure 5.1. Characterization of nanorods and imprinted polymer particles. (A) Extinction spectrum of 1.2 nM Au nanorods in 0.75 mM CTAB where the longitudinal plasmon peak maxima ($\lambda_{max,L}$) = 719.0 nm. The inset shows a TEM image of Au nanorods where the length, width, and aspect ratio of the nanorods is 56.7 ± 10.6 nm, 17.8 ± 4.1 nm, and 3.1 ± 0.6 nm, respectively (number of particles analyzed (n) = 120). TEM images of (B) $MIP_{acetaminophen}$, (C) $MIP_{caffeine}$ (D) $MIP_{aspirin}$. The mean dimensions from TEM analysis are 421 ± 128 nm (n = 50), 345 ± 113 (n = 51), and 284 ± 117 (n = 35) for $MIP_{caffeine}$, $MIP_{acetaminophen}$, and $MIP_{aspirin}$, respectively.

5.3.2. Evaluation of Nanorod Incorporation with MIPs

The detection limit of drugs in previous MIP assays (See Chapter 4) was limited to mM concentrations whereas biologically relevant concentrations for small molecules can be as low as µM to nM concentrations.[277,278] To achieve these low detection limits, SERS is often used because molecular detection is improved by enhancing the magnitude of Raman scattering up to 9 orders of magnitude for a given analyte as a result of both chemical and electromagnetic enhancement effects.[270] As a result, the combination of nanomaterials with MIPs should improve the sensitivity of the MIP biosensors. The interactions of the nanorods with the drugs as well as with MIPs incubated with drugs are evaluated with extinction spectroscopy and Raman microscopy.

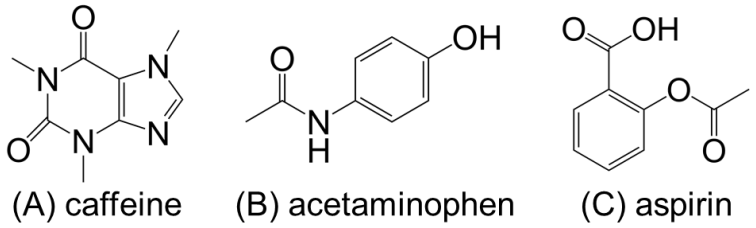

Figure 5.2. Structures of (A) caffeine, (B) acetaminophen, and (C) aspirin.

Previous studies of acetaminophen, caffeine, and aspirin (Figure 5.2) adsorbed onto a SERS active substrate (gold or silver) indicate that all three drugs can bind to the metal surface through the lone pairs of electrons on the carbonyl oxygen.[279,280] Acetaminophen and caffeine can also bind to the metal surface through electron lone pairs on nitrogen.[279,280] These effects are evaluated in Figure 5.3. For comparison, the optical properties of all samples are shown. First, the extinction spectra of 1.2 nM gold nanorods incubated overnight with and without 900 µM acetaminophen (Figure 5.3A1-2), caffeine (Figure 5.3B1-2), and aspirin (Figure 5.3C1-2) show that the gold nanorods

are electromagnetically stable in the presence of the drugs. Importantly, the chosen drug concentration (900 μM) falls below the Raman detection limits of the drugs in buffer, which means no observed peaks appear in normal Raman spectra (see Chapter 4).

LSPR spectral changes reveal several interesting nanoparticle-molecule interactions. Upon incubation with acetaminophen and caffeine, the gold nanorod longitudinal plasmon wavelength maximum blue-shifts by 3 and 4 nm, respectively. Additionally, the full width at half maximum (Γ) decreases from 0.28_2 eV to 0.28_0 and 0.27_9 eV for the nanorods incubated in acetaminophen and caffeine, respectively. This blue shift and slight narrowing of the plasmon band indicates that caffeine and acetaminophen are inserting between the carbon chains[281] of the CTAB promoting a less heterogeneous alignment of CTAB molecules on the gold nanorods surface. In contrast, the longitudinal plasmon wavelength for gold nanorods incubated with aspirin neither shifts nor broadens in the presence of aspirin. This indicates that the aspirin is not partitioning into or interacting with the CTAB bilayer structure. As a result, aspirin should not result in significant SERS enhancements (vide infra).

Electrostatic, hydrogen bonding, and Van der Waals, interactions are expected to drive the interactions between the MIPs and nanorods as well.[282-284] For MIPs and nanorods to interact, electrostatic potentials and hydrogen bonding between the two phases must be promoted. The slightly positive surface of the gold nanrods[285] and slightly negative polymer surface along with the high ionic strength of the buffer solution promotes these electrostatic interactions.[286] The interactions between the nanorods and polymer surface are further promoted via hydrogen bonds between the CTAB headgroup and carboxylic acid terminated polymer surface.[284,285] Once this takes place, drug molecules can partition into the hydrophobic tail region of the bilayer and undergo SERS enhancement. As such, these hypothesized interactions should increase as both of the head and tail group interactions are optimized. To initiate this process for SERS enhancement, gold nanorods should assemble at close packing distances on the MIP

surface. As a result, introduction of nanorods to MIP with and without drugs occurs in a multi-step process.

To achieve this, incubation of a known mass of MIP (2 mg polymer/mL) with 900 µM drug for a minimum of 8 hours allows for the saturation of drug binding sites in the MIPs for subsequent assays. MIP binding sites density per mg of polymer are 82.6 x 10^{18}, 33.9 x 10^{18}, 58.9 x 10^{18} for $MIP_{acetaminophen}$, $MIP_{caffeine}$, and $MIP_{aspirin}$, respectively (see Chapter 4). Consequently, all binding sites in the MIP should be saturated by drug molecules thereby inducing drug enrichment[241,287,288] in the MIPs prior to SERS detection. Following removal of the supernatant from the MIP-drug samples, Au nanorods (0 – 1.8 nM) were added and allowed to incubate for 15 minutes. Next, the composite sample is spotted onto a TEM grid or glass slide and dried. Samples evaluated with TEM reveal that nanorods interact with all three MIP samples (Figure 5.3). The polymer particle size slightly increases (from ~420 to ~540 nm for $MIP_{caffeine}$), which indicates that incomplete drying of the polymer occurred.

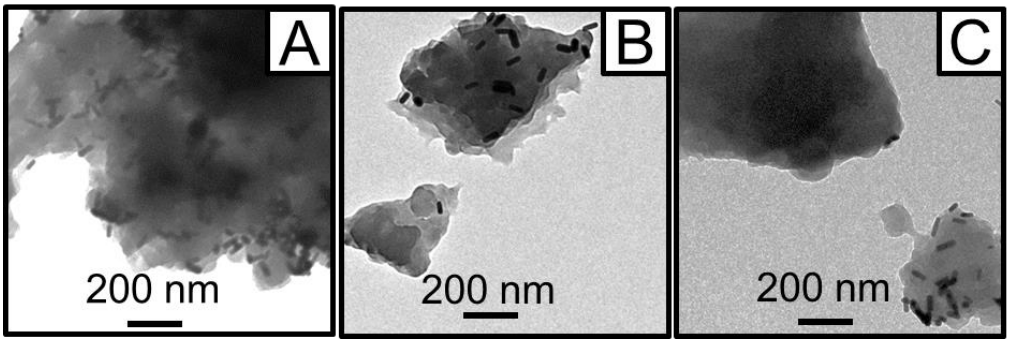

Figure 5.3. TEM of (A) $MIP_{acetaminophen}$, (B) $MIP_{caffeine}$, and (C) $MIP_{aspirin}$ after incubation in 1.2 nM nanorods.

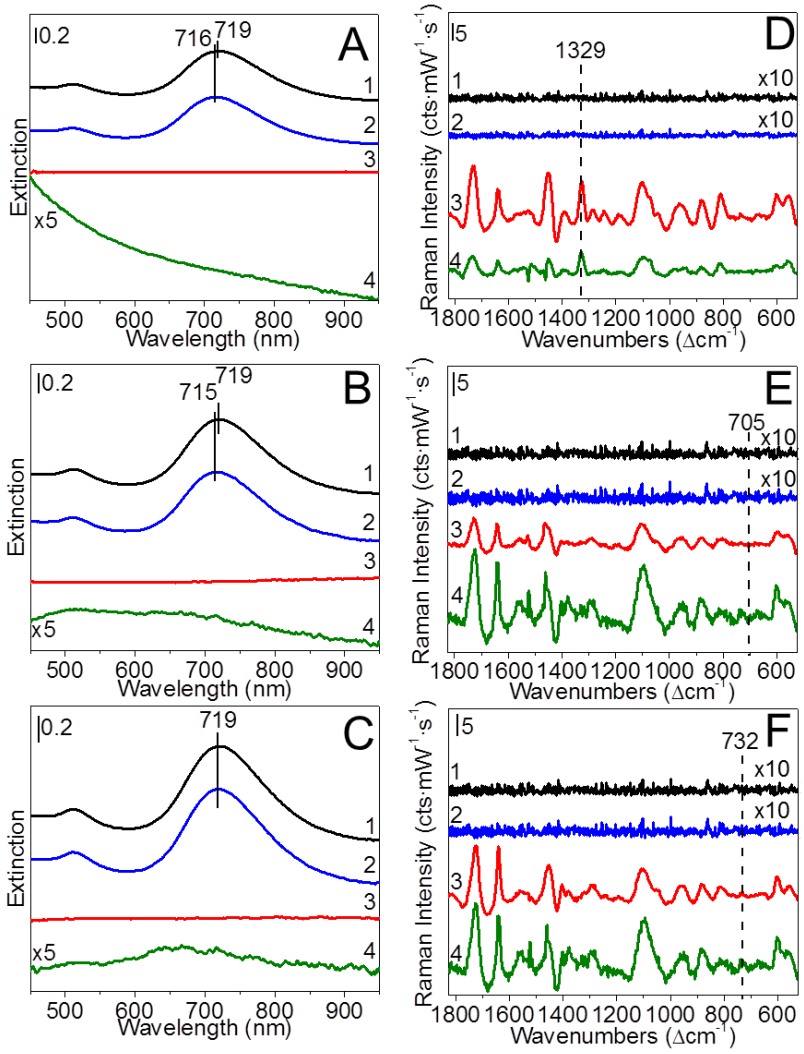

Figure 5.4. MIP sensors. (A-C) Representative extinction spectra for (1) 1.2 nM Au nanorods in 0.75 mM CTAB (in all panels), (2) 900 µM (A) acetaminophen, (B) caffeine, and (C) aspirin incubated with 1.2 nM Au nanorods (no MIP), (3) MIP, and (4) MIP and 1.2 nM Au nanorods. The longitudinal extinction maximum is labeled for the nanorod only spectra. The spectra are offset and spectrum (4) in each panel is multiplied by 5 for clarity. Representative Raman spectra of (1) 1.2 mM Au nanorods in 0.75 mM CTAB and 0.9 mM (D) acetaminophen, (E) caffeine, and (F) and aspirin incubated with (2) 1.2 nM Au nanorods (no MIP), (3) MIP, and (4) MIP and 1.2 nM Au nanorods. The unique Raman bands for caffeine (705 cm^{-1}, O=C-N deformation), acetaminophen (1329 cm^{-1}, phenyl OH stretch), and aspirin (750 cm^{-1}, O-H deformation) are labeled with a dotted line. The spectra are offset and spectra (1) and (2) are multiplied by 10 for clarity. Raman parameters: λ_{ex} = (1) and (2) 785 nm, (3) and (4) 532 nm; t_{int} = (1) and (2) 60 s, (3) and (4) 10 s; P = (1) and (2) 70 mW, (3) and (4) 15 mW.

Table 5.1. Unique vibrational band assignments for $MIP_{acetaminophen}$, $MIP_{aspirin}$, $MIP_{caffeine}$, and CTAB.

Raman Shift (cm^{-1})			Assignment	Molecule
$MIP_{Acetaminophen}$	$MIP_{caffeine}$	$MIP_{Aspirin}$		
1736	1726	1725	v(Carbonyl C=O)	Polymer
1640	1640	1640	v(C=C)	Polymer
1558	1558	1556	$v(CH_2)$	CTAB
1521	1527	1523	$w(CH_2)$	Polymer
	1462	1460	$\delta(CH_2)$	Polymer
1451	1447	1451	$\delta(CH_3)$	Polymer
	1402	1403	$d(CH_2)$	Polymer
1390	1379	1380	$d_a(CH_3)$	Polymer
1329			v(Phenyl OH)	Acetaminophen
1286	1290	1289	$(CH_2)_n$ twisting vibration	Polymer, CTAB
1243	1244		v(Ester)	Polymer
1149	1148	1149	CH_2 scissor mode	CTAB
1102	1102	1103	v(C-C)	CTAB
1074	1062		v(C-C Alkane)	CTAB
1044	1048	1049	$r(CH_3)$	Polymer
974	998	1004	$r(CH_3)$	Polymer, CTAB
960	957	956	$r(C(CH_3))$	Polymer
879	878	881	v(C-C-C (C-H))	Polymer
862	865	862	$d(CH_3)$	CTAB
811	804	810	v_s(C-C-C)	Polymer
		732	d(O-H), δ(C-H ring)	Aspirin
	705		δ(C-H out-of-plane)	Caffeine
559	599	601	v(C-C-O (methacrylate))	Polymer
558	568	555	$d(C_4N^+)$, $d(C\text{-}N\text{-}CH_3)$	CTAB, caffeine

Note: Abbreviations: δ= bending, d = deformation; ν = stretching, r = rocking, w = wagging, a = anti-symmetric, s = symmetric.

Next, the optical properties of the materials reveal how the composite materials are forming. Figure 5.4 shows correlated extinction and Raman spectra of dried drug-MIP particles after incubation with (spectrum 4 in each panel) and without 1.2 nM gold nanorods (spectrum 3 for each panel) for (Figures 5.4A and 5.4D) $MIP_{acetaminophen}$, (Figures 5.3B and 5.3E) $MIP_{caffeine}$, and (Figures 5.4C and 5.4F) $MIP_{aspirin}$. Corresponding control spectra which include spectra with nanorods only and nanorods with drug are shown in spectrum 1 and spectrum 2 of each panel, respectively.

Evaluation of the extinction spectra further reveal that the introduction of the molecular imprinted polymer to the CTAB headgroups on the nanorods causes the nanorods to assemble at short separation distances[289] on the surface of the MIPs as observed from the dampening of the LSPR spectra. Namely, broad and dampened spectral features arise in the LSPR spectra for each sample. Interestingly, gold nanorods incubated with $MIP_{caffeine}$ are most significantly dampened of the three samples while $MIP_{aspirin}$ samples are least impacted. This suggests that the surface of the caffeine-selective MIPs contain more carboxylic functional groups promoting more hydrogen bonding between the nanorod and MIP surface and thus promoting stronger attractive interaction between the gold nanorod than those between the other two MIPs. The opposite is observed for the aspirin-selective MIP. These spectroscopic results suggest that MIP-nanorod interactions can promote SERS detectability of caffeine and acetaminophen to a greater extent than for aspirin.

Differences in the SERS spectra for the various drugs further support this hypothesis. Recall that SERS signals for all drugs are not observed using nanorods alone. As a result, the MIP is expected to facilitate interactions between the nanorods and drugs, which could improve drug detectability. As shown in Figures 5.4D-5.4F (spectra 3 and 4 in each panel), spectral features for the polymer, CTAB, and drug are observed for each sample and are summarized in Table 5.1.[290,291] The presence of the unique drug vibrational bands in the samples incubated with MIPs indicates that the polymers are

acting as perm-selective materials for the drugs thereby facilitating drug enrichment in the MIPs.[292] Specifically, Raman bands at 1329 cm^{-1} (phenyl O-H stretch), 705 cm^{-1} (-CH=CH-), and 750 cm^{-1} (O-H deformation) are observed for acetaminophen (Figure 5.4D-3), caffeine (Figure 5.4E-3), and aspirin (Figure 5.4F-3) in the presence of corresponding MIP. To evaluate the impact of enrichment in the MIP samples without nanorods, all Raman signals are compared to the polymer C-C-O stretch at 600 cm^{-1}, which serves as an internal standard. Assuming drug enrichments as previously observed for these imprinted polymers (see Chapter 4), normalized Raman intensities of 1.26, 0.87, and 0.19 correspond to 20x, 18x, and 70x enrichments for $MIP_{acetaminophen}$, $MIP_{caffeine}$, and $MIP_{aspirin}$, respectively. These results are summarized in Figure 5.5.

Next, vibrational signal changes from the addition of nanorods are evaluated. Of note, the extinction properties of the nanorods-MIP samples vary from spot to spot on the glass substrate. This variability is attributed to uneven dispersion of the nanorod-MIP constructs in the sampling volume and is corrected for by assuming that the polymer signals are not enhanced significantly by the nanorods and comparing signals relative to the polymer band. In comparison to the enriched samples, larger SERS signals are observed for all samples (Figure 5.5) vs. samples that do not contain MIPs. These normalized SERS intensities range from 2.3, 0.9_8, and 0.3_0 for $MIP_{acetaminophen}$, $MIP_{caffeine}$, and $MIP_{aspirin}$, respectively.

These SERS signals are hypothesized to arise from drug molecules at binding sites in the MIP that are nearest to the nanorod surfaces.[293,294] Because the acetaminophen imprinted polymer contains ~2 and ~1.4 times the number of binding sites as the caffeine or aspirin imprinted polymer (82.6×10^{18} vs. 33.9×10^{18} or 58.9×10^{18} binding sites/g of polymer), larger signal increases are both expected and observed for acetaminophen vs. caffeine and aspirin. Binding site densities alone, however, do not explain the SERS responses observed for aspirin. We hypothesize that MIP particle swelling[236] upon incubation in buffer increases the distance between the binding sites and nanorods which

decreases the overall SERS signal. To better understand the hydrated size of MIP particles and understand these observations, the hydration layer thickness was determined by subtracting the dry polymer radius determined from TEM from the hydrated radius determined from DLS. This yields a hydration layer thickness of ~400 nm for $MIP_{aspirin}$ and ~200 nm for both $MIP_{acetaminophen}$ and $MIP_{caffeine}$. As a result, the small SERS signal observed for aspirin enriched in MIPs is limited by the increased distance between the polymer binding sites and the enhancing nanorod substrates (in comparison to acetaminophen and caffeine). These findings suggest that the number of binding sites and polymer swelling must be considered to promote large SERS signals.

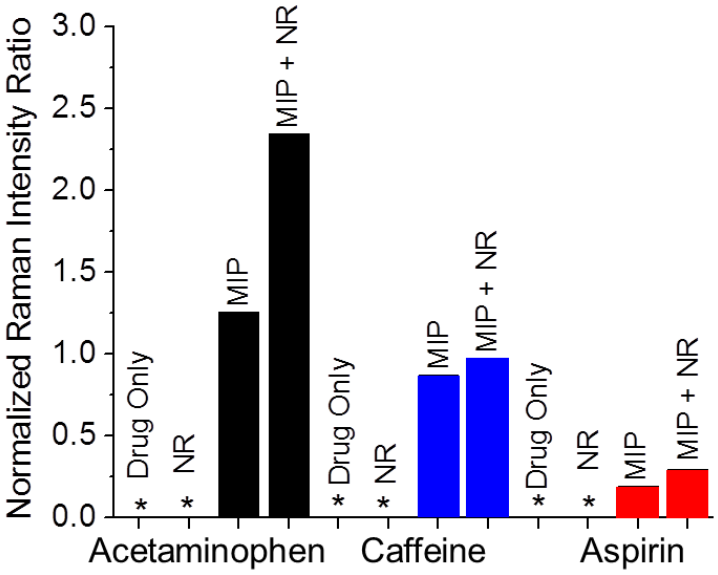

Figure 5.5. SERS enhancements for the three drugs in the presences of MIP and 1.2 nM gold nanorods. Normalized Raman intensity ratio for acetaminophen (black bars), caffeine (blue bars), and aspirin (red bars) for 0.9 mM drug only, 1.2 nM nanorods only (NR), molecular imprinted polymer loaded with drug (MIP), and molecular imprinted polymer loaded with drug and incubated with 1.2 nM nanorods (MIP + NR). "*" indicates no signal was observed.

5.3.3. Correlating LSPR and SERS Measurements of MIP Sensors

As discussed previously, SERS enhancements depend on the electrostatic and hydrogen bonding interactions between the drug and MIP as well as the nanorods and MIP. In an effort to maximize nanorod-MIP interactions, the concentration of nanorods is varied from 0 to 1.8 nM. As in previous studies, 2 mg of MIP is pre-equilibrated with 900 μM drug for 4 hours. Next, both LSPR (Figures 5.6A-5.6C) and SERS (Figures 5.6D-5.6F) spectra are collected and compared for the three drugs. As expected, the plasmonic features of the nanorods become more visible as nanorod concentration increases from 0 to 1.2 to 1.8 nM for all samples. The slight variations in the LSPR features among the three MIP samples are attributed to differences in induced electrostatic and hydrogen bonding interactions between the MIPs and nanorods samples. Once again, the large hydration layer thickness for $MIP_{aspirin}$ limits the short-range interactions between aspirin binding sites and the SERS-active nanorods. As a result, the extinction properties of this nanorod-modified sample are more similar to nanorods free in solution vs. nanorods bound to either $MIP_{acetaminophen}$ or $MIP_{caffeine}$.

To evaluate the mechanism of signal changes in the corresponding SERS spectra for the samples (Figures 5.6D-5.6F), both vibration energies and peak widths can be monitored.[295-299] Hydrogen bonding interactions between the CTAB head groups on the gold nanorod or MIPs/drugs can influence the relevant vibrational force constant associated with the interacting functional groups. For example, out-of-plane bends or deformations result in an increased force constant of that vibration which will cause those Raman frequencies to blue-shift.[280] In-plane stretches, however, will red-shift as the effective bond lengths of these will increase from electron donation from the drug to the metal.[279]

All of these frequency changes are observed in Figures 5.6D-5.6E. SERS spectra for $MIP_{caffeine}$, $MIP_{acetaminophen}$, and $MIP_{aspirin}$ incubated with (spectrum 1) 0, (spectrum 2)

1.2, and (spectrum 3) 1.8 nM nanoparticles are shown in this figure. For instance, the unique vibrational band for $MIP_{caffeine}$, blue-shifts from 703 cm^{-1} to 705 cm^{-1} (C-H out of plane bend) in the presence of nanorods (Figure 5.6D). Importantly, this 2 cm^{-1} *blue*-shift indicates that caffeine is near the metal surface and either partitioning into the CTAB layer on the gold nanorods or bound to a MIP binding site. The unique Raman band for acetaminophen, however, (Figure 5.6E) *red*-shifts by 2 cm^{-1} to 1327 cm^{-1} from 1329 cm^{-1} (phenyl stretch) in the presence of nanorods, which indicates (1) more direct interactions with the metal surface and (2) acetaminophen is likely partitioning into the CTAB bilayer on the surface of the gold nanorods. As observed previously, little change is observed for aspirin (Figure 5.6F). The lack of vibrational frequency changes in the aspirin vibrational modes likely arise from the limited interactions between the MIP particles and nanorods. As a result, MIP-nanorod interactions are shown to play an important role in either promoting or prohibiting SERS signals of small molecules. Future studies could focus on exploiting this behavior for complex sample analysis.

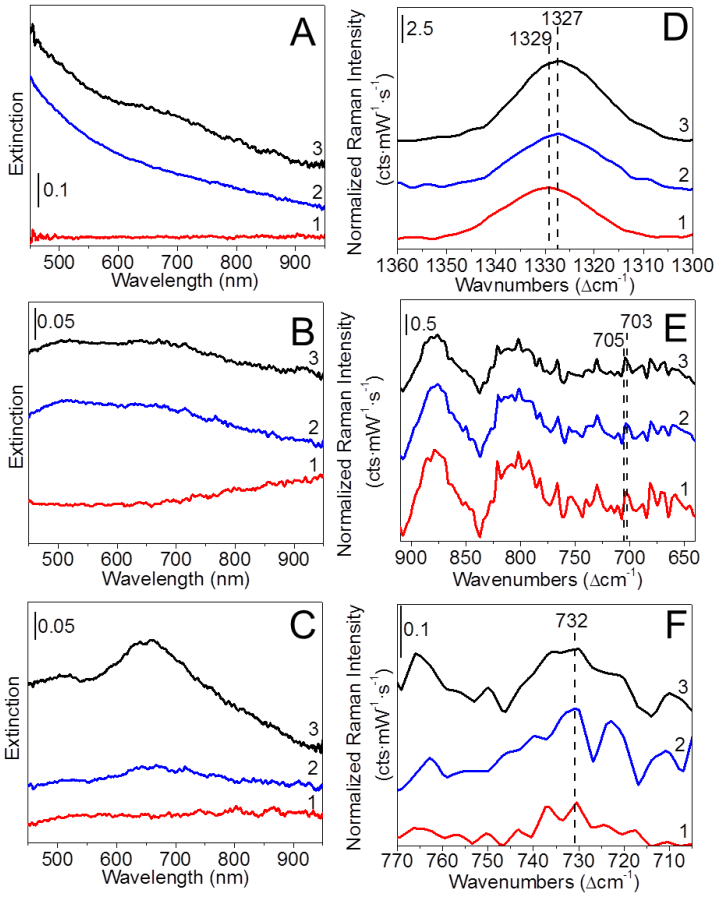

Figure 5.6. Extinction spectra of (A) $MIP_{acetaminophen}$ treated with 0.9 mM acetaminophen, (B) $MIP_{caffeine}$ treated with 0.9 mM caffeine, and (C) $MIP_{aspirin}$ treated with 0.9 mM aspirin and incubated with (1) 0, (2) 1.2, and (3) 1.8 nM Au nanorods. (D) Normalized Raman spectra of $MIP_{acetaminophen}$ treated with 0.9 mM acetaminophen and incubated with (1) 0, (2) 1.2, and (3) 1.8 nM Au nanorods. The acetaminophen Raman bands at 1329 cm^{-1} and 1327 cm^{-1} (phenyl OH stretch) are labeled with a dotted line. (E) Normalized Raman spectra of $MIP_{caffeine}$ treated with 0.9 mM caffeine and incubated with (1) 0, (2) 1.2, and (3) 1.8 nM Au nanorods. The caffeine Raman bands at 705 cm^{-1} and 703 cm^{-1} (O=C-N deformation) is labeled with a dotted line. (F) Normalized Raman spectra of $MIP_{aspirin}$ treated with 0.9 mM aspirin and incubated with (1) 0, (2) 1.2, and (3) 1.8 nM Au nanorods. The aspirin Raman band at 750 cm^{-1} (O-H deformation) is labeled with a dotted line. All spectra were normalized to the polymer band at 600 cm^{-1} (C-C-O stretch) to account for sampling differences. Raman parameters: λ_{ex} = 532 nm, t_{int} = 8 – 15 seconds, P = 15 mW.

5.4. Conclusions

Small molecule detection using MIP nanosensors depends on the plasmonic properties of the gold nanorod SERS substrate and surface chemistry, binding and swelling characteristics of the MIP, and surface charge differences on the MIPs vs. nanomaterials. Interactions of nanorods with acetaminophen, aspirin, and caffeine templated MIPs were evaluated using extinction spectroscopy and Raman microscopy. First, gold nanorods and MIPs were synthesized, and the optical and structural properties were evaluated. Second, LSPR changes upon drug incubation with gold nanorods revealed blue shifts and plasmon narrowing in the presence of acetaminophen and caffeine indicating drug interactions with the metal nanoparticle surface. No LSPR changes were observed upon aspirin nanorod incubation because of limited driving forces for interaction (osmotic and electrostatic). Introduction of nanorods to drug-saturated molecular imprinted polymers induced electrostatic and hydrogen bond driven nanorod aggregation on the MIP surfaces for all three drugs and exhibited correlated SERS responses. The magnitudes of the SERS responses were found to correlate with the number of binding sites and hydration layer thickness of the MIP. Moreover, nanoparticle concentration dependent vibrational shifts for caffeine and acetaminophen MIPs indicated that the drugs are partitioning into the CTAB bilayer or are very close to the MIP surface still allowing for nanorod-drug interactions. Importantly, MIP-nanorod interactions can either promote or prohibit SERS detection of small molecules. Future studies could focus on exploiting this behavior for complex sample analysis and for SERS-based MIP biosensor development.

CHAPTER 6 CONCLUSIONS AND FUTURE DIRECTIONS

6.1 Conclusions

The work presented in this thesis consists of the synthesis, functionalization, and characterization of noble metal nanoparticles as well as the synthesis of drug-specific molecular imprinted polymers (MIP) which are used for the Raman and SERS-based detection of small molecules. The methods used and the results published from these studies can be applied to future work toward understanding and facilitating the integration of nanomaterials into MIP devices for biological and environmental sensor construction.

Chapter 1 reviewed the use of affinity nanosensors using both naturally occurring recognition elements, such as antibodies and DNA, and explored plastic antibodies as an alternative recognition element for qualitative and quantitative detection of small molecules. Examination of naturally occurring recognition elements for optical nanosensors included aggregation-based immunoassays, plasmonic biosensors, and surface-enhanced Raman biosensors (SERS). Naturally occurring recognition elements exhibit well understood binding behavior thereby facilitating utilization in biosensors but are limited in scope because of the tendency of these materials to denature in as a function of pH, ionic strength, and/or concentration. In contrast, plastic antibodies provide more environmental stability in these same varying solution conditions without losing recognition capabilities. Incorporation of plastic antibodies into nanosensors with fluorescence, electrochemical, surface plasmon resonance (SPR), and SERS detection facilitated the development of MIP sensors and allowed for quantitative detection of a variety of molecules with selectivities at or near that of naturally occurring recognition elements.

To improve detection sensitivity in biological and environmental sensors, nanomaterials are often used, and reproducible quantification of small molecules is

improved when homogeneous nanoparticles are used. As a result, the effects of varying citrate concentration during gold nanoparticle growth and the resulting nanomaterial homogeneity were examined in Chapter 2. Citrate was utilized to stabilize the nanoparticles during growth but also impacted the overall ionic strength and solution pH. An increase in citrate concentrations was found to initially decrease the formation of rod-like nanomaterials. No rod-like structures formed when citrate concentrations ranged from 0.70 – 1.10 mM; however, the localized surface plasmon resonance (LSPR) band of these samples dampened with increasing citrate concentration suggesting that the number of internal and/or external atomic defects increased. Time-dependent flocculation studies indicated that the materials with the most dampened LSPR properties were the most unstable nanoparticles (i.e., aggregated most readily) which further supported the hypothesis that increasing atomic defects in the gold nanomaterials with increasing citrate (via the formation of a short yet non-diffuse double layer) influenced nanoparticle function in subsequent studies.

Next, the surface chemistry of nanoparticles must be considered prior to integrating nanomaterials in sensors. As a result, the characterization and optimization of gold nanoparticles with controlled surface chemistry was described in Chapter 3. Specifically, the chapter focused on the synthesis and characterization of thioctic acid functionalized gold nanoparticles. In summary, gold nanoparticles functionalized with thioctic acid were prepared with the slow addition of NaCl. TEM, ^{1}H NMR, extinction spectroscopy, zeta potential, XPS, and flocculation studies revealed that the self-assembly of thioctic acid on gold nanoparticles increases with increasing NaCl concentration.

An increase in NaCl concentration decreased the Debye length surrounding the deprotonated carboxylate groups on the assembled thioctic acid molecules thereby facilitating increased SAM packing densities. Furthermore, the slow addition of NaCl to gold nanoparticles during thioctic acid self-assembly increased subsequent functionalized

nanoparticle stability vs. controls as determined from flocculation studies. These results are expected to improve strategies for reproducible SAM formation on solution-phase nanostructures. Further studies could be expanded to investigate how nanoparticle shape, size, and radius of curvature impact this self-assembly process for ultimate improvements in the reproducible synthesis and use of nanomaterials in a variety of applications including those where MIPs are utilized.

Chapter 4 examines the development and spectroscopic characterization of MIPs for biomolecule detection in complex matrixes. Specifically, perm-selective MIPs were synthesized to quantitatively detect acetaminophen, aspirin, or caffeine in a complex matrix. While MIP selectivity was modest yet consistent with previous investigations, detection of the unique Raman band of the target drug molecules allowed for drug identification within a complex sample. As a result, MIP recognition agents in conjunction with Raman microscopy provided a rapid and direct method of quantitative and qualitative detection of drug samples.

Gold nanomaterials and MIPs are combined for the enhanced detection of drugs as described in Chapter 5. Incorporation of nanomaterials into a MIP biosensor for SERS detection was investigated by incubating MIPs with acetaminophen, aspirin, and caffeine to enrich samples. Next, these materials were equilibrated with gold nanorods to enhanced detection sensitivity using SERS. Impacts of gold nanorods concentration were evaluated and the optical properties of these nanomaterials were used to explain the observed enhancements. Future improvements to nanoparticle surface chemistry and MIP binding pocket density to drug concentration are expected to improve the limits of detection and the dynamic range for MIP biosensors.

6.2 Future Directions

In closing, nanomaterial incorporation into MIP biosensors will likely expand because of resulting improvements in the understanding of the ion double layer composition and thickness on the growth of gold nanoparticle structure as well as the subsequent surface functionalization along with the combination of the molecular fingerprint capabilities using Raman spectroscopy and decreased detection limits achieved using surface-enhanced Raman scattering. Application to real-world relevant biological systems such as a complex sample containing Vitamin D metabolites (see Appendix 2 for preliminary data) requires sensitive and specific real-time detection in complex matrices.

The optimized synthesis of MIP and fabrication of MIP biosensor devices with real-time and sensitive quantification of target analyte will be crucial for overcoming the challenges faced by biosensors with novel recognition agents. Improvements to MIP specificity could be realized with the implementation of covalently synthesized polymers that rely on covalent bonds for binding with the template rather than hydrogen bonding utilized in this thesis. MIP particle syntheses that yield homogeneous polymer particles directly is expected to decrease the non-specific binding in the biosensor by removing the partially broken template sites generated by grinding bulk polymers. Furthermore, the use of flow-through devices with increased flow capabilities (~100 μL min^{-1}) are expected to allow for real-time detection by promoting biomolecule diffusion into the binding site. All in all, the incorporation of noble metal nanomaterials into MIP biosensors will continue to improve analyte sensitivity and as a result, applicability of nanomaterial biosensor detection methods. Regardless of the signal transduction method or nanomaterial used; plastic antibody design, incorporation, and synthesis will continue to drive real-world applications of MIP sensors for biological and environmental sample analysis.

APPENDIX A BASELINE SUBTRACTION OF RAMAN SPECTRA USING AN EXCEL PROTOCOL

The following Excel protocol generates a baseline for a given Raman spectrum and then subtracts that baseline from the original Raman spectral intensity data to provide a baseline subtracted Raman spectrum in a reproducible, non-biased, and rapid manner. This appendix serves as a resource for members of the Haes research group in adopting this method into their data analysis.

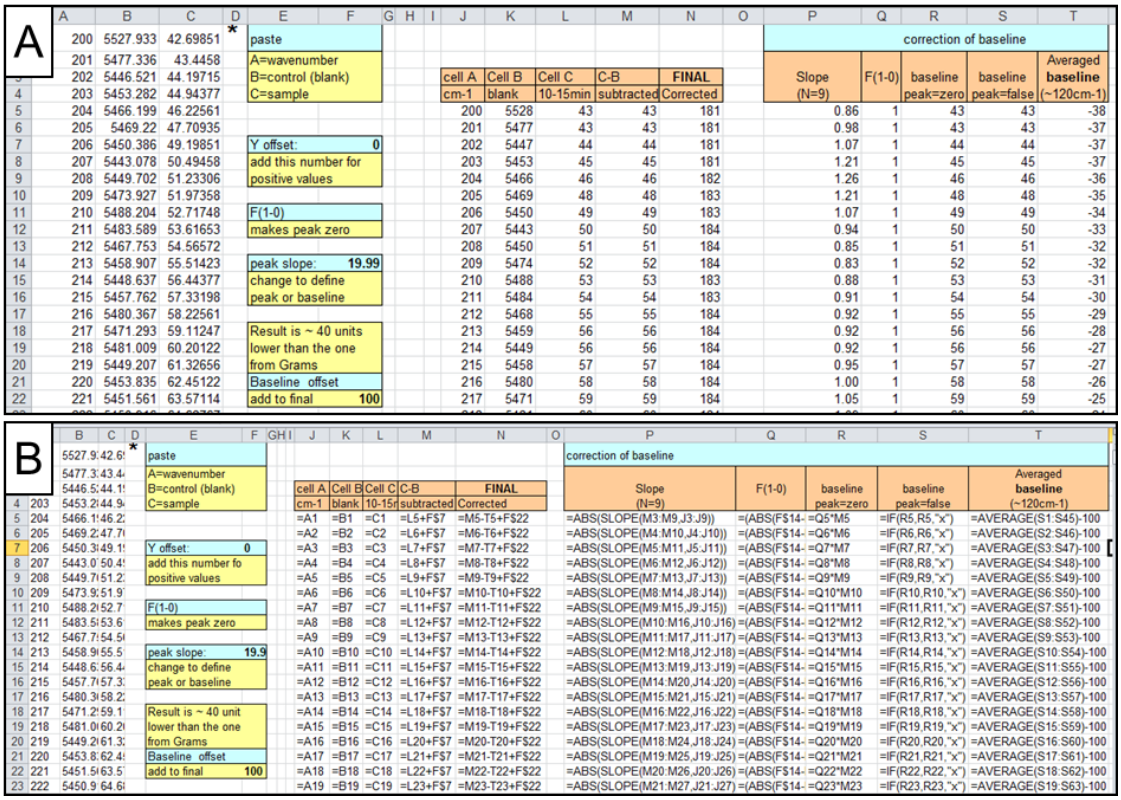

Figure A.1. Screen shot of example Raman data file treatment using the Excel protocol (A) without and (B) with formulas shown.

A.1 Overview of Approach.

The following approach generates baseline-subtracted Raman spectra with the aid of simple functions found in Excel. Figure A.1 shows an example Excel protocol for Raman data analysis (A) without and (B) with formulas shown. The vibrational wavenumbers, raw Raman intensity, calculated slope, baseline, and baseline subtracted spectrum are located in columns A, C, P, T, and N, respectively. Specifically, the protocol operates by estimating the slope (=SLOPE(known y, known x), shown in column P) over a moving yet discrete wavenumber range (9 cm^{-1} in this example) to determine if a peak is present. As shown in Figure A.1, the slope for a peak is set at 19.99 for this example protocol (Cell F14). If the slope in any spectral window exceeds this calculated value (for instance, in the presence of a vibrational band), no baseline subtraction takes place. When the slope is less than the value in Cell F14, a vibrational band is likely not present and these data likely represent background counts. As a result, an average baseline at the center wavenumber is generated by averaging the Raman count data over a 121 raw data point range (60 points on each side of the center point). This procedure continues throughout the entire spectral range.

For reference, a plot of the raw Raman spectrum, estimated baseline, and baseline subtracted Raman spectrum are shown in Figure A2. Plotting the (Figure A.2-1) uncorrected Raman spectrum, (Figure A.2-2) generated baseline, and (Figure A.2-3) resulting baseline subtracted Raman spectrum illustrates a successful example for data treatment using the Excel protocol for an arbitrary data file. Note that the broad continuum often observed in Raman spectra is observed in the raw data file and well-represented by the generated baseline file. The resulting “corrected” Raman spectrum contains vibrational features associated with the original sample (minus the background continuum).

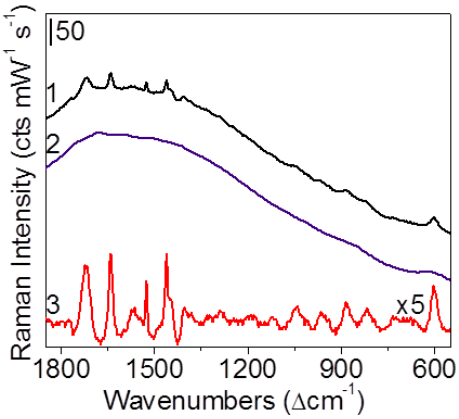

Figure A.2. Representative Raman spectra of (1) a raw data file, (2) Excel generated baseline from the raw data file, and (3) the resulting baseline subtracted Raman spectrum. The spectra are offset, and the subtracted spectrum is multiplied by 5 for clarity.

A.2 How to Apply this Protocol to Your Data.

To use this baseline subtraction protocol, first paste the Raman intensity data (typically in counts or counts/mW/s) along with the shifted wavenumber data associated with the raw data into columns C and A, respectively. The protocol can also be modified to subtract a blank spectrum from the raw data by pasting the Raman intensity data associated with raw blank data into Column B. Additionally, column M (see Figure A.1) contains blank corrected data which can also be background corrected (raw-blank).

Next, the peak slope threshold (value in cell F14) and baseline window must be optimized by increasing or decreasing the preset number for the slope of the peak (cell F14) and/or the number of data points averaged (Column T) to generate a meaningful baseline. For example, Figure A.3A illustrates a baseline subtracted Raman spectrum with the preset slope threshold in cell F14 set to (1) 1 (too low) or (2) 50 (too high). A false peak arises at ~1775 cm^{-1} (Figure A.3-A1) when the preset slope threshold is too low. This peak disappears at larger preset slope thresholds (for instance, 50, Figure A3-A2). Importantly, an optimized preset slope threshold will not generate artificial peaks in processed Raman spectra. After optimization of all values, the background subtracted

spectrum can then be copied from column N and pasted into another document for further use.

A.3 Warning: Optimizing the Number of Averages Easily Generates False Spectral Features.

The parameter most difficult to troubleshoot is the number of data points to average when generating a baseline (Column T). For example, Figure A.3-B shows a baseline-corrected Raman spectrum generated using (1) 401, (2) 121, or (3) 7 averaged data points which is changed in column T. When the number of averaged data points spans a window that is too large for accurate baseline estimation, artificial peaks and an uneven baseline result (Figure A.3-B1). Alternatively, a window that is too small for baseline estimation results in the over-subtraction of peaks from the original Raman spectrum (Figure A.3-B3). An optimized baseline maximizes the identification of "real" vibrational modes and minimizes the generation of false vibrational features observed in processed Raman spectra (Figure A.3-B2). Of note, once the Excel protocol for a given molecule is determined, no further optimization in terms of preset slope threshold and averaging window are required.

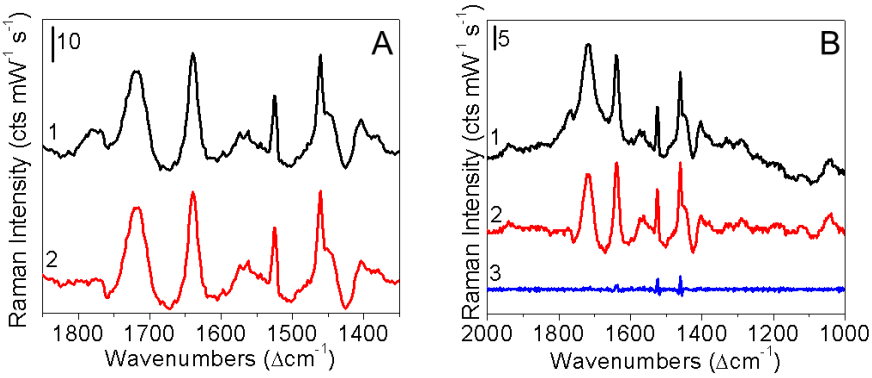

Figure A.3. Representative baseline subtracted Raman spectra after changing the (A) slope threshold to (1) 1 and (2) 50 and (B) number of data points averaged to (1) 401, (2) 121, and (3) 7.

APPENDIX B TOWARDS MOLECULAR IMPRINTED POLYMERS NANOSENSORS FOR QUANTITATIVE VITAMIN D METABOLITE DETECTION

B.1 Introduction

Vitamin D deficiency is a suspected clinical indicator of poor health and several diseases including but not limited to asthma, cardiovascular disease, cancer, and cystic fibrosis.[300-302] The many biologically relevant forms or metabolites of Vitamin D such as 7-dehydrocholesterol, calcifediol (25-hydroxyvitamin D), and calcitriol (1,25-dihydroxyvitamin D) (structures shown in Figure B.1) increase the difficulty of fully understanding the role Vitamin D deficiency plays in human health and disease. Because Vitamin D transformation is influenced by UV light, understanding mechanistic impacts from the environment or body are difficult to separate. Specifically, the UV light-induced ring opening of the pro-vitamin form of Vitamin D (7-dehydrocholeserol) results in Vitamin D. Vitamin D is then further hydroxylated to form calcifediol and subsequently calcitriol.[301]

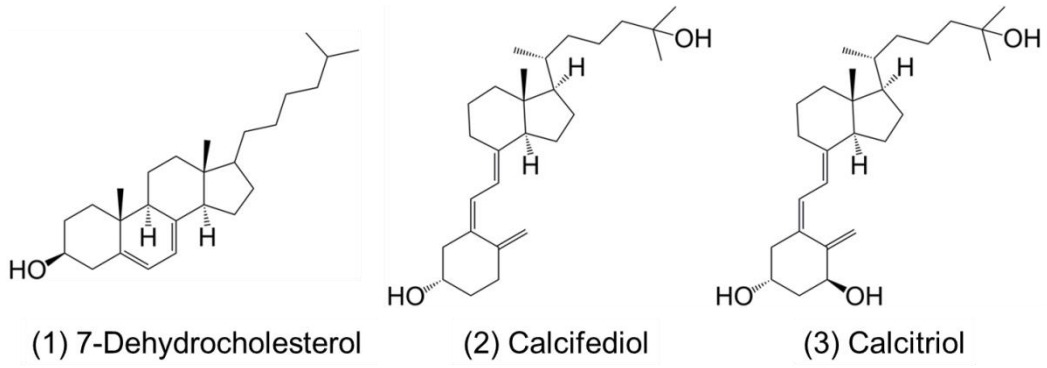

Figure B.1. Structures of (1) 7-dehydrocholesterol, (2) calcifediol, and (3) calcitriol.

Because of the possible clinical significance of Vitamin D in several diseases, there are several commercially available kits for calcitriol or calcifediol.[303] Assays to quantitatively detect Vitamin D metabolites typically use gas or liquid chromatography as well as immunoassays.[301] Several problems exist in these standard detection schemes or kits. First, the detection limits resulting from these typically do not approach clinically relevant concentrations (sub-50 nM).[300] Second, metabolites must be derivatized prior to analysis with chromatographic methods.[301] Third, commercially available kits require long incubation times (30 minutes – overnight), exhibit poor reproducibility between users and/or labs, and possess short shelf lives because of the instability of the reagents (i.e., antibodies) employed.[303] Finally, both precursors and metabolites cannot be detected simultaneously with commercially available kits or chromatographic methods. As a result, whether or not Vitamin D directly or indirectly impacts disease and poor health is unknown and highly debated.[304] This question could be addressed by developing a new method that gives rise to simultaneous and quantitative analysis of these precursors and metabolites thereby allowing for a better understanding of the relationship between Vitamin D metabolism and human health.

Herein, preliminary progress toward developing a novel Vitamin D metabolite sensor platform is discussed. First, a standard immunoassay method is evaluated to assess the current state of the art capabilities for Vitamin D detection. Next, Raman spectra of Vitamin D metabolites are collected and characterized. Finally, the syntheses of molecular imprinted polymers (MIPs) that recognize cholesterol are synthesized, extracted, and characterized using Raman microscopy. Cholesterol which exhibits similar chemical and physical properties as Vitamin D metabolites is selected for these preliminary studies. Importantly, development of a MIP nanobiosenor for Vitamin D detection will significantly assist in addressing current biomedical detection limitations and subsequently, will impact how diseases are diagnosed (see Chapter 5). Furthermore, the narrow, unique vibrational features observed with Raman spectroscopy and simplified

using MIP recognition elements along with enhanced detection capabilities should make this approach an ideal detection and recognition platform for bioassays, in general, and analysis of complex Vitamin D precursors and metabolites possible.

B.2 Materials and Methods

Cholesterol ($C_{27}H_{46}O$), 7-dehydrocholesterol ($C_{27}H_{44}O$), ethylene glycol dimethacrylate ($C_{10}H_{14}O_4$), 1-hydroxy-cyclohexyl-phenyl-ketone (Irgacure 184), methacrylic acid ($C_4H_6O_2$), and tetrahydrofuran (THF) (C_4H_8O) were purchased from Sigma-Aldrich (St. Louis, MO). Calcifediol ($C_{27}H_{44}O_2$) was purchased from VWR (Radnor, PA). Calcitriol ($C_{27}H_{44}O_3$) was purchased from Fisher Scientific (Pittsburgh, PA). Chemicals were used as received. Water (18.2 MΩ cm^{-1}) was obtained using a Nanopure System from Barnstead (Dubuque, IA).

B.2.1 MIP Synthesis

Molecular imprinted polymers were prepared according to previous reports.[34,218] Briefly, cholesterol imprinted MIPs ($MIP_{cholesterol}$) were prepared by combining and equilibrating the following for 30 minutes: 39 - 77 mg cholesterol, 60 µL methacrylic acid, 470 µL ethylene glycol dimethacrylate, 1.41 mg of the photo initiator Irgacure 184, and 1470 µL THF. Polymerization of 1 mL aliquots occurred using an OmniCure Series 1500 ultraviolet lamp with a 250 - 450 nm filter (P = 15 mW) for 2 hours. The resulting MIPs were dried overnight at room temperature and then at 90 °C for 24 hours. A non-imprinted polymer was prepared using the same conditions except no cholesterol was used. Cholesterol templates were removed from the MIP via extraction for 80 hours with 95% ethanol. The ethanol was replaced with fresh ethanol every 20 hours to maximize extraction efficiency.

B.2.2 Raman Microscopy

All Raman spectra were collected using either an Examiner532 Raman spectrometer (DeltaNu) with the following parameters: excitation wavelength (λ_{ex}) = 532 nm, power (P) = 1.9 or 49 mW, integration time (t_{int}) = 1 – 30 seconds, and at least 5 averages or an Examiner785 Raman spectrometer (DeltaNu) which was mounted on an Olympus BX51 microscope equipped with a 10x objective lens (λ_{ex} = 785 nm, P = 59 mW, t_{int} = 60 seconds, and at least 5 averages). In both cases, an Olympus QColor camera was used to visualize the samples. Raman intensities were collected in terms of photon counts (cts) but were reported in units of $cts \cdot mW^{-1} \cdot s^{-1}$ to account for slight laser power variations and utilized integration times. The fluorescence background was removed by applying a point-by-point baseline with Grams AI to determine vibrational peak intensities.

$MIP_{cholesterol}$ analysis was performed by analyzing spectral intensities for the vibrational modes in a sample and dividing those values by the Raman intensity of the polymer C-C-O stretch at 600 cm^{-1} to account for sampling differences. Measurements were performed in triplicate, and error bars represent the standard deviation of these data.

B.2.3 Calcitriol Enzyme Immunoassay (EIA)

An EIA kit for the quantitative determination of calcitriol (Vitamin D metabolite) was purchased from Immunodiagnostic Systems Inc. (Fountain Hills, AZ) and used according to the included instructions (Figure B.2). This EIA assumes that the measured calcitriol concentration equals the total Vitamin D concentration in the sample. To use this assay, a multistep process involving the generation of a calibration curve is required. Briefly, 100 µL of the included six calibration standards (0 – 544 pM calcitriol) were added to 100 µL of a primary antibody solution (anti-calcitriol) and allowed to incubate at 2 – 8 °C overnight. After this 12 hour incubation window, 150 µL of these solutions (now containing calcitrol-antibody complexes) were pipetted into the appropriate wells of a

secondary antibody coated well plate (leaving two wells empty for the blank), sealed, and shaken (500 – 750 RPM) for 90 minutes at room temperature. Next, 100 µL of biotin functionalized calcitriol was added to each well (including two "blank" wells) and shook for an additional 60 minutes. The well plate was thoroughly washed three times with a proprietary rinsing buffer, and 200 µL of an enzyme conjugate solution was added to each well which was then incubated for 30 minutes thereby allowing for a reaction to occur between the enzyme conjugate and the biotin labeled calcitriol. After washing the well plates three times with the rinsing buffer, 200 µL of a proprietary chromophore solution was added to all of the wells (including the blanks) and incubated for 30 minutes. Finally, 100 µL of 0.5 M HCl were added to each well in the well plate, and the absorbance at 450 nm was measured using a plate reader.

A calibration curve of calcitriol concentration was constructed by plotting the normalized percent binding (B/B_o%) as a function of calcitriol concentration using the following equation:

$$\frac{B}{B_o}\% = \frac{(\text{mean absorbance - mean absorbance of substrate blank})}{(\text{mean absorbance for 0 pM calibrator - mean absorbance of substrate blank})} \text{ x } 100$$

where the absorbance was measured at 450 nm for all of the samples. The data were normalized and fit with a standard Boltzmann function for dose-response analysis using Origin.

B.3 Results and Discussion

The evaluation of a calcitriol EIA kit assessed the current capabilities of state of the art clinical detection of Vitamin D. This EIA kit quantifies the calcitriol concentration in the samples and assumes that the measured calcitriol concentration equals the total Vitamin D concentration in the sample. The EIA kit requires a multiple step process (Figure B.2-A), which was completed according to the included instructions. Briefly, the six included calibration solutions (0 – 544 pM) are mixed with a primary antibody

resulting in Vitamin D antibody conjugates which are then incubated with a secondary antibody-coated plate. Biotin labeled Vitamin D is then added to the plate and an enzyme conjugate is added to react with the biotin labeled Vitamin D. Finally, a proprietary chromophore is added to the wells thereby labeling the biotin molecules (and indirectly, the calcitriol molecules) with an enzyme.

Quantification of the amount of Vitamin D in each well is achieved by measuring the absorption of the chromophore at 450 nm using single wavelength UV-vis detection. A plot of normalized percent binding (B/B_0%) as a function of calcitriol concentration generates a calibration curve (Figure B2-B). The data are fit with a standard Boltzmann function for a dose-response analysis using Origin to determine a dissociation constant (K_d).[5] The K_d corresponds to the Vitamin D concentration when B/B_o% equals 0.5 and is $9.5_3 \times 10^{-11}$ M. This calculated K_d agrees with previously reported dissociation constants for the calcitriol antibody which range from 10^{-10} to 10^{-11} M.[305] While the immunoassay kit is successful in generating a calibration curve for Vitamin D, limitations of using an EIA kit for Vitamin D quantification include (1) multiple steps required to generate a detectable signal total a minimum of several days for analysis and (2) calcitriol concentration is the only Vitamin D metabolite that is monitored. An improved detection scheme that allows for simultaneous and high throughput detection of Vitamin D pro-vitamin and metabolites would overcome these current limitations associated with this EIA kit.

Initial steps toward realizing an improved Vitamin D assay are proposed based on the spectroscopic properties of these small biologically relevant molecules. The similar chemical structures and UV light sensitivity of Vitamin D pro-vitamin and metabolites challenge the successful, simultaneous detection and quantification of these suspected biologically-relevant molecules (Figure B.1). The narrow, unique vibrational features observed with Raman spectroscopy, however, make this spectroscopic detection method

an ideal signal transduction platform for complex drug mixture analysis, such as for Vitamin D pro-vitamin and metabolites as evidenced by the data in Figure B.3.

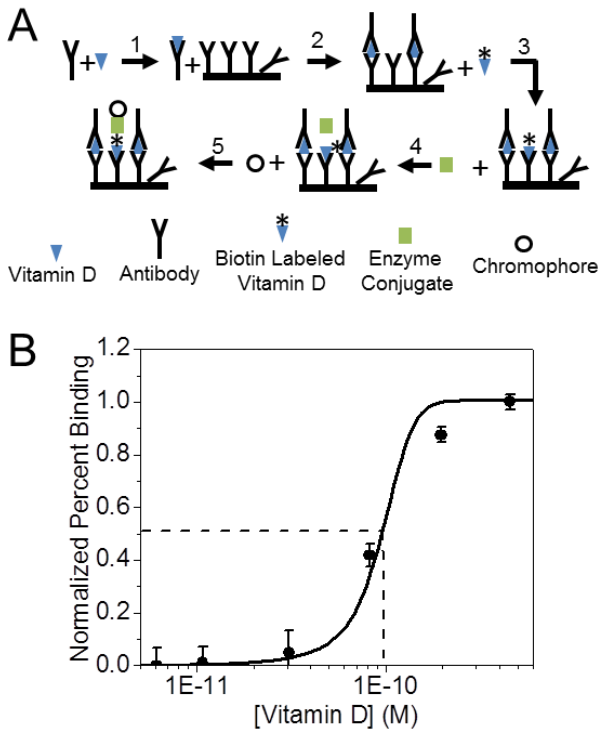

Figure B.2. Quantification of calcitriol (Vitamin D metabolite) using an enzyme immunoassay (EIA). (A) EIA scheme. The Vitamin D in the sample is (1) labeled with primary antibody resulting in a Vitamin D – antibody conjugate which is then (2) incubated with a secondary antibody coated plate, (3) biotin labeled Vitamin D is added to the plate, (4) the biotin labeled Vitamin D is reacted with an enzyme conjugate, and (5) a chromophore is added which binds with the enzyme conjugate. Quantification is achieved by measuring absorption of the chromophore at 450 nm. (B) Normalized percent binding of the Vitamin D antibody as a function of Vitamin D concentration. The solid line represents a Boltzman fit $((B/B_o\%)_{max} + ((B/B_o\%)_{min}-(B/B_o\%))/[1+\exp((\text{Vitamin D})-(\text{Vitamin D})_o)/d(\text{Vitamin D})])$, and the dotted line represents the K_d, where $K_d = 9.5_3 \times 10^{-11}$ M.

For example, Figure A2.3 depicts the Raman spectra of (1) calcitriol, (2) calcifediol, and (3) 7-dehydrocholesterol. These forms of Vitamin D exhibit both

overlapping and unique vibrational bands (Table B.1). By identifying the unique vibrational modes for these molecules, quantitative detection using Raman spectroscopy is possible. For 7-dehydrocholesterol, these vibrational bands are located at 555 cm^{-1} (ring puckering), 615 cm^{-1} (CH_3 rocking), and 1442 cm^{-1} (isopropyl asymmetric stretch). For calcifediol, unique vibrational modes are located at 741 cm^{-1} (C-C ring deformation) and 1410 cm^{-1} (CH_3 vinyl deformation). Finally, unique vibrational modes for calcitriol are located at 1159 cm^{-1} (C-O alcohol stretch). These unique bands encourage future research objectives including the following: (1) synthesis of calcifediol, calcitriol, and 7-dehydrocholesterol MIPs, (2) incorporation of these MIPs into flow through devices, (3) Raman spectral response as a function of target molecule concentration, and (4) quantification of Vitamin D molecular forms in patient samples.

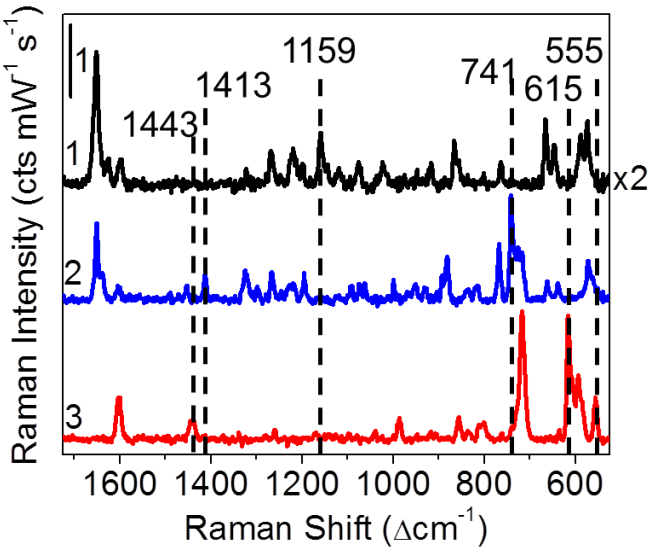

Figure B.3. Raman spectra of (1) calcitriol, (2) calcifediol, and (3) 7-dehydrocholesterol. The unique vibrational modes are labeled for 7-dehydrocholesterol (1442 cm^{-1}, isopropyl asymmetric stretch; 615 cm^{-1}, CH_2 rocking; and 555 cm^{-1}, ring puckering), calcifediol (1410 cm^{-1}, CH_2 vinyl deformation and 741 cm^{-1}, C-C ring deformation), and calcitriol (1159 cm^{-1}, C-O alcohol stretch). Raman microscopy parameters: t_{int} = 60 s, λ_{ex} = 785 nm, P = 59.0 mW, and objective = 10x.

In MIP biosensors, the large S/N of pre-concentrated drugs in the MIP and unique vibrational frequencies facilitate Raman spectral analysis for identifying and quantifying these target molecules. Cholesterol exhibits similar chemical and physical properties as Vitamin D metabolites. For this reason, a cholesterol templated MIP is synthesized using a traditional methacrylate based polymer synthesis using methacrylic acid (functional monomer) and ethylene glycol dimethacrylate (cross linking monomer) for preliminary MIP biosensor development and assessment.[34] Subsequent analysis using Raman microscopy allows for the quantification of cholesterol via molecular vibrational energy changes and is achieved by comparing sample spectra in the polymer and solid (Figure B.4).[232] Shifts in the unique Raman modes after polymerization indicate drug molecule interactions with the polymer template.

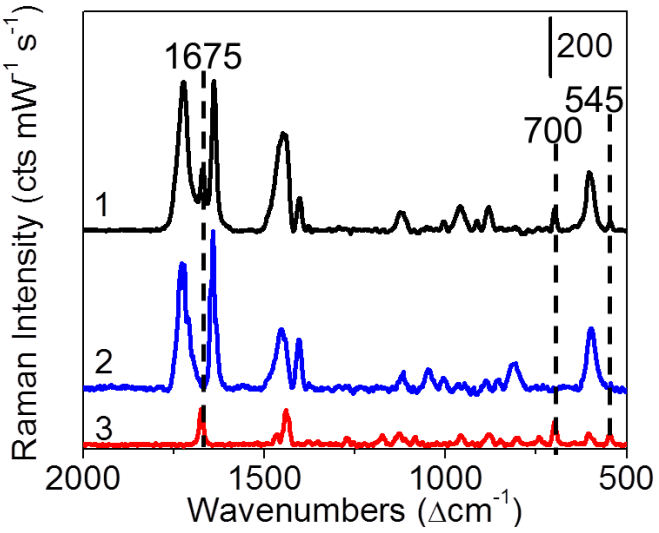

Figure B.4. Raman spectra of (1) solid cholesterol, (2) non-imprinted methacrylate-based polymer, and (3) cholesterol imprinted methacrylate-based polymer. The unique cholesterol vibrational modes are labeled as follows: 1675 cm^{-1} (C=O stretch), 700 cm^{-1} (sterol ring stretch), and 545 cm^{-1} (C-O in plane deformation). Raman parameters: t_{int} = 1 – 30 s, λ_{ex} = 532 nm, and P = 1.9 or 49 mW.

Table B.1. Raman vibrational band assignments for calcifediol, calcitriol, and 7-dehydrocholesterol.

Raman Shift (Δcm^{-1})	Assignment	Molecule
555	Ring puckering (cyclohexane)	7-dehydrocholesterol
571, 573	Ring puckering (cyclohexane)	Calcitriol, Calcifediol
588	$r(CH_2)$	Calcitriol
593	$r(CH_2)$	7-dehydrocholesterol
615	$r(CH_2)$	7-dehydrocholesterol
638	$r(CH_2)$	Calcifediol
647	δ(O-H) out of plane	Calcitriol
662, 666	δ(O-H) out of plane	Calcitriol,Calcifediol
717	δ(C-H) out of plane	7-dehydrocholesterol
747	d(C-C ring)	Calcifediol
763, 768	d(C-O)	Calcitriol, Calcifediol
801, 806	v(C-C)	Calcitriol
838, 838, 837	C-C-C skeletal vibration	All 3 Molecules
856	C-C-C skeletal vibration	7-dehydrocholesterol
866	C-C-C skeletal vibration	Calcitriol
882	C-C-C skeletal vibration	Calcifediol
917	C-C-C skeletal vibration	Calcitriol
947, 951	δ(C-H)	Calcitriol, Calcifediol
987	Ring puckering	7-dehydrocholesterol
1000	Ring puckering	Calcifediol
1023	Ring puckering	Calcitriol
1075, 1075	$r(CH_3)$	Calcitriol, Calcifediol
1094	v_a(C-C-C-C)	Calcifediol
1120	v_a(C-C-C-C)	Calcitriol
1144	v_s(C-C-C-C)	Calcitriol
1159	v(C-O)	Calcitriol
1198, 1196	v(C-C-O)	Calcitriol, Calcifediol
1219, 1219	$d(C(CH_3)_2)$	Calcitriol, Calcifediol
1260	$d(C(CH_3)_2)$	7-dehydrocholesterol
1269, 1267	$d(C(CH_3)_3)$	Calcitriol, Calcifediol

Table B.1 - Continued

1323. 1325	d(C-H)	Calcitriol, Calcifediol
1413	d(CH_3) vinyl	Calcifediol
1443	va(C(CH_3)$_2$)	7-dehydrocholesterol
1454	da(C-H)	Calcifediol
1600, 1604, 1604	ν(C=C)	All 3 Molecules
1625, 1639	d(-CH=CH-)	Calcitriol, Calcifediol
1652, 1652	ν(C=C)	Calcitriol, Calcifediol

Note: Abbreviations: δ = bending; d = deformation; ν = stretching, r = rocking, a = asymmetric, s = symmetric.

For instance, the unique Raman band for cholesterol red-shifts from 547 cm^{-1} when in solid form to 545 cm^{-1} (C-O) when bound to the MIP (Table B.2). Importantly, this 2 cm^{-1} red-shift indicates that the oxygen containing functional groups form hydrogen bonds with the nearby methacrylate polymer. The unique Raman bands for cholesterol at 700 cm^{-1} (sterol ring) and 1675 cm^{-1} (C=C), interestingly, do not shift when bound to the MIP. This indicates that the OH group in cholesterol participates in hydrogen bonding with the polymer whereas the sterol ring structure does not.

After synthesis and unique Raman band identification, template molecules require extraction from the imprinted polymer matrix prior to use of MIPs for both recognition and quantitative sample evaluation. As shown in Figure B.5A, Raman spectra collected from MIPs before and after template removal indicate the successful removal of template molecules from the polymer matrices. This is achieved through a multi-step process. Briefly, incubating the samples in ethanol for 80 hours and drying overnight to remove solvent removes the template drugs from the MIP (Figure B.5A-2). The disappearance of unique Raman bands for cholesterol suggests successful extraction (i.e., removal) from the template polymer.

Table B.2. Raman vibrational band assignments for cholesterol and polymer.

Raman Shift (Δcm^{-1})		Assignment	Molecule
Solid	MIP		
547	545	d(C-O in plane)	Cholesterol
	600	v(C-C-O)	Polymer
606		d(phenyl ring)	Cholesterol
700	700	v(steroid ring)	Cholesterol
	708	δ(C-H out of plane)	Polymer
748		d(C-C ring)	Cholesterol
804		v(C-C)	Cholesterol
	809	v_s(C-C-C)	Polymer
848		v(C-C)	Cholesterol
	857	v(C-COOH)	Polymer
880	881	skeletal vibration	Cholesterol
	954	r($C(CH)_3$)	Polymer
958	960	v($C(CH)_3$)	Cholesterol
	1010	r(CH_3)	Polymer
	1049	v(C-C)	Polymer
1084		v(C-O), ring vibration	Cholesterol
	1126	r(CH_3)	Polymer
1130		d(CH_3)	Cholesterol
1175		v(C-C-C) branched alkane	Cholesterol
	1192	v(C-O), δ(O-H in plane)	Polymer
	1241	v(Ester)	Polymer
1273		d($C(CH_3)_3$)	Cholesterol
	1290	$(CH_3)_n$ twisting vibration	Polymer
	1377	$d_a(CH_3)$	Polymer
1441		δ(CH_2), δ(CH_3)	Cholesterol
	1452	δ(CH_2)	Polymer
1467		v(C=C)	Cholesterol
1675	1675	v(C=C)	Cholesterol
	1643	v(C=C)	Polymer
	1725	v(C=O)	Polymer

Note: Abbreviations: δ = bending; d = deformation; v = stretching, r = rocking, a = asymmetric, s = symmetric.

For instance, the unique Raman band for cholesterol red-shifts from 547 cm^{-1} when in solid form to 545 cm^{-1} (C-O) when bound to the MIP (Table B.2). Importantly,

this 2 cm^{-1} red-shift indicates that the oxygen containing functional groups form hydrogen bonds with the nearby methacrylate polymer. The unique Raman bands for cholesterol at 700 cm^{-1} (sterol ring) and 1675 cm^{-1} (C=C), interestingly, do not shift when bound to the MIP. This indicates that the OH group in cholesterol participates in hydrogen bonding with the polymer whereas the sterol ring structure does not.

After synthesis and unique Raman band identification, template molecules require extraction from the imprinted polymer matrix prior to use of MIPs for both recognition and quantitative sample evaluation. As shown in Figure B.5A, Raman spectra collected from MIPs before and after template removal indicate the successful removal of template molecules from the polymer matrices. This is achieved through a multi-step process. Briefly, incubating the samples in ethanol for 80 hours and drying overnight to remove solvent removes the template drugs from the MIP (Figure B.5A). The disappearance of unique Raman bands for cholesterol suggests successful extraction (i.e., removal) from the template polymer.

During $MIP_{cholesterol}$ synthesis, the cholesterol concentration is varied from 50 – 90 mM to determine the appropriate level of cholesterol loading required for MIP stability and recognition capabilities as well as a measurable signal for quantification with a dynamic range that spans ~two orders of magnitude. The ratio of the Raman intensity of the cholesterol sterol stretch at 700 cm^{-1} to the polymer methacrylate stretch at 600 cm^{-1} is used to account for polymer sampling differences (Figure B5.B). Before cholesterol extraction (black circles), the Raman intensity ratio increases linearly with templated cholesterol concentration. Fitting the data with a linear regression yields the following equation: Raman Ratio = 0.003*[Cholesterol] + 0.039. This means that the Raman intensity ratio increases by 3.9% for every 1 mM cholesterol added to the templating solution. The Raman intensity ratio after cholesterol extraction is also shown (red circles). Because the Raman band at 700 cm^{-1} is absent from all of these spectra, all ratios are ~0 for all cholesterol imprinted polymer samples post extraction (red circles). All in

all, the linear response of the $MIP_{cholesterol}$ using Raman spectroscopy indicates the feasibility of the MIP biosensor platform for cholesterol quantification as well as similar syntheses for Vitamin D metabolite quantification. In the future, similar approaches to Vitamin D metabolite specific MIP syntheses are expected and could facilitate the need of quantitative Vitamin D metabolite detection in complex sample matrices.

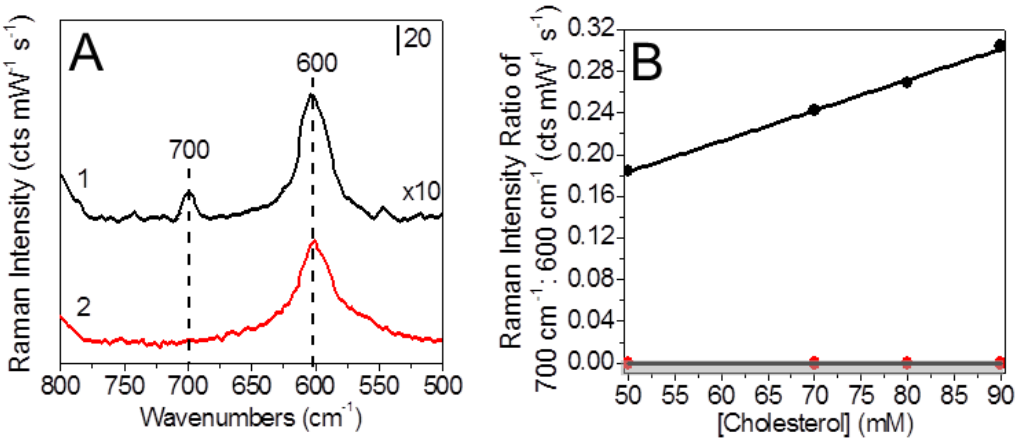

Figure B.5. Raman analysis of imprinted methacrylate-based polymers. (A) Raman of cholesterol imprinted methacrylate-based polymers (1) before* and (2) after cholesterol extraction using ethanol. The cholesterol sterol stretch at 700 cm^{-1} and the polymer methacrylate stretch at 600 cm^{-1} are labeled. (B) Comparison of the Raman intensity ratio of the cholesterol sterol stretch at 700 cm^{-1} to the polymer methacrylate stretch at 600 cm^{-1} (black circles) before and (red circles) after cholesterol extraction are shown. The gray shaded region the noise limitation of the spectrometer. *Spectrum is multiplied by 10 for plotting comparable intensities. Raman parameters: t_{int} = 2 s, λ_{ex} = 532 nm, and P = 49 mW.

B.4 Conclusions and Future Outlook

The preliminary results reported here are expected to provide insights into the development of Vitamin D biosensors which utilize MIP recognition agents as well as Raman spectroscopy for detection. Specifically, the Raman band assignments for pro-vitamin D and metabolites will prove useful for complex sample analysis as well as identification of vibrational mode shifts of the target molecules in the MIP vs. in solution.

Template extraction using ethanol appears to be an appropriate solvent for removing template molecules from Vitamin D MIPs and could be improved by implementing Soxhlet extraction. Furthermore, the incorporation of noble metal nanomaterials into the biosensor could improve detection limits of target molecules through the use of surface enhanced Raman scattering. Further development of the MIP nanobiosensor should allow for quantitative and simultaneous detection of Vitamin D molecules, and subsequently, impact how Vitamin D related diseases are diagnosed, treated, and understood.

REFERENCES

(1) Scheller, F.; Schubert, F.; Pfeiffer, D.; Hintsche, R.; Dransfeld, I.; Renneberg, R.; Wollenberger, U.; Riedel, K.; Pavlova, M.; Kuhn, M.; Muller, H.-G.; Tan, P. m.; Hoffmann, W.; Moritz, W. *Analyst* **1989**, *114*, 653.

(2) Borisov, S. M.; Wolfbeis, O. S. *Chem. Rev.* **2008**, *108*, 423.

(3) Vadgama, P.; Crump, P. W. *Analyst* **1992**, *117*, 1657.

(4) Seok, H.; Park, T. H. *BJIOAM* **2011**, *6*, 1310.

(5) *Immunoassay*; Diamandis, E. P.; Christopoulos, T. K., Eds.; Academic Press: San Diego, CA, 1996.

(6) Englebienne, P. *Analyst* **1998**, *123*, 1599.

(7) Aslan, K.; Luhrs, C. C.; Pérez-Luna, V. H. *J. Phys. Chem. B* **2004**, *108*, 15631.

(8) Pavlov, V.; Xiao, Y.; Shlyahovsky, B.; Willner, I. *J. Am. Chem. Soc.* **2004**, *126*, 11768.

(9) Thanh, N. T. K.; Rosenzweig, Z. *Anal. Chem.* **2002**, *74*, 1624.

(10) Gasparyan, V. K. *Colloid Surface B* **2010**, *80*, 180.

(11) He, L.; Rodda, T.; Haynes, C. L.; Deschaines, T.; Strother, T.; Diez-Gonzalez, F.; Labuza, T. P. *Anal. Chem.* **2011**, *83*, 1510.

(12) He, L.; Haynes, C. L.; Diez-Gonzalez, F.; Labuza, T. P. *J. Raman Spectrosc.* **2011**, *42*, 1428.

(13) Wang, G.; Park, H.-Y.; Lipert, R. J.; Porter, M. D. *Anal. Chem.* **2009**, *81*, 9643.

(14) Driskell, J. D.; Kwarta, K. M.; Lipert, R. J.; Porter, M. D.; Neill, J. D.; Ridpath, J. F. *Anal. Chem.* **2005**, *77*, 6147.

(15) Guarrotxena, N.; Bazan, G. C. *Chem. Commun.* **2011**, *47*, 8784.

(16) Grubisha, D. S.; Lipert, R. J.; Park, H.-Y.; Driskell, J.; Porter, M. D. *Anal. Chem.* **2003**, *75*, 5936.

(17) Szunerits, S.; Boukherroub, R. *Chem. Commun.* **2012**, *48*, 8999.

(18) Mayer, K. M.; Hafner, J. H. *Chem. Rev.* **2011**, *111*, 3828.

(19) Haes, A. J.; Chang, L.; Klein, W. L.; Van Duyne, R. P. *J. Am. Chem. Soc.* **2005**, *127*, 2264.

(20) Hall, W. P.; Ngatia, S. N.; Van Duyne, R. P. *J. Phys Chem. C* **2011**, *115*, 1410.

(21) Wang, X.; Xu, Y.; Chen, Y.; Li, L.; Liu, F.; Li, N. *Anal. Bioanal. Chem.* **2011**, *400*, 2085.

(22) Haes, A. J.; Van Duyne, R. P. *J. Am. Chem. Soc.* **2002**, *124*, 10596.

(23) Sim, H. R.; Wark, A. W.; Lee, H. J. *Analyst* **2010**, *135*, 2528.

(24) Bai, H.; Wang, R.; Hargis, B.; Lu, H.; Li, Y. *Sensors* **2012**, *12*, 12506.

(25) Balamurugan, S.; Mayer, K. M.; Lee, S.; Soper, S. A.; Hafner, J. H.; Spivak, D. A. *J. Mol. Recognit.* **2013**, *26*, 402.

(26) Bantz, K. C.; Meyer, A. F.; Wittenberg, N. J.; Im, H.; Kurtulus, O.; Lee, S. H.; Lindquist, N. C.; Oh, S.-H.; Haynes, C. L. *Phys. Chem. Chem. Phys.* **2011**, *13*, 11551.

(27) Cheong, W. J.; Yang, S. H.; Ali, F. *J. Sep. Sci.* **2013**, *36*, 609.

(28) Haupt, K.; Mosbach, K. *Chem. Rev.* **2000**, *100*, 2495.

(29) Piletsky, S. A.; Matuschewski, H.; Schedler, U.; Wilpert, A.; Piletska, E. V.; Thiele, T. A.; Ulbricht, M. *Macromolecules* **2000**, *33*, 3092.

(30) Xie, C.; Liu, B.; Wang, Z.; Gao, D.; Guan, G.; Zhang, Z. *Anal. Chem.* **2007**, *80*, 437.

(31) Piletsky, S. A.; Piletskaya, E. V.; Sergeyeva, T. A.; Panasyuk, T. L.; El'skaya, A. V. *Sensor Actuat. B-Chem.* **1999**, *60*, 216.

(32) Wulff, G. *Chem. Rev.* **2001**, *102*, 1.

(33) Nematollahzadeh, A.; Shojaei, A.; Abdekhodaie, M. J.; Sellergren, B. *J. Colloid Interf. Sci.* **2013**, *404*, 117.

(34) Spizzirri, U. G.; Peppas, N. A. *Chem. Mater.* **2005**, *17*, 6719.

(35) Lasáková, M.; Thiébaut, D.; Jandera, P.; Pichon, V. *J. Sep. Sci.* **2009**, *32*, 1036.

(36) Tse Sum Bui, B.; Merlier, F.; Haupt, K. *Anal. Chem.* **2010**, *82*, 4420.

(37) González, G.; Hernando, P.; Durand Alegría, J. *Anal. Bioanal. Chem.* **2009**, *394*, 963.

(38) Yonamine, Y.; Hoshino, Y.; Shea, K. J. *Biomacromolecles* **2012**, *13*, 2952.

(39) Moschallski, M.; Evers, A.; Brandstetter, T.; Rühe, J. *Anal. Chim. Act.* **2013**, *781*, 72.

(40) Gao, F.-X.; Ma, X.-T.; He, X.-W.; Li, W.-Y.; Zhang, Y.-K. *Colloid Surface A* **2013**, *433*, 191.

(41) Zhang, X.; Du, X.; Huang, X.; Lv, Z. *J. Am. Chem. Soc.* **2013**, *135*, 9248.

(42) Tov, O. Y.; Luvitch, S.; Bianco-Peled, H. *J. Sep. Sci.* **2010**, *33*, 1673.

(43) Zeng, Z.; Hoshino, Y.; Rodriguez, A.; Yoo, H.; Shea, K. J. *ACS Nano* **2009**, *4*, 199.

(44) Bossi, A.; Bonini, F.; Turner, A. P. F.; Piletsky, S. A. *Biosens. Bioelectron.* **2007**, *22*, 1131.

(45) Moreira, F. T. C.; Sharma, S.; Dutra, R. A. F.; Noronha, J. P. C.; Cass, A. E. G.; Sales, M. G. F. *Biosens. Bioelectron.* **2013**, *45*, 237.

(46) Ambrosini, S.; Beyazit, S.; Haupt, K.; Tse Sum Bui, B. *Chem. Commun.* **2013**, *49*, 6746.

(47) Hoshino, Y.; Haberaecker Iii, W. W.; Kodama, T.; Zeng, Z.; Okahata, Y.; Shea, K. J. *J. Am. Chem. Soc.* **2010**, *132*, 13648.

(48) Hoshino, Y.; Kodama, T.; Okahata, Y.; Shea, K. J. *J. Am. Chem. Soc.* **2008**, *130*, 15242.

(49) Hoshino, Y.; Koide, H.; Urakami, T.; Kanazawa, H.; Kodama, T.; Oku, N.; Shea, K. J. *J. Am. Chem. Soc.* **2010**, *132*, 6644.

(50) Hoshino, Y.; Shea, K. J. *J. Mater. Chem.* **2011**, *21*, 3517.

(51) Boopathi, M.; Suryanarayana, M. V. S.; Nigam, A. K.; Pandey, P.; Ganesan, K.; Singh, B.; Sekhar, K. *Biosens. Bioelectron.* **2006**, *21*, 2339.

(52) Piszkiewicz, S.; Kirkbride, E. A.; Doreng-Stearns, N.; Henderson, B. R.; Lenker, M. A.; Tang, E.; Kawashiri, L. H.; Nichols, C. S.; Moore, S. C.; Sogo, S. G. *Chem. Commun.* **2013**, *49*, 5954.

(53) Tse Sum Bui, B.; Haupt, K. *Anal. Bioanal. Chem.* **2010**, *398*, 2481.

(54) Cheong, W. J.; Ali, F.; Choi, J. H.; Lee, J. O.; Yune Sung, K. *Talanta* **2013**, *106*, 45.

(55) Fuchs, Y.; Soppera, O.; Haupt, K. *Anal. Chim. Act.* **2012**, *717*, 7.

(56) Suedee, R. *Int. J. Pharm. Sci. Rev. Res.* **2013**, *44*, 235.

(57) Haupt, K. *Nat. Mater.* **2010**, *9*, 612.

(58) Poma, A.; Guerreiro, A.; Whitcombe, M. J.; Piletska, E. V.; Turner, A. P. F.; Piletsky, S. A. *Adv. Funct. Mater.* **2013**, *23*, 2821.

(59) Moczko, E.; Poma, A.; Guerreiro, A.; Perez de Vargas Sansalvador, I.; Caygill, S.; Canfarotta, F.; Whitcombe, M. J.; Piletsky, S. *Nanoscale* **2013**, *5*, 3733.

(60) Vasapollo, G.; Sole, R. D.; Mergola, L.; Lazzoi, M. R.; Scardino, A.; Scorrano, S.; Mele, G. *Int. J. Mol. Sci.* **2011**, *12*, 5908.

(61) Mayes, A. G.; Whitcombe, M. J. *Adv. Drug Deliver. Rev.* **2005**, *57*, 1742.

(62) Jana, N. R.; Ying, J. Y. *Adv. Mater.* **2008**, *20*, 430.

(63) Haynes, C. L.; Haes, A. J.; McFarland, A. D.; Van Duyne, R. P. In *Topics in Fluorescence*; Lakowicz, J. R., Ed.; Plenum Press: New York, 2003; Vol. 8, p 1.

(64) Haynes, C. L.; McFarland, A. D.; Van Duyne, R. P. *Anal. Chem.* **2005**, *7*, 338A.

(65) Volkert, A. A.; Subramaniam, V.; Ivanov, M. R.; Goodman, A. M.; Haes, A. J. *ACS Nano* **2011**, *5*, 4570.

(66) Mie, G. *Ann. Phys.* **1908**, *25*, 377.

(67) Volkert, A. A.; Subramaniam, V.; Haes, A. J. *Chem. Commun.* **2011**, *47*, 478.

(68) Hwang, C.-C.; Lee, W.-C. *J. Chromatogr. A* **2002**, *962*, 69.

(69) Kantarovich, K.; Tsarfati, I.; Gheber, L. A.; Haupt, K.; Bar, I. *Anal. Chem.* **2009**, *81*, 5686.

(70) Guerreiro, A. R.; Chianella, I.; Piletska, E.; Whitcombe, M. J.; Piletsky, S. A. *Biosens. Bioelectron.* **2009**, *24*, 2740.

(71) Gam-Derouich, S.; Mahouche-Chergui, S.; Truong, S.; Ben Hassen-Chehimi, D.; Chehimi, M. M. *Polymer* **2011**, *52*, 4463.

(72) Gültekin, A.; Diltemiz, S. E.; Ersöz, A.; Sarıözlü, N. Y.; Denizli, A.; Say, R. *Talanta* **2009**, *78*, 1332.

(73) Gültekin, A.; Ersöz, A.; Hür, D.; Sarıözlü, N. Y.; Denizli, A.; Say, R. *Appl. Surf. Sci.* **2009**, *256*, 142.

(74) Gültekin, A.; Ersöz, A.; Denizli, A.; Say, R. *Sensor Actuat. B-Chem.* **2012**, *162*, 153.

(75) Gültekin, A.; Ersöz, A.; Denizli, A.; Say, R. *Talanta* **2012**, *93*, 364.

(76) Bompart, M.; De Wilde, Y.; Haupt, K. *Adv. Mater.* **2010**, *22*, 2343.

(77) Kantarovich, K.; Tsarfati, I.; Gheber, L. A.; Haupt, K.; Bar, I. *Biosens. Bioelectron.* **2010**, *26*, 809.

(78) Kantarovich, K.; Tsarfati-BarAd, I.; Gheber, L.; Haupt, K.; Bar, I. *Plasmonics* **2013**, *8*, 3.

(79) Kostrewa, S.; Emgenbroich, M.; Klockow, D.; Wulff, G. *Macromol. Chem. Physic.* **2003**, *204*, 481.

(80) Kan, X.; Liu, T.; Li, C.; Zhou, H.; Xing, Z.; Zhu, A. *J Solid State Electrochem* **2012**, *16*, 3207.

(81) Wang, H.; Zhao, H.; Quan, X.; Chen, S. *Electroanal.* **2011**, *23*, 1863.

(82) Xue, J.-Q.; Li, D.-W.; Qu, L.-L.; Long, Y.-T. *Anal. Chim. Act.* **2013**, *777*, 57.

(83) Li, S.; Du, D.; Huang, J.; Tu, H.; Yang, Y.; Zhang, A. *Analyst* **2013**, *138*, 2761.

(84) Holthoff, E. L.; Stratis-Cullum, D. N.; Hankus, M. E. *Sensors* **2011**, *11*, 2700.

(85) Ton, X.-A.; Tse Sum Bui, B.; Resmini, M.; Bonomi, P.; Dika, I.; Soppera, O.; Haupt, K. *Angew. Chem. Int. Ed.* **2013**, *52*, 8317.

(86) Yu, D.; Zeng, Y.; Qi, Y.; Zhou, T.; Shi, G. *Biosens. Bioelectron.* **2012**, *38*, 270.

(87) Matsui, J.; Akamatsu, K.; Hara, N.; Miyoshi, D.; Nawafune, H.; Tamaki, K.; Sugimoto, N. *Anal. Chem.* **2005**, *77*, 4282.

(88) Matsui, J.; Akamatsu, K.; Nishiguchi, S.; Miyoshi, D.; Nawafune, H.; Tamaki, K.; Sugimoto, N. *Anal. Chem.* **2004**, *76*, 1310.

(89) Kara, M.; Uzun, L.; Kolayli, S.; Denizli, A. *J. Appl. Polym. Sci.* **2013**, *129*, 2273.

(90) Riskin, M.; Ben-Amram, Y.; Tel-Vered, R.; Chegel, V.; Almog, J.; Willner, I. *Anal. Chem.* **2011**, *83*, 3082.

(91) Riskin, M.; Tel-Vered, R.; Willner, I. *Adv. Mater.* **2010**, *22*, 1387.

(92) Lépinay, S.; Kham, K.; Millot, M.-C.; Carbonnier, B. *Chem. Pap.* **2012**, *66*, 340.

(93) Sener, G.; Uzun, L.; Say, R.; Denizli, A. *Sensor Actuat. B-Chem.* **2011**, *160*, 791.

(94) Brown, K. R.; Walter, D. G.; Natan, M. J. *Chem. Mater.* **2000**, *12*, 306.

(95) Cao, L.; Zhu, T.; Liu, Z. *J. Colloid Interf. Sci.* **2006**, *293*, 69.

(96) Long, N. N.; Vu, L. V.; Kiem, C. D.; Doanh, S. C.; Nguyet, C. T.; Hang, P. T.; Thien, N. D.; Quynh, L. M. *J. Phys. Conf. Ser.* **2009**, *187*, 012026.

(97) Zou, X.; Ying, E.; Dong, S. *Nanotechnology* **2006**, *17*, 4758.

(98) Cao, G. *Nanostructures and Nanomaterials: Synthesis, Properties, and Applications*; Imperial College Press: London, 2004.

(99) Weisbecker, C. S.; Merritt, M. V.; Whitesides, G. M. *Langmuir* **1996**, *12*, 3763.

(100) Mayya, K. S.; Patil, V.; Sastry, M. *Langmuir* **1997**, *13*, 3944.

(101) Jana, N. R.; Gearheart, L.; Murphy, C. J. *Langmuir* **2001**, *17*, 6782.

(102) Ji, X.; Song, X.; Li, J.; Bai, Y.; Yang, W.; Peng, X. *J. Am. Chem. Soc.* **2007**, *129*, 13939.

(103) Kreibig, U.; Vollmer, M. *Cluster Materials*; Springer-Verlag: Heidelberg, Germany, 1995; Vol. 25.

(104) Hunter, R. J. *Introduction to Modern Colloid Science*; Oxford University Press: Oxford, 1993.

(105) Quintanilla, A.; Butselaar-Orthlieb, V. C. L.; Kwakernaak, C.; Sloof, W. G.; Kreutzer, M. T.; Kapteijn, F. *J. Catal.* **2010**, *271*, 104.

(106) Magomedov, M. N. *Phys. Solid State* **2004**, *46*, 954.

(107) Callister, W. D. *Materials Science And Engineering: An Introduction*; John Wiley & Sons, 2007.

(108) Nikoobakht, B.; El-Sayed, M. A. *Chem. Mater.* **2003**, *15*, 1957.

(109) Bisson, L.; Boissiere, C.; Sanchez, C.; Tomazeau, C.; Uzio, D. *Mater. Res. Soc. Symp. Proc.* **2007**, *1017*.

(110) Ulman, A. *Chem. Rev.* **1996**, *96*, 1533.

(111) Hickman, J. J.; Ofer, D.; Laibinis, P. E.; Whitesides, G. M.; Wrighton, M. S. *Science* **1991**, *252*, 688.

(112) Mirkin, C. A.; Ratner, M. A. *Annu. Rev. Phys. Chem* **1992**, *43*, 719.

(113) Wollman, E. W.; Kang, D.; Frisbie, C. D.; Lorkovic, I. M.; Wrighton, M. S. *J. Am. Chem. Soc.* **1994**, *116*, 4395.

(114) Bonneman, H.; Richards, R. M. *Eur. J. Inorg. Chem.* **2001**, *10*, 2455.

(115) Noh, J.; Kato, H. S.; Kawai, M.; Hara, M. *J. Phys. Chem. B* **2006**, *110*, 2793.

(116) Dameron, A. A.; Charles, L. F.; Weiss, P. S. *J. Am. Chem. Soc.* **2005**, *127*, 8697.

(117) Crooks, R. M.; Ricco, A. J. *Accounts Chem. Res.* **1998**, *31*, 219.

(118) Badia, A.; Lennox, R. B.; Reven, L. *Accounts Chem. Res.* **2000**, *33*, 475.

(119) Adams, D. M.; Brus, L.; Chidsey, C. E. D.; Creager, S.; Creutz, C.; Kagan, C. R.; Kamat, P. V.; Lieberman, M.; Lindsay, S.; Marcus, R. A.; Metzger, R. M.; Michel-Beyerle, M. E.; Miller, J. R.; Newton, M. D.; Rolison, D. R.; Sankey, O.; Schanze, K. S.; Yardley, J.; Zhu, X. *J. Phys. Chem. B* **2003**, *107*, 6668.

(120) Fendler, J. H. *Chem. Mater.* **2001**, *13*, 3196.

(121) Si, S.; Mandal, T. K. *Langmuir* **2006**, *23*, 190.

(122) Brust, M.; Walker, M.; Bethell, D.; Schiffrin, D. J.; Whyman, R. *J. Chem. Soc. Chem. Comm.* **1994**, 801.

(123) Weare, W. W.; Reed, S. M.; Warner, M. G.; Hutchison, J. E. *J. Am. Chem. Soc.* **2000**, *122*, 12890.

(124) Joo, S.-W.; Kim, W.-J.; Yoon, W. S.; Choi, I. S. *J. Raman Spectrosc.* **2003**, *34*, 271.

(125) Yang, A.-C.; Weng, C.-I. *J. Phys Chem. C* **2010**, *114*, 8697.

(126) Creager, S. E.; Clarke, J. *Langmuir* **1994**, *10*, 3675.

(127) Tseng, W.-L.; Huang, M.-F.; Huang, Y.-F.; Chang, H.-T. *Electrophoresis* **2005**, *26*, 3069.

(128) Haes, A. J.; Hall, W. P.; Chang, L.; Klein, W. L.; Van Duyne, R. P. *Nano Lett.* **2004**, *4*, 1029.

(129) Haes, A. J.; Zhao, J.; Zou, S.; Own, C. S.; Marks, L. D.; Schatz, G. C.; Van Duyne, R. P. *J. Phys. Chem. B* **2005**, *109*, 11158.

(130) Templeton, A. C.; Wuelfing, W. P.; Murray, R. W. *Accounts Chem. Res.* **2000**, *33*, 27.

(131) Daniel, M.-C.; Astruc, D. *Chem. Rev.* **2004**, *104*, 293.

(132) Chechik, V. *J. Am. Chem. Soc.* **2004**, *126*, 7780.

(133) Hill, H. D.; Millstone, J. E.; Banholzer, M. J.; Mirkin, C. A. *ACS Nano* **2009**, *3*, 418.

(134) Zhang, S.; Leem, G.; Srisombat, L.-o.; Lee, T. R. *J. Am. Chem. Soc.* **2008**, *130*, 113.

(135) Leontowich, A. F. G.; Calver, C. F.; Dasog, M.; Scott, R. W. J. *Langmuir* **2009**, *26*, 1285.

(136) Sardar, R.; Heap, T. B.; Shumaker-Parry, J. S. *J. Am. Chem. Soc.* **2007**, *129*, 5356.

(137) Zhang, Z.; Yan, B.; Liu, K.; Liao, Y.; Liu, H. *Electrophoresis* **2009**, *30*, 379.

(138) Wang, G.; Murray, R. W. *Nano Lett.* **2004**, *4*, 95.

(139) Warner, M. G.; Hutchison, J. E. *Nat Mater* **2003**, *2*, 272.

(140) Wyrwa, D.; Beyer, N.; Schmid, G. *Nano Lett.* **2002**, *2*, 419.

(141) DeVries, G. A.; Brunnbauer, M.; Hu, Y.; Jackson, A. M.; Long, B.; Neltner, B. T.; Uzun, O.; Wunsch, B. H.; Stellacci, F. *Science* **2007**, *315*, 358.

(142) Sardar, R.; Shumaker-Parry, J. S. *Nano Lett.* **2008**, *8*, 731.

(143) Phillips, R. L.; Miranda, O. R.; You, C.-C.; Rotello, V. M.; Bunz, U. H. F. *Angew. Chem. Int. Ed.* **2008**, *47*, 2590.

(144) Thomas, K. G.; Kamat, P. V. *Accounts Chem. Res.* **2003**, *36*, 888.

(145) Marinakos, S. M.; Brousseau, L. C.; Jones, A.; Feldheim, D. L. *Chem. Mater.* **1998**, *10*, 1214.

(146) Shipway, A. N.; Lahav, M.; Blonder, R.; Willner, I. *Chem. Mater.* **1998**, *11*, 13.

(147) Katz, E.; Willner, I. *Angew. Chem. Int. Ed.* **2004**, *43*, 6042.

(148) Ghosh, P. S.; Kim, C.-K.; Han, G.; Forbes, N. S.; Rotello, V. M. *ACS Nano* **2008**, *2*, 2213.

(149) Bastús, N. G.; Sánchez-Tilló, E.; Pujals, S.; Farrera, C.; López, C.; Giralt, E.; Celada, A.; Lloberas, J.; Puntes, V. *ACS Nano* **2009**, *3*, 1335.

(150) Selvakannan, P. R.; Mandal, S.; Phadtare, S.; Pasricha, R.; Sastry, M. *Langmuir* **2003**, *19*, 3545.

(151) Heeb, R.; Lee, S.; Venkataraman, N. V.; Spencer, N. D. *ACS Appl. Mater. Interfaces* **2009**, *1*, 1105.

(152) Finklea, H. O. *Electroanal. Chem.* **1996**, *19*, 109.

(153) Preiner, M. J.; Melosh, N. A. *Langmuir* **2009**, *25*, 2585.

(154) Lusk, A. T.; Jennings, G. K. *Langmuir* **2001**, *17*, 7830.

(155) Campuzano, S.; Pedrero, M.; Montemayor, C.; Fatás, E.; Pingarrón, J. M. *J. Electroanal. Chem.* **2006**, *586*, 112.

(156) Kwon, S.; Choi, J.; Lee, H.; Noh, J. *Colloid Surface A* **2008**, *313–314*, 324.

(157) Yamada, R.; Wano, H.; Uosaki, K. *Langmuir* **2000**, *16*, 5523.

(158) Poirier, G. E. *Langmuir* **1997**, *13*, 2019.

(159) Losic, D.; Shapter, J. G.; Gooding, J. J. *Aust. J. Chem.* **2001**, *54*, 643.

(160) Losic, D.; Shapter, J. G.; Gooding, J. J. *Langmuir* **2001**, *17*, 3307.

(161) Losic, D.; Gooding, J. J.; Shapter, J. G.; Hibbert, D. B.; Short, K. *Electroanal.* **2001**, *13*, 1385.

(162) Grabar, K. C.; Freeman, R. G.; Hommer, M. B.; Natan, M. J. *Anal. Chem.* **1995**, *67*, 735.

(163) Ivanov, M. R.; Bednar, H. R.; Haes, A. J. *ACS Nano* **2009**, *3*, 386.

(164) Haiss, W.; Thanh, N. T. K.; Aveyard, J.; Fernig, D. G. *Anal. Chem.* **2007**, *79*, 4215.

(165) Hurst, S. J.; Lytton-Jean, A. K. R.; Mirkin, C. A. *Anal. Chem.* **2006**, *78*, 8313.

(166) Usher, C. R.; Baltrusaitis, J.; Grassian, V. H. *Langmuir* **2007**, *23*, 7039.

(167) Kreibig, U. In *Handbook of Optical Properties*; Hummel, R. E., Wissmann, P., Eds.; CRC Press: Boca Raton, 1997; Vol. 2, p 145.

(168) Haes, A. J.; Haynes, C. L.; McFarland, A. D.; Schatz, G. C.; Van Duyne, R. P.; Zou, S. *MRS Bull.* **2005**, *30*, 368.

(169) El-Sayed, M. A. *Accounts Chem. Res.* **2001**, *34*, 257.

(170) Link, S.; El-Sayed, M. A. *J. Phys. Chem. B* **1999**, *103*, 8410.

(171) Bohren, C. F.; Huffman, D. R. *Absorption and Scattering of Light by Small Particles*; Wiley Interscience: New York, 1983.

(172) Schmid, G. *Chem. Rev.* **1992**, *92*, 1709.

(173) Aslan, K.; Pérez-Luna, V. H. *Langmuir* **2002**, *18*, 6059.

(174) Pham, T.; Jackson, J. B.; Halas, N. J.; Lee, T. R. *Langmuir* **2002**, *18*, 4915.

(175) Cheng, Q.; Brajter-Toth, A. *Anal. Chem.* **1992**, *64*, 1998.

(176) Rooth, M.; Shaw, A. M. *J. Phys Chem. C* **2007**, *111*, 15363.

(177) Cheng, Q.; Brajter-Toth, A. *Anal. Chem.* **1996**, *68*, 4180.

(178) Kimura, K.; Takashima, S.; Ohshima, H. *J. Phys. Chem. B* **2002**, *106*, 7260.

(179) Dougherty, G. M.; Rose, K. A.; Tok, J. B. H.; Pannu, S. S.; Chuang, F. Y. S.; Sha, M. Y.; Chakarova, G.; Penn, S. G. *Electrophoresis* **2008**, *29*, 1131.

(180) Song, Y.; Harper, A. S.; Murray, R. W. *Langmuir* **2005**, *21*, 5492.

(181) Hostetler, M. J.; Wingate, J. E.; Zhong, C.-J.; Harris, J. E.; Vachet, R. W.; Clark, M. R.; Londono, J. D.; Green, S. J.; Stokes, J. J.; Wignall, G. D.; Glish, G. L.; Porter, M. D.; Evans, N. D.; Murray, R. W. *Langmuir* **1998**, *14*, 17.

(182) Badia, A.; Gao, W.; Singh, S.; Demers, L.; Cuccia, L.; Reven, L. *Langmuir* **1996**, *12*, 1262.

(183) Terrill, R. H.; Postlethwaite, T. A.; Chen, C.-h.; Poon, C.-D.; Terzis, A.; Chen, A.; Hutchison, J. E.; Clark, M. R.; Wignall, G. *J. Am. Chem. Soc.* **1995**, *117*, 12537.

(184) Hori, H.; Yamamoto, Y.; Iwamoto, T.; Miura, T.; Teranishi, T.; Miyake, M. *Phys. Rev. B* **2004**, *69*, 174411.

(185) Crespo, P.; Litrán, R.; Rojas, T. C.; Multigner, M.; de la Fuente, J. M.; Sánchez-López, J. C.; García, M. A.; Hernando, A.; Penadés, S.; Fernández, A. *Phys. Rev. Lett.* **2004**, *93*, 087204.

(186) Kohlmann, O.; Steinmetz, W. E.; Mao, X.-A.; Wuelfing, W. P.; Templeton, A. C.; Murray, R. W.; Johnson, C. S. *J. Phys. Chem. B* **2001**, *105*, 8801.

(187) Schmitt, H.; Badia, A.; Dickinson, L.; Reven, L.; Lennox, R. B. *Adv. Mater.* **1998**, *10*, 475.

(188) Park, J.-N.; Forman, A. J.; Tang, W.; Cheng, J.; Hu, Y.-S.; Lin, H.; McFarland, E. W. *Small* **2008**, *4*, 1694.

(189) Porter, L. A.; Ji, D.; Westcott, S. L.; Graupe, M.; Czernuszewicz, R. S.; Halas, N. J.; Lee, T. R. *Langmuir* **1998**, *14*, 7378.

(190) Johnson, S. R.; Evans, S. D.; Mahon, S. W.; Ulman, A. *Langmuir* **1997**, *13*, 51.

(191) Lu, H. B.; Campbell, C. T.; Castner, D. G. *Langmuir* **2000**, *16*, 1711.

(192) Castner, D. G.; Hinds, K.; Grainger, D. W. *Langmuir* **1996**, *12*, 5083.

(193) Baer, D. R.; Engelhard, M. H. *J. Electron. Spectrosc.* **2010**, *178–179*, 415.

(194) Lumsden, J. B. In *Materials Characterization*; Whan, R. E., Ed.; American Society for Metals: Metals Park, OH, 1986; Vol. 10.

(195) Giray, C. B.; Dogan, M.; Akalin, A.; Baltrusaitis, J.; Chan, D. C. N.; Skinner, H. C. W.; Dogan, A. U. *Scanning* **2007**, *29*, 206.

(196) Jablonski, A.; 1.1 ed.; National Institues of Standards and Technology: Gaithersburg, MD, 2000.

(197) Beilschmidt, H.; Tiliuin, I. S.; Werner, W. S. M. *Surf. Interf. Anal.* **1994**, *22*, 120.

(198) Schmid, G. *Adv. Eng. Mater.* **2001**, *3*, 737.

(199) Cademartiri, L.; Ozin, G. *Concepts of Nanochemistry*; Wiley-VCH: Weinheim, Germany, 2009.

(200) Wang, Z. L.; Petroski, J. M.; Green, T. C.; El-Sayed, M. A. *J. Phys. Chem. B* **1998**, *102*, 6145.

(201) Dong, Y.; Abaci, S.; Shannon, C.; Bozack, M. J. *Langmuir* **2003**, *19*, 8922.

(202) Madoz, J.; Kuznetzov, B. A.; Medrano, F. J.; Garcia, J. L.; Fernandez, V. M. *J. Am. Chem. Soc.* **1997**, *119*, 1043.

(203) Kuwabata, S.; Fukuzaki, R.; Nishizawa, M.; Martin, C. R.; Yoneyama, H. *Langmuir* **1999**, *15*, 6807.

(204) Mazur, M.; Krysiński, P. *Langmuir* **2001**, *17*, 7093.

(205) Willey, T. M.; Vance, A. L.; Bostedt, C.; van Buuren, T.; Meulenberg, R. W.; Terminello, L. J.; Fadley, C. S. *Langmuir* **2004**, *20*, 4939.

(206) Porter, M. D.; Bright, T. B.; Allara, D. L.; Chidsey, C. E. D. *J. Am. Chem. Soc.* **1987**, *109*, 3559.

(207) Schlenoff, J. B.; Li, M.; Ly, H. *J. Am. Chem. Soc.* **1995**, *117*, 12528.

(208) Doneux, T.; De Decker, Y. *Langmuir* **2009**, *25*, 2199.

(209) Fawcett, W. R.; Tikanen, A. C. *J Phys. Chem.-US* **1996**, *100*, 4251.

(210) Fawcett, W. R.; Smagala, T. G. *Electrochim. Acta* **2008**, *53*, 5136.

(211) Kunze, K. K.; Netz, R. R. *Phys. Rev. Lett.* **2000**, *85*, 4389.

(212) Kamath, G.; Cao, F.; Potoff, J. J. *J. Phys. Chem. B* **2004**, *108*, 14130.

(213) Akram, M.; Stuart, M. C.; Wong, D. K. Y. *Anal. Chim. Act.* **2004**, *504*, 243.

(214) Volkert, A. A.; Haes, A. J. *Analyst* **2014**, *139*, 21.

(215) Suárez-Rodríguez, J. L.; Díaz-García, M. E. *Anal. Chim. Act.* **2000**, *405*, 67.

(216) Jakusch, M.; Janotta, M.; Mizaikoff, B.; Mosbach, K.; Haupt, K. *Anal. Chem.* **1999**, *71*, 4786.

(217) Roca, M.; Haes, A. J. *J. Am. Chem. Soc.* **2008**, *130*, 14273.

(218) Rosengren-Holmberg, J. P.; Karlsson, J. G.; Svenson, J.; Andersson, H. S.; Nicholls, I. A. *Org. Biomol. Chem.* **2009**, *7*, 3148.

(219) Ramsey, J. D.; Collins, G. E. *Anal. Chem.* **2005**, *77*, 6664.

(220) Ericson, C.; Liao, J.-L.; Nakazato, K. i.; Hjertén, S. *J. Chromatogr. A* **1997**, *767*, 33.

(221) Fahmy, R.; Marnane, B.; Bensley, D.; Hollenbeck, R. G. *AAPS PharmSci* **2002**, *4*, 137.

(222) Bondesson, L.; Mikkelsen, K. V.; Luo, Y.; Garberg, P.; Ågren, H. *Spectrochim. Acta A* **2007**, *66*, 213.

(223) Gunasekaran, S.; Sankari, G.; Ponnusamy, S. *Spectrochim. Acta A* **2005**, *61*, 117.

(224) Nanubolu, J. B.; Burley, J. C. *Mol. Pharm.* **2012**, *9*, 1544.

(225) Socrates, G. *Infrared and Raman Characteristic Group Frequencies: Tables and Charts*; 3 ed.; John Wiley & Sons Ltd.: West Sussex, England, 2001.

(226) Zou, Y.; Armstrong, S. R.; Jessop, J. L. P. *J. Biomed. Mater. Res. A* **2008**, *86A*, 883.

(227) Zou, Y.; Armstrong, S. R.; Jessop, J. L. P. *J. Biomed. Mater. Res. A* **2010**, *94A*, 288.

(228) McStay, D.; Al-Obaidi, A. H.; Hoskins, R.; Quinn, P. J. *J. Opt. A-Pure Appl. Op.* **2005**, *7*, S340.

(229) Li, Y.; Li, X.; Dong, C.; Qi, J.; Han, X. *Carbon* **2010**, *48*, 3427.

(230) Kantarovich, K.; Belmont, A.-S.; Haupt, K.; Bar, I.; Gheber, L. A. *Appl. Phys. Lett.* **2009**, *94*.

(231) Torii, H.; Tatsumi, T.; Tasumi, M. *J. Raman Spectrosc.* **1998**, *29*, 537.

(232) Preston, T. C.; Nuruzzaman, M.; Jones, N. D.; Mittler, S. *J. Phys Chem. C* **2009**, *113*, 14236.

(233) Novartis Consumer Health, I. 2014; Vol. 2014.

(234) Kuzmič, P. *Anal. Biochem.* **1996**, *237*, 260.

(235) Klotz, I. M. *Ligand-Receptor Energetics: A Guide for the Perplexed*; Wiley: New York, N. Y., 1997.

(236) Byrne, M. E.; Park, K.; Peppas, N. A. *Adv. Drug Deliver. Rev.* **2002**, *54*, 149.

(237) Zhang, T.; Liu, F.; Chen, W.; Wang, J.; Li, K. *Anal. Chim. Act.* **2001**, *450*, 53.

(238) Kuzmic, P. *DynaFit Scripting Manual Version 3.28*; 6th ed.; BioKin Press: Pullman, WA, 2005.

(239) Matsui, J.; Miyoshi, Y.; Doblhoff-Dier, O.; Takeuchi, T. *Anal. Chem.* **1995**, *67*, 4404.

(240) Seong, H.; Lee, H. B.; Park, K. *J. Biomat. Sci-Polym. Sci.* **2002**, *13*, 637.

(241) Wilkins, J. A.; Xiang, R.; Horváth, C. *Anal. Chem.* **2002**, *74*, 3933.

(242) Labrou, N. E. *J. Chromatogr. B* **2003**, *790*, 67.

(243) Sellergren, B. *Anal. Chem.* **1994**, *66*, 1578.

(244) Naseri, M. T.; Hemmatkhah, P.; Hosseini, M. R. M.; Assadi, Y. *Analytica Chimica Acta* **2008**, *610*, 135.

(245) Bjarnason, B.; Chimuka, L.; Ramström, O. *Anal. Chem.* **1999**, *71*, 2152.

(246) Penn, M. A.; Drake, D. M.; Driskell, J. D. *Anal. Chem.* **2013**, *85*, 8609.

(247) Ansell, R. J. *J. Chromatogr. B* **2004**, *804*, 151.

(248) Duggleby, R. G.; Wood, C. *J. Biochem.* **1989**, *258*, 397.

(249) *The Immunoassay Handbook: Theory and applications of lignad binding, ELISA, and related techniques*; 4th ed.; Elsevier: Waltham, MA, 2013.

(250) Gam-Derouich, S.; Mahouche-Chergui, S.; Truong, S.; Hassen-Chehimi, D. B.; Chehimi, M. M. *Polymer* **2011**, *52*, 4463.

(251) Gültekin, A.; Diltemiz, S. E.; Ersoz, A.; Sariozlu, N. Y.; Denizli, A.; Say, R. *Talanta* **2009**, *78*, 1332.

(252) Gültekin, A.; Ersoz, A.; Hur, D.; Sariozlu, Y. N.; Denizli, A.; Say, R. *Applied Surface Science* **2009**, *256*, 142.

(253) Gültekin, A.; Ersoz, A.; Denizli, A.; Say, R. *Sensors and Actuators B* **2012**, *162*, 153.

(254) Gültekin, A.; Ersoz, A.; Denizli, A.; Say, R. *Talanta* **2012**, *93*, 364.

(255) Bompart, M.; De Wilde, Y.; Haupt, K. *Advanced Materials* **2010**, *22*, 2343.

(256) Kantarovich, K.; Tsarfati, I.; Gheber, L. A.; Haupt, K.; Bar, I. *Analytical Chemistry* **2009**, *81*, 5686.

(257) Kantarovich, K.; Tsarfati, I.; Gheber, L. A.; Haupt, K.; Bar, I. *Biosensors & Bioelectronics* **2010**, *26*, 809.

(258) Kantarovich, K.; Tsarfati-BarAd, I.; Gheber, L. A.; Haupt, K.; Bar, I. *Plasmonics* **2013**, *8*, 3.

(259) Kostrewa, S.; Emgenbroich, M.; Klockow, D.; Wulff, G. *Macromolecular Chemistry and Physics* **2003**, *204*, 481.

(260) Kan, X.; Liu, T.; Li, C.; Zhou, H.; Xing, Z.; Zhu, A. *Journal of Solid State Electrochemistry* **2012**, *16*, 3207.

(261) Wang, H.; Zhao, H.; Quan, X.; Chen, S. *Electroanalysis* **2011**, *23*, 1863.

(262) Xue, J. Q.; Li, D. W.; Qu, L. L.; Long, Y. T. *Analytica Chimica Acta* **2013**, *777*, 57.

(263) Li, S.; Du, D.; Huang, J.; Tu, H.; Yang, Y.; Zhang, A. *Analyst* **2013**, *138*, 2761.

(264) Holthoff, E. L.; Stratis-Cullum, D. N.; Hankus, M. E. *Sensors* **2011**, *11*, 2700.

(265) Haynes, C. L.; McFarland, A. D.; Van Duyne, R. P. *Analytical Chemistry* **2005**, *77*, 338A.

(266) Volkert, A. A.; Subramaniam, V.; Ivanov, M. R.; Goodman, A. M.; Haes, A. J. *ACS Nano* **2011**, *5*, 4570.

(267) Schatz, G. C.; Van Duyne, R. P. *Electromagnetic Mechanism of Surface-Enhanced Spectroscopy*; Wiley: New York, 2002; Vol. 1.

(268) Haes, A. J.; Haynes, C. L.; McFarland, A. D.; Schatz, G. C.; Van Duyne, R. P.; Zou, S. *MRS Bulletin* **2005**, *30*, 368.

(269) Pierre, M. C. S.; Haes, A. J. *Anal. Chem.* **2012**, *84*, 7906.

(270) Roca, M.; Haes, A. J. *Journal of the American Chemical Society* **2008**, *130*, 14273.

(271) Spizzirri, U. G.; Peppas, N. A. *Chemistry of Materials* **2005**, *17*, 6719.

(272) Rosengren-Homberg, J. P.; Karlsson, J. G.; Svenson, J.; Andersson, H.; Nicholls, I. A. *Organic & Biomolecular Chemistry* **2009**, *7*, 3148.

(273) Fahmy, R.; Marnane, B.; Bensley, D.; Hollenbeck, R. G. *AAPS PharmSci* **2002**, *4*, 137.

(274) Kreibig, U. In *Handbook of Optical Properties*; Hummel, R. E., Wissmann, P., Eds.; CRC Press: Boca Raton, 1997; Vol. II, p 145.

(275) Haynes, C. L.; Haes, A. J.; McFarland, A. D.; Van Duyne, R. P. *Topics in Fluorescence Spectroscopy* **2005**, *8*, 47.

(276) Orendorff, C. J.; Gearheart, L.; Jana, N. R.; Murphy, C. J. *Phys. Chem. Chem. Phys.* **2006**, *8*, 165.

(277) Ginde, A. A.; Liu, M. C.; Camargo, C. A. *Arch. Intern. Med.* **2009**, *169*, 626.

(278) Borisov, S. M.; Wolfbeis, O. S. *Chemical Reviews* **2008**, *108*, 423.

(279) Wang, Y.; Li, Y. S.; Zhang, Z.; An, D. *Spectrochimica Acta Part A* **2003**, *59*, 589.

(280) Pavel, I.; Szeghalmi, A.; Moigno, D.; Cinta, S.; Kiefer, W. *Biopolymers* **2002**, *72*, 25.

(281) Pérez-Juste, J.; Pastoriza-Santos, I.; Liz-Marzán, L. M.; Mulvaney, P. *Coordin. Chem. Rev.* **2005**, *249*, 1870.

(282) Amin, F.; Yushchenko, D. A.; Montenegro, J. M.; Parak, W. J. *ChemPhysChem* **2012**, *13*, 1030.

(283) Nikoobakht, B.; Wang, Z. L.; El-Sayed, M. A. *J. Phys. Chem. B* **2000**, *104*, 8635.

(284) Gole, A.; Murphy, C. J. *Langmuir* **2005**, *21*, 10756.

(285) Gole, A.; Murphy, C. J. *Chem. Mater.* **2005**, *17*, 1325.

(286) Gittins, D. I.; Caruso, F. *J. Phys. Chem. B* **2001**, *105*, 6846.

(287) Labrou, N. E. *Journal of Chromatography B* **2003**, *790*, 67.

(288) Sellergren, B. *Analytical Chemistry* **1994**, *66*, 1578.

(289) Jana, N. R.; Gearheart, L. A.; Obare, S. O.; Johnson, C. J.; Edler, K. J.; Mann, S.; Murphy, C. J. *J. Mater. Chem.* **2002**, *12*, 2909.

(290) Lee, S.; Anderson, L. J. E.; Payne, C. M.; Hafner, J. H. *Langmuir* **2011**, *27*, 14748.

(291) Dendramis, A. L.; Schwinn, E. W.; Sperline, R. P. *Surface Science* **1983**, *134*, 675.

(292) Bjarnason, B.; Chimuka, L.; Ranstrom, O. *Analytical Chemistry* **1999**, *71*, 2152.

(293) Pierre, M. C. S.; Haes, A. J. *Analytical Chemistry* **2012**, *84*, 7906.

(294) Kennedy, B. J.; Spaeth, S.; Dickey, M.; Carron, K. T. *Journal of Physical Chemistry B* **1999**, *103*, 3640.

(295) Takahashi, M.; Niwa, M.; Ito, M. *Journal of PHysical Chemistry B* **1987**, *91*, 11.

(296) Zou, S.; Williams, C. T.; Chen, E. K. Y.; Weaver, M. J. *Journal of the American Chemical Society* **1998**, *120*, 3811.

(297) Haes, A. J.; Zou, S.; Schatz, G. C.; Van Duyne, R. P. *Journal of Physical Chemistry B* **2004**, *108*, 6961.

(298) Fleger, Y.; Mastai, Y.; Rosenbluh, M.; Dressler, D. H. *Journal of Raman Spectroscopy* **2009**.

(299) Xu, C. Y.; Zhang, P. X.; Yan, L. *Journal of Raman Spectroscopy* **2001**, *32*, 862.

(300) Ginde, A. A.; Liu, M. C.; Camargo, C. A.; Jr *Arch. Intern. Med.* **2009**, *169*, 626.

(301) Luque de Castro, M. D.; M. Fernández-Romero, J.; Ortiz-Boyer, F.; Quesada, J. M. *J. Pharmaceut. Biomed.* **1999**, *20*, 1.

(302) Wootton, A. M. *Clinical Biochemistry Review* **2005**, *26*, 33.

(303) Carter, G. D.; Jones, J. C.; Berry, J. L. *The Journal of Steroid Biochemistry and Molecular Biology* **2007**, *103*, 480.

(304) Jaslow, R.; CBSNews.com: 2014; Vol. 2014.

(305) DeLuca, H. F.; Schnoes, H. K. *Annu. Rev. Biochem.* **1983**, *52*, 411.